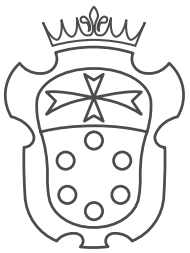

SCUOLA
NORMALE
SUPERIORE

Classe di Scienze

Corso di perfezionamento in
Fisica

XXXVII ciclo

Radiation fields in the Early Universe and their feedback effects

Settore Scientifico Disciplinare **FIS/05**

Candidato/a
dr. Daniele Manzoni

Relatore

Prof. Andrea Ferrara

Anno accademico 2024–2025

Contents

Abstract

Radiative feedback is a fundamental process shaping how galaxies form and evolve. The interaction between radiation fields and gas provides a natural self-regulation mechanism for star formation, while the collective light emitted by several sources on large scales builds the cosmic radiation backgrounds that preserve information about the epochs in which they were generated.

The advent of revolutionary facilities such as the James Webb Space Telescope (JWST) has made it possible to directly observe and study the assembly of the first galaxies. Its observations have revealed an unexpectedly high abundance of bright galaxies and massive black holes at early times, raising new questions about the physical processes that govern galaxy formation and black hole growth. These findings challenge our current models, suggesting that new theoretical directions must be explored to interpret what JWST is uncovering about the early Universe. The detection of numerous accreting black holes at $z \gtrsim 7$ has, in particular, renewed interest in their possible primordial origin, making the investigation of their observable consequences both timely and necessary.

On small scales, the extreme conditions within early galaxies offer an ideal environment for Lyα radiation pressure to dominate the regulation of star formation. What is the impact of Lyα feedback on early star formation? Can it limit the star formation efficiency (SFE)? Addressing these questions is crucial for testing theoretical models seeking to explain the overabundance of bright galaxies discovered by JWST. While the hypothesis of feedback-free star formation could account for such observations, it neglects the role of Lyα feedback. Is truly feedback-free star formation still possible once Lyα feedback is included in theoretical models?

From a larger-scale perspective, populations of accreting black holes could produce detectable radiation backgrounds. The accretion process itself would be influenced by the feedback from these backgrounds, which provide additional heating in the early Universe. Intriguingly, observations of the near-infrared background (NIRB) have revealed an excess in its large-scale fluctuations. Could a population of accreting primordial black holes reproduce the features observed in these NIRB fluctuations?

This thesis is organised into four Parts. Part I introduces the general context and motivations, followed by two main research components dedicated to Lyα feedback (Part II) and primordial black holes (Part III) in the early Universe. The detailed structure of the chapters is as follows:

1. In Chapter 1, we provide a brief overview of cosmic history, establishing the physical background required for the subsequent chapters.

2. In Chapter 2, we introduce the main concepts related to primordial black holes, laying the theoretical groundwork for our modelling framework.

3. In Chapter 3, we describe the main observational probes of the early Universe, from the transformative discoveries of JWST to the information encoded in cosmic radiation backgrounds. These observations provide the foundation and motivation for the thesis.

4. In Chapter 4, we introduce the physics of the Lyα line. Starting from the basic principles, we discuss Lyα radiative transfer and focus on the dynamical implications of resonant scattering.

5. In Chapter 5, we analyse how Lyα radiation pressure regulates star formation efficiency. We develop a shell model that includes Lyα feedback and validate it with dedicated hydrodynamical simulations, deriving the maximum SFE allowed under Lyα feedback.

6. In Chapter 6, we study early Lyα feedback by following the evolution of ionised bubbles around massive stars. By linking the star formation rate to the volume filling factor of Lyα-driven bubbles, we derive the resulting SFE and show that Lyα feedback removes the possibility of feedback-free star formation.

7. In Chapter 7, we develop a model to predict the radiation backgrounds produced by PBHs. This includes modifications to the matter power spectrum induced by PBHs, thermal feedback from X-ray emission due to accretion, and extended PBH mass functions. We then compute the NIRB signal produced by PBHs and compare it with observational data.

Finally, in Part IV, we summarise the main results and outline future developments and perspectives.

Part I

Introduction

Chapter 1

Overview of the Cosmic History

1.1 The Cosmological Model

The cosmological model used today to describe the Universe is built from only a few fundamental components. Despite its simplicity, it provides a powerful theoretical framework on which modern cosmological theories and predictions are based. The key ingredients are:

- A theory of gravitation: *General Relativity*
- The cosmological principle: *the Universe is homogeneous and isotropic on sufficiently large scales*
- A small set of physical parameters: *the cosmological parameters*

On cosmological scales, gravity is the only effective interaction. The other fundamental forces—electromagnetic, weak, and strong—play a role only on smaller astrophysical scales, from galaxies down to stellar interiors.

Einstein's theory of General Relativity describes how the geometry of spacetime is determined by the distribution of matter, and vice versa. In the words of J. A. Wheeler, *"Spacetime tells matter how to move; matter tells spacetime how to curve"*. Mathematically, spacetime is described by the metric tensor $g_{\mu\nu}$, which defines the spacetime interval ds between two events:

$$ds^2 = g_{\mu\nu} dx^\mu dx^\nu. \tag{1.1}$$

The four-vector dx^μ contains the temporal and spatial coordinates, expressed in spherical coordinates as (ct, r, θ, ϕ), where the time coordinate is rescaled by the speed of light c.

The interaction between matter and spacetime is governed by Einstein's field equations:

$$R_{\mu\nu} - \frac{1}{2} g_{\mu\nu} R = \frac{8\pi G}{c^4} T_{\mu\nu} + \Lambda g_{\mu\nu}, \tag{1.2}$$

where $R_{\mu\nu}$ is the Ricci tensor, R is the Ricci scalar (both depending non-trivially on $g_{\mu\nu}$), and together they describe the local curvature of spacetime. On the right-hand side, $T_{\mu\nu}$ is the energy–momentum tensor, while Λ is the cosmological constant. These terms encode the local content of matter and energy that curves spacetime. The cosmological constant, or dark energy, represents an energy density constant in space and time. Its gravitational effect is repulsive, and its physical nature remains unknown.

Einstein's equations are extremely difficult to solve for an arbitrary matter distribution. To obtain analytical solutions, the assumptions of homogeneity and isotropy were first introduced. Observations of the Cosmic Microwave Background (CMB, see Sec. 1.2.3) later confirmed that the Universe is indeed homogeneous and isotropic to within one part in 10^5 (Smoot et al., 1992). For such a Universe, the Einstein equations predict either expansion or contraction—no static solutions exist.

By adopting the cosmological principle, the spacetime geometry is constrained to the Friedmann–Robertson–Walker (FRW) metric:

$$ds^2 = c^2 dt^2 - a^2(t) \left[\frac{dr^2}{1 - kr^2} + r^2 (d\theta^2 + \sin^2\theta \, d\phi^2) \right], \tag{1.3}$$

where $a(t)$ is the scale factor, which describes the expansion (or contraction) of the Universe as a function of time, k is the spatial curvature, and $d\Omega^2 = d\theta^2 + \sin^2\theta \, d\phi^2$. Observations of the CMB show that our Universe is spatially flat, so $k \simeq 0$ (de Bernardis et al., 2000).

The expansion of the Universe was first observed in 1929 by the American astronomer Edwin Hubble. He found that the "nebulae" he was observing (now known to be galaxies outside the Milky Way) were receding with a velocity proportional to their distance (Hubble, 1929):

$$v = H_0 r. \tag{1.4}$$

Here, $H_0 = 67.11\,\mathrm{km\,s^{-1}\,Mpc^{-1}}$ is the Hubble constant. This relation follows naturally from the FRW metric. From Eq. 1.3, a source at a physical distance $r = a(t)R_c$, where R_c is the comoving coordinate, recedes with velocity $v = dr/dt = \dot{a}R_c = (\dot{a}/a)R_c = Hr$, where $H(t) = \dot{a}(t)/a(t)$ is the Hubble parameter, a generally time-dependent quantity.

The expansion of the Universe also has profound effects on light. Photons travel along null geodesics with $ds^2 = 0$, which gives $cdt = a(t)dr$. Let dr be the comoving distance between two successive wave crests; this distance remains constant as the photon propagates from t_0 to t_1. Hence, $dt_0/a(t_0) = dt_1/a(t_1)$. Since the photon frequency scales as $\nu \propto dt^{-1}$, it follows that

$$\nu_1 = \nu_0 \frac{a_0}{a_1} = \frac{\nu_0}{1+z}, \tag{1.5}$$

where the redshift is defined by $1 + z = a_1/a_0$. Equation 1.5 shows that if the scale factor of the Universe doubles, the frequency of light is reduced by a factor of three. Redshift is therefore the quantity most commonly used to describe the expansion of the Universe, rather than the scale factor itself.

From Eqs. 1.2 and 1.3, one can derive an equation for the evolution of the scale factor, known as the Friedmann equation:

$$\left(\frac{\dot{a}}{a}\right)^2 = H^2(t) = \frac{8\pi G}{3}\rho - \frac{kc^2}{a^2}. \tag{1.6}$$

This relation connects the expansion rate of the Universe, expressed by the Hubble parameter $H(t)$, to the total energy density ρ and the spatial curvature k.

The energy density can be decomposed into contributions from non-relativistic matter, radiation, and vacuum energy: $\rho = \rho_m + \rho_r + \rho_\Lambda$. Introducing the critical density,

$$\rho_c = \frac{3H^2}{8\pi G} \simeq 5 \times 10^{-30} \left(\frac{H}{H_0}\right)^2 \mathrm{g\,cm^{-3}}, \tag{1.7}$$

the Friedmann equation can be recast as

$$\frac{H(t)}{H_0} = \sqrt{\frac{\Omega_m}{a^3} + \frac{\Omega_r}{a^4} + \Omega_\Lambda}, \tag{1.8}$$

where the dimensionless density parameters are defined as $\Omega_m = \rho_m/\rho_c$, $\Omega_r = \rho_r/\rho_c$, and $\Omega_\Lambda = \rho_\Lambda/\rho_c$. Here, spatial curvature has been neglected. From Eq. 1.8 we see that the contributions of matter and radiation to the energy density decrease as $\sim a^{-3}$ and $\sim a^{-4}$, respectively. The steeper decline of radiation arises from the redshifting of photons, which leads to a loss of energy. In contrast, the dark energy term remains constant throughout cosmic evolution. The Friedmann equation thus describes the evolution of the scale factor in terms of a small set of cosmological parameters.

The most up-to-date values of the cosmological parameters, as reported by the *Planck* Collaboration (Planck Collaboration et al., 2020), are given in Table 1.1.

Ω_Λ	Ω_m	Ω_b	h	n_s	σ_8
0.6847	0.3153	0.0493	0.6736	0.9649	0.8111

Table 1.1: Cosmological parameters derived from the *Planck* Collaboration (Planck Collaboration et al., 2020). The first three are the density parameters for dark energy, total matter, and baryonic matter, respectively. h is the Hubble constant in units of $100\,\mathrm{km\,s^{-1}\,Mpc^{-1}}$, n_s is the spectral index of primordial perturbations, and σ_8 is the root-mean-square matter fluctuation on scales of $8\,\mathrm{Mpc}\,h^{-1}$.

1.2 From Big Bang to Recombination

1.2.1 The first second of the Universe

An expanding Universe implies that, when traced backward in time, it must have originated from an initial singularity. This moment is commonly referred to as the Big Bang. The density and temperature of the early Universe were extremely high. Since our understanding of particle physics is reliable only below energies of about $\sim 1\,\mathrm{GeV}$ (corresponding to $\sim 10^{13}\,\mathrm{K}$), the physics of the very early Universe remains uncertain. It is generally expected that all fundamental interactions—gravity, electromagnetic, weak, and strong—were unified at the earliest times in a Grand Unified Theory (GUT). Below the Planck time, $t \sim 10^{-43}\,\mathrm{s}$, a complete theory of quantum gravity, which is still lacking, would be required to make meaningful predictions. Despite this mystery, observations of the Universe's flatness, homogeneity, and isotropy strongly suggest the existence of a phase of exponential expansion, known as inflation (Linde, 1982). During inflation, quantum fluctuations were stretched to macroscopic scales, smoothing the Universe and driving it toward homogeneity. In this process, any initial curvature would have been diluted to negligible levels. Inflation is thought to have ended at $t \sim 10^{-32}\,\mathrm{s}$.

The Universe underwent a sequence of phase transitions driven by symmetry breaking in fundamental physics, progressively separating the different forces and giving rise to new particles. The breaking of the Grand Unified Theory (GUT) symmetry first split the strong interaction from the electroweak force. Subsequently, during the electroweak phase transition, the Higgs mechanism separated the electromagnetic and weak interactions, generating the W, Z, and Higgs bosons. As a result of these transitions, the four fundamental forces became distinct and decoupled from one another.

At that stage, the energy scale was so high that all particles were relativistic, and the expansion was dominated by radiation. Particle species remained in thermal equilibrium as long as their interaction rate Γ was much larger than the Hubble expansion rate H. When $\Gamma \sim H$, a species decoupled from the thermal bath and thereafter evolved with the background expansion. Interaction rates depend on the energy density, or equivalently the temperature[1].

As the Universe expanded, its temperature decreased as a consequence of entropy conservation. For a fluid with density ρ and pressure P, the entropy in a volume V is

$$S = \frac{\rho + P}{T} V. \tag{1.9}$$

For radiation, $P_r = \rho_r/3$ and the volume scales as $V \propto a^3$. Entropy conservation, $dS/dt = 0$, then implies that the temperature scales as $T \propto a^{-1}$.

When the Universe was about $t \sim 10^{-6}\,\mathrm{s}$ old, it had cooled to $T \sim 100\,\mathrm{MeV}$. At this temperature, protons and neutrons formed out of the quark–gluon plasma in the quark-hadron phase transition. Weak interactions maintained equilibrium between protons and neutrons through β-decay ($n \leftrightarrow p + e^- + \bar{\nu}_e$) and electron capture ($p + e^- \leftrightarrow n + \nu_e$). When the temperature dropped to $T \sim 1\,\mathrm{MeV}$, these interactions decoupled, leaving the neutron-to-proton ratio frozen at about $n_n/n_p \sim 0.2$. At this point, the Universe was approximately one second old.

1.2.2 The formation of the first elements

A key milestone in the early Universe was the formation of the first heavy elements from protons and neutrons, a process known as Big Bang Nucleosynthesis (BBN). The first necessary step in nucleosynthesis was the formation of deuteron, the bound state of a proton and a neutron:

$$n + p \leftrightarrow d + \gamma. \tag{1.10}$$

Since photons can dissociate deuteron only when their energy exceeds the binding energy ($\sim 2\,\mathrm{MeV}$), one might expect deuteron to form already within the first second. In practice, efficient deuteron production was delayed until about three minutes after the Big Bang. The reason is that photons, being in thermal equilibrium with other particles, follow a blackbody distribution. The high-energy tail of this distribution always contains some photons energetic enough to dissociate deuterons. As photons outnumber baryons by a factor of $\sim 10^9$, even these rare photons were sufficient to prevent stable deuteron survival. Only when the temperature dropped to $T \sim 0.1\,\mathrm{MeV}$ could deuteron accumulate efficiently. This delay is known as the deuteron bottleneck (Cyburt et al., 2016).

At that point, BBN proceeded rapidly, producing helium isotopes ($^3\mathrm{He}$ and $^4\mathrm{He}$), followed by lithium ($^7\mathrm{Li}$). Nucleosynthesis then halted, since there are no stable nuclei with mass numbers 5 or 8. This nuclear "gap" prevents the efficient production of heavier elements.

For example, the synthesis of carbon requires the intermediate formation of $^8\mathrm{Be}$ through:

$$^4\mathrm{He} + {}^4\mathrm{He} \rightarrow {}^8\mathrm{Be} + \gamma, \tag{1.11}$$

$$^8\mathrm{Be} + {}^4\mathrm{He} \rightarrow {}^{12}\mathrm{C} + \gamma, \tag{1.12}$$

[1] The energy is given by $E \sim k_B T$. For simplicity, the Boltzmann constant k_B is omitted in the following.

a sequence known as the triple-alpha process. However, because $^8\mathrm{Be}$ is unstable and particle densities during BBN were relatively low, no significant carbon production occurred. The production of carbon and heavier elements had to await the formation of stars, hundreds of Myrs after the Big Bang.

Element abundances became fixed once nuclear reactions froze out, between ~ 6 minutes (for H and $^4\mathrm{He}$) and ~ 8 hours (for $^7\mathrm{Li}$). The final primordial abundances relative to hydrogen were about $\mathrm{He/H} \sim 0.08$ and $\mathrm{Li/H} \sim 10^{-10}$ (Cooke, 2024).

1.2.3 The matter-radiation decoupling

After BBN, the Universe consisted of a hot plasma of electrons, protons, and photons, kept in thermal equilibrium through $p+e \leftrightarrow H+\gamma$. The expansion was dominated by radiation, but it became matter dominated about 47,000 years after the Big Bang, corresponding to $z \sim 3300$.

The next crucial stage in the thermal history of the Universe was recombination, when electrons and protons combined to form neutral hydrogen. In thermal equilibrium, the ionization fraction x evolves with temperature according to the Saha equation:

$$\frac{x^2}{1-x} = \frac{(2\pi m_e kT)^{3/2}}{n(2\pi\hbar)^3} \exp(-B/kT), \tag{1.13}$$

where n is the total number density and $B = 13.6\,\mathrm{eV}$ is the hydrogen binding energy. The equilibrium prediction gives $x = 0.5$ at $T_{\mathrm{dec}} \simeq 3700\,\mathrm{K}$, corresponding to $z_{\mathrm{dec}} \simeq 1360$.

In reality, recombination proceeded far from equilibrium. When an electron is captured directly into the ground state, it produces a photon energetic enough to ionize another atom, leading to no net recombination. The only efficient pathway was through capture into the $n = 2$ excited state, followed by a slow two-photon decay to the ground state. As a result, recombination was delayed until $T_{\mathrm{dec}} \sim 3300\,\mathrm{K}$, corresponding to $z_{\mathrm{dec}} \sim 1100$.

This marks the epoch of matter–radiation decoupling. Once the plasma became mostly neutral, photons no longer scattered efficiently and began to travel freely through space. These photons are observed today as the Cosmic Microwave Background (CMB), the oldest light we can detect.

Not all electrons recombined, however. As the neutral fraction increased, the recombination rate fell below the expansion rate, leaving a small residual free-electron population. This residual ionization allowed Thomson scattering to continue coupling the CMB temperature to the matter temperature until $z \sim 200$, after which the two fully decoupled.

The CMB is observed today as an almost perfect blackbody spectrum with temperature $T = 2.72548\,\mathrm{K}$ (Planck Collaboration et al., 2020). Tiny fluctuations at the level of 10^{-5} across the sky trace the density variations present at the time of last scattering. Figure 1.1 shows the amplitude of these temperature fluctuations as a function of angular scale. The peaks reflect acoustic oscillations in the photon–baryon plasma, whose positions and amplitudes encode precise information about the matter and radiation content of the Universe. The cosmological parameters derived from these fluctuations (Table 1.1) form the foundation of the current standard cosmological model.

1.3 The Dark Ages

After matter–radiation decoupling, fluctuations evolved under the influence of gravity. No luminous sources were yet present during this period, which is therefore referred to as the *Dark Ages*. The only observable signal from this epoch arises from the 21 cm photons produced by spin-flip transitions in neutral hydrogen. We now describe how fluctuations evolve first in the linear regime and later collapse to form dark matter halos.

1.3.1 The Linear Growth of Fluctuations

The evolution of matter under gravity is governed by the continuity, Euler, and Poisson equations:

$$\frac{\partial \rho}{\partial t} + \nabla_p \cdot (\rho \mathbf{v}) = 0, \tag{1.14}$$

$$\frac{\partial \mathbf{v}}{\partial t} + (\mathbf{v} \cdot \nabla_p)\mathbf{v} = -\nabla_p \phi, \tag{1.15}$$

$$\nabla_p^2 \phi = 4\pi G \rho, \tag{1.16}$$

where pressure has been neglected. This approximation is justified since we are interested in scales much larger than the Jeans length, and in particular in the evolution of dark matter.

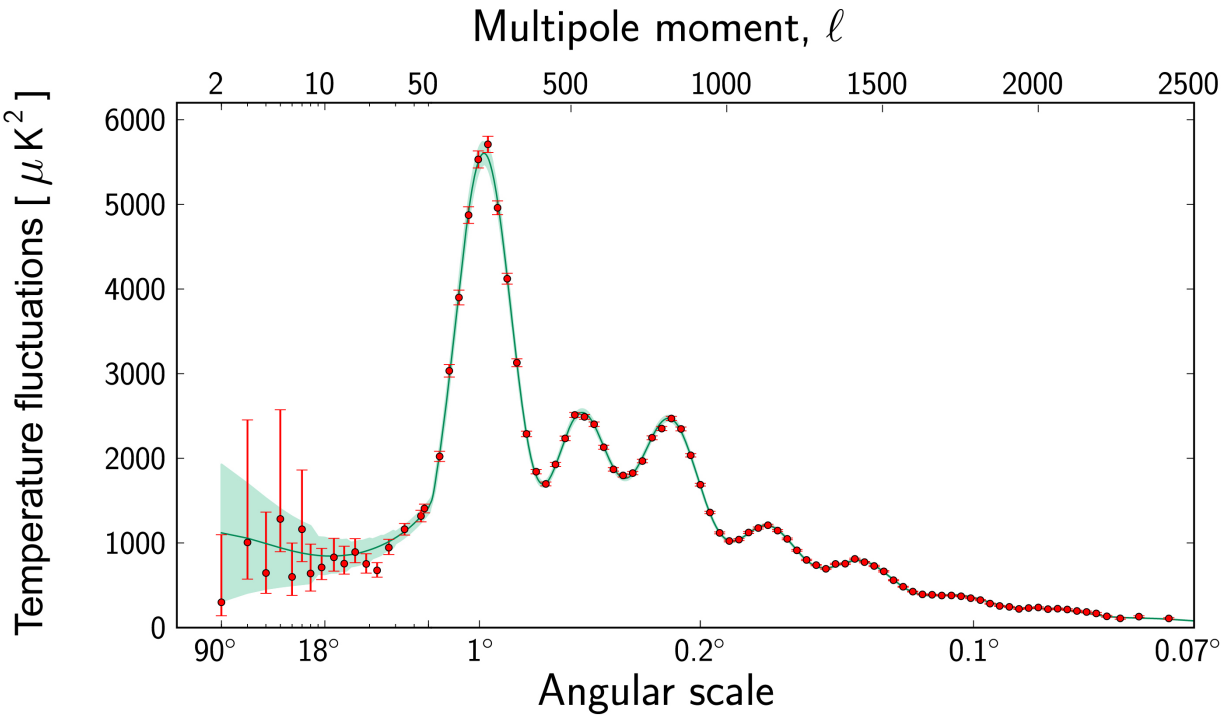

Figure 1.1: CMB angular power spectrum as a function of the angular scale or multiple moment l. Red point show Planck data, while the green solid line shows the best-fit curve. Image credit: ESA and the Planck collaboration

Because density fluctuations are small, it is useful to define the overdensity δ with respect to the mean background density:

$$\rho = \bar{\rho}(1+\delta), \quad \delta \ll 1. \tag{1.17}$$

Expanding to first order in δ and introducing the peculiar velocity $\mathbf{u}$, related to the proper velocity by $\mathbf{v} = \dot{a}\mathbf{R} + \mathbf{u}$, we obtain:

$$\dot{\delta} + a^{-1}\nabla \cdot \mathbf{u} = 0, \tag{1.18}$$

$$\dot{\mathbf{u}} + H\mathbf{u} + a^{-1}\nabla\phi = 0, \tag{1.19}$$

$$\nabla^2\phi = 4\pi G\bar{\rho}_0 a^{-1}\delta, \tag{1.20}$$

where $\nabla = a\nabla_p$ denotes the gradient with respect to comoving coordinates.

From these equations, the evolution of the overdensity follows:

$$\ddot{\delta} + 2H\dot{\delta} - 4\pi G\bar{\rho}_0 a^{-3}\delta = 0. \tag{1.21}$$

In a matter-dominated Universe, this equation has the solution

$$\delta(t) = \frac{3}{5}t^{2/3} + \frac{1}{2}t^{-1}, \tag{1.22}$$

corresponding to a growing and a decaying mode. The growing mode dominates, giving

$$\delta(t) \propto t^{2/3} \propto a \propto (1+z). \tag{1.23}$$

Thus, perturbations grow proportionally to the scale factor until they become non-linear.

1.3.2 The Non-linear Regime

To describe the non-linear evolution of overdensities, a simple but powerful approach is the spherical collapse model. The radius of a spherical shell enclosing a fixed mass M evolves according to

$$\frac{\mathrm{d}r}{\mathrm{d}t} = -\frac{GM}{r^2}. \tag{1.24}$$

The parametric solution is:

$$r = \frac{r_i}{2\delta_i}(1-\cos\theta), \tag{1.25}$$

$$t = \frac{\delta_i^{-3/2}}{2H_i}(\theta-\sin\theta), \tag{1.26}$$

where r_i, δ_i, and H_i denote the initial conditions. Collapse occurs at $\theta = 2\pi$, yielding the collapse redshift

$$(1+z_{\rm coll}) = \delta_i(1+z_i)\Big(\frac{4}{3}\Big)^{2/3}(2\pi)^{-2/3} = 0.356\,\delta_i(1+z_i). \tag{1.27}$$

Using the linear solution in Eq. (1.22), the extrapolated overdensity at $z=0$ is

$$\delta_0 \equiv \frac{3}{5}\delta_i(1+z_i), \tag{1.28}$$

so Eq. (1.27) can be rewritten as

$$(1+z_{\rm coll}) = \frac{\delta_0}{1.686}. \tag{1.29}$$

This shows that collapse occurs when the linearly extrapolated overdensity reaches the critical value $\delta_c = 1.686$.

After collapse, shell crossing invalidates the spherical model. The system virialises and relaxes to equilibrium. The final mean density of the virialised halo is $\rho_{\rm vir} = 180\rho(z_{\rm coll})$. Dark matter halos represent the potential wells into which baryons subsequently accrete.

The properties of a halo of mass M_h collapsing at redshift z are given by Barkana & Loeb (2001):

$$R_{\rm vir} = 0.784\Big(\frac{M_h}{10^8\,h^{-1}M_\odot}\Big)^{1/3}\Big(\frac{\Omega_m\Delta_c}{\Omega_m^z 18\pi^2}\Big)^{1/6}\Big(\frac{1+z}{10}\Big)^{-1}\,h^{-1}\,{\rm kpc}, \tag{1.30}$$

$$V_c = 23.4\Big(\frac{M_h}{10^8\,h^{-1}M_\odot}\Big)^{1/3}\Big(\frac{\Omega_m\Delta_c}{\Omega_m^z 18\pi^2}\Big)^{1/2}\Big(\frac{1+z}{10}\Big)^{1/2}\,{\rm km\,s^{-1}}, \tag{1.31}$$

$$T_{\rm vir} = 1.98\times10^4\Big(\frac{\mu}{0.6}\Big)\Big(\frac{M_h}{10^8\,h^{-1}M_\odot}\Big)^{2/3}\Big(\frac{\Omega_m\Delta_c}{\Omega_m^z 18\pi^2}\Big)^{1/3}\Big(\frac{1+z}{10}\Big)\,{\rm K}, \tag{1.32}$$

with (Bryan & Norman, 1998)

$$\Delta_c = 18\pi^2 + 82(\Omega_m^z-1) - 39(\Omega_m^z-1)^2, \tag{1.33}$$

$$\Omega_m^z = \frac{\Omega_m(1+z)^3}{\Omega_m(1+z)^3+\Omega_\Lambda}, \tag{1.34}$$

where μ is the mean molecular weight.

Once halos form, smaller ones merge hierarchically into larger structures. The abundance of halos of mass M, the *Halo Mass Function* (HMF), can be described using the Press–Schechter formalism. In this approach, regions of a Gaussian random density field that exceed a critical threshold $\delta_{\rm crit}$ are assumed to collapse. After smoothing the field on a scale R, the probability of finding a fluctuation of amplitude between δ_M and $\delta_M + d\delta_M$ is (Press & Schechter, 1974)

$$P(\delta_M, R, z)\,{\rm d}\delta_M = \frac{1}{\sqrt{2\pi}\sigma_M}\exp\Big(-\frac{\delta_M^2}{2\sigma_M^2}\Big){\rm d}\delta_M, \tag{1.35}$$

where σ_M is the variance of the density field on scale R, related to mass M through the filter function.

The fraction of matter collapsed into halos above mass M is

$$f_{\rm coll}(>M,z) = 2\int_{\delta_{\rm crit}}^{\infty}{\rm d}\delta_M\,P(\delta_M,R,z) = {\rm erfc}\Big(-\frac{\delta_{\rm crit}}{2\sigma_M^2}\Big), \tag{1.36}$$

where the prefactor of two corrects for underdense regions embedded within larger collapsing structures. Differentiating Eq. (7.2) yields the HMF:

$$\frac{{\rm d}n}{{\rm d}M} = \sqrt{\frac{2}{\pi}}\frac{\bar\rho}{M}\frac{\delta_c(z)}{\sigma_M^2}\left|\frac{{\rm d}\sigma_M}{{\rm d}M}\right|\exp\Big(-\frac{\delta_c^2(z)}{2\sigma_M^2}\Big), \tag{1.37}$$

with $\delta_c(z) = 1.686/D(z)$, where the growth factor is (Lightman & Schechter, 1990)

$$D(z) = \frac{g(z)}{g(0)(1+z)}, \tag{1.38}$$

$$g(z) = \frac{5}{2}\Omega_m \left[\Omega_m^{4/7} - \Omega_\Lambda + (1+\Omega_m/2)(1+\Omega_\Lambda/70)\right]^{-1}. \tag{1.39}$$

The HMF is a cornerstone of structure formation theory, providing the statistical link between the initial density field and the abundance of collapsed dark matter halos.

1.4 The Cosmic Dawn

We have so far discussed the evolution of dark matter. We now turn to the baryonic component and describe how the first stars and galaxies formed. On large scales, baryons trace the dark matter distribution; however, on smaller scales, gas pressure plays an important role.

We now reconsider the evolution of perturbations in Eq. 1.21, this time including the contribution from pressure:

$$\ddot{\delta} + 2H\dot{\delta} = 4\pi G\bar{\rho}_0 a^{-3}\delta + a^{-2}c_s^2\nabla^2\delta. \tag{1.40}$$

A static solution, in which pressure exactly balances gravity, satisfies

$$0 = 4\pi G\bar{\rho}_0 a^{-3}\delta + a^{-2}c_s^2\nabla^2\delta. \tag{1.41}$$

Further insight is obtained by taking the Fourier transform, yielding

$$0 = \left(4\pi G\bar{\rho}_0 a^{-3} - a^{-2}c_s^2\,|\mathbf{k}|^2\right)\delta_k, \tag{1.42}$$

where $\delta_k = \sum \delta \exp(-i\mathbf{k}\cdot\mathbf{R})$. The wavelength for which this condition is satisfied defines the Jeans length:

$$\lambda_J^p = \sqrt{\frac{\pi c_s^2}{G\bar{\rho}(z)}}. \tag{1.43}$$

For $\lambda > \lambda_J^p$, gravity dominates and perturbations can collapse, while on smaller scales ($\lambda < \lambda_J^p$), pressure prevents collapse. This criterion determines which perturbations are able to grow.

Once baryons fall into the gravitational potential wells of dark matter haloes, they are heated to the virial temperature. For further collapse to occur, the gas must lose energy through radiative cooling. Efficient collapse requires that the cooling timescale be shorter than the free-fall time. The cooling timescale is given by Rees & Ostriker (1977):

$$t_{\rm cool} = \frac{1}{\gamma - 1}\frac{nk_{\rm B}T}{\Lambda(n,T)}, \tag{1.44}$$

where $\Lambda(n,T)$ is the gas cooling function. For primordial gas, only hydrogen and helium are able to radiate away energy. The primordial cooling function is shown in Fig. 1.2.

At high temperatures, collisions can excite the electronic states of hydrogen atoms, which then de-excite by emitting Lyman-series photons. This process allows the gas to cool down to temperatures of $T \sim 10^4$ K. To reach lower temperatures, molecular hydrogen ($\rm H_2$) is required. Through radiative decay of its rotational transitions, $\rm H_2$ cooling can reduce the gas temperature further to $T \sim 200$ K. However, $\rm H_2$ cooling remains efficient only up to densities of $n \sim 10^4\ \rm cm^{-3}$. At higher densities, collisional excitation and de-excitation processes (which scale as $\propto n^2$) dominate over radiative cooling (which scales as $\propto n$). Consequently, molecular hydrogen cooling becomes inefficient, and further collapse can proceed only when the Jeans mass is reached (Dayal & Ferrara, 2018):

$$M_J = 500\left(\frac{T}{200\ \rm K}\right)^{3/2}\left(\frac{n}{10^4\ \rm cm^{-3}}\right)^{1/2}. \tag{1.45}$$

Therefore, we expect the first generation of stars in the Universe to be very massive. The precise mass distribution of Population III (Pop III) stars remains a topic of active debate (Klessen & Glover, 2023). This question is crucial for determining their ultimate fate—whether they collapse into black holes or explode as supernovae, and, in that case, what type of supernovae they produce. Most

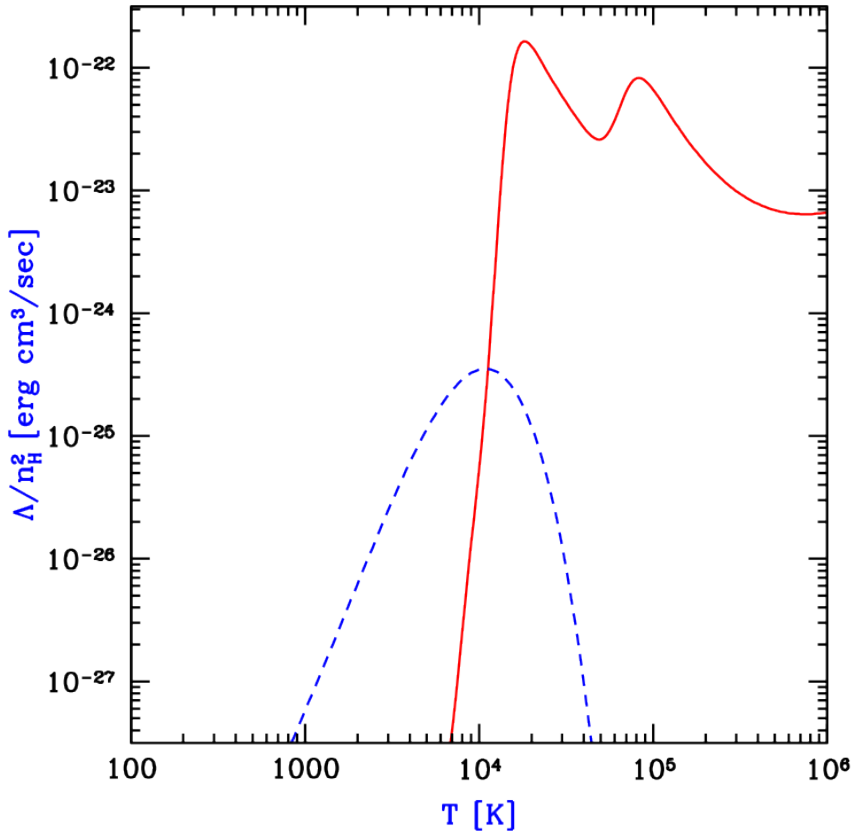

Figure 1.2: Cooling function of primordial gas as a function of temperature. The red solid line refers to atomic gas (hydrogen and helium), while the blue dashed line refers to molecular hydrogen. From Barkana & Loeb (2001).

of our current understanding of Pop III stars comes from theoretical models and numerical simulations rather than direct observations. Detecting these first stars, even indirectly, remains one of the greatest challenges in modern astrophysics.

The formation of Pop III stars marks the emergence of the first luminous sources in the Universe, a period commonly referred to as the *Cosmic Dawn*. Theoretical models place the onset of this era at redshifts $z \sim 20$–30, corresponding to about 100–200 Myr after the Big Bang. Modern observational facilities are now probing epochs as early as ~ 300 Myr after the Big Bang, approaching the time when the first stars are expected to have formed. However, detecting Pop III stars directly remains extremely difficult.

These stars produce heavy elements in their cores, and their surroundings become enriched with metals through stellar winds and supernova explosions. It is possible to estimate the minimum mass of gas into which metals from a supernova remnant (SNR) are mixed (Magg et al., 2020):

$$M_{\rm dil} = 1.9 \times 10^4 \left(\frac{E}{10^{51}\ {\rm erg}}\right)^{0.96} \left(\frac{n}{1\ {\rm cm}^{-3}}\right)^{-0.11} M_\odot, \tag{1.46}$$

where E is the explosion energy. A single SNR can therefore enrich its surroundings up to a metallicity of approximately $Z_{\rm max} \sim 3 \times 10^{-3}\ Z_\odot$.

This enrichment has profound consequences: subsequent generations of stars can no longer form from pristine gas. Once a critical metallicity of $Z_{\rm crit} \sim 10^{-5}\ Z_\odot$ is reached (Schneider et al., 2002), the gas cooling and fragmentation properties change significantly. This marks the transition from the primordial Pop III to the more familiar Pop II stellar populations observed in high-redshift galaxies.

1.5 The Epoch of Reionization

The emergence of the first luminous sources marked the onset of the last major phase transition of the intergalactic medium (IGM): the Epoch of Reionization (EoR). During this period, the hydrogen in the Universe transformed from being almost entirely neutral to becoming highly ionized. Ultraviolet (UV) photons with energies above $13.6\,{\rm eV}$, emitted by the first generations of stars and galaxies, ionized the surrounding hydrogen and generated expanding H II regions embedded in an otherwise neutral medium (Dayal & Ferrara, 2018).

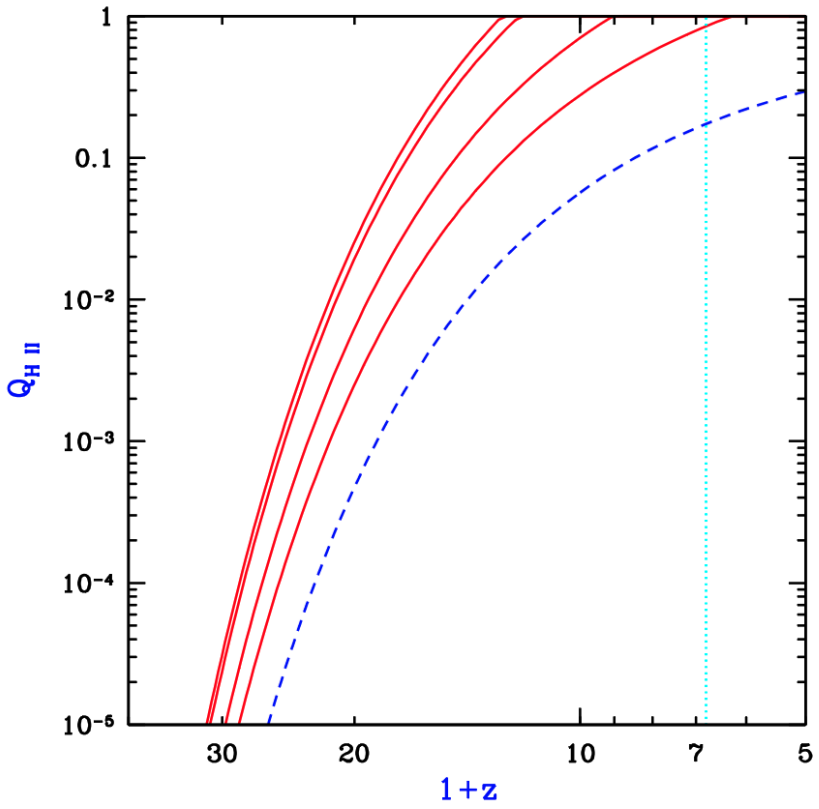

Figure 1.3: Redshift evolution of the ionized volume filling factor from semi-analytical models for clumping factors $C = 0, 1, 10, 30$ (solid red lines from left to right). The dashed curve shows the collapsed fraction $f_{\rm coll}$. The vertical dotted line indicates the observational lower limit for the end of reionization. From Barkana & Loeb (2001).

The ionization state of the IGM reflects the balance between photoionization and recombination processes. The global evolution of the ionized hydrogen filling factor, $Q_{\rm HII}$, can be described by (Madau et al., 1999)

$$\frac{dQ_{\rm HII}}{dt} = \frac{\dot{n}_{\rm ion}}{\langle n_{\rm H}\rangle} - \frac{Q_{\rm HII}}{t_{\rm rec}}, \tag{1.47}$$

where $\dot{n}_{\rm ion}$ is the comoving ionizing photon production rate, $\langle n_{\rm H}\rangle$ is the mean hydrogen number density, and $t_{\rm rec}$ is the recombination timescale. The resulting evolution of $Q_{\rm HII}$ from a semi-analytical model is illustrated in Fig. 1.3.

The reionization process involves a complex interplay of astrophysical mechanisms. Several parameters influence the evolution of Eq. 1.47, particularly the production and escape of ionizing photons from early galaxies. Massive stars within galaxies emit the majority of ionizing photons, but only a fraction of this radiation escapes into the IGM. This fraction, denoted by $f_{\rm esc}$, depends sensitively on the structure, morphology, and gas distribution within galaxies. Stellar feedback, such as supernova explosions, can carve low-density channels through which photons escape more efficiently. However, direct measurements of the Lyman continuum flux are challenging, especially at high redshift, and the dependence of $f_{\rm esc}$ on galaxy mass or redshift remains uncertain (Jaskot, 2025).

The escape fraction controls how efficiently galaxies contribute to the build-up of the cosmic UV background (UVB), a radiation field that profoundly influences both reionization and galaxy formation. Photoionization heating from the UVB raises the gas temperature to $T \sim 10^4$ K. This heating particularly affects halos with comparable virial temperatures, since gas can be photo-evaporated if its thermal energy exceeds the gravitational binding energy. Additionally, the increase in temperature enhances pressure support and raises the Jeans mass, thereby inhibiting gas collapse and reducing star formation—an example of negative feedback.

However, the UVB also exerts a positive feedback. Heating smooths out small-scale density fluctuations in the IGM, effectively lowering the clumping factor. Following Haardt & Madau (2012), the clumping factor evolves with redshift as $C(z) = 1 + 43z^{-1.71}$. A smoother IGM facilitates reionization, as ionizing photons encounter fewer dense, neutral regions acting as sinks.

The primary sources of the UVB—and therefore the main drivers of reionization—are believed to be galaxies hosted in low-mass dark matter halos. This conclusion arises naturally from the evolving halo mass function, assuming a roughly constant star formation efficiency with halo mass. Nonetheless, other sources may contribute. Accreting supermassive black holes in active galactic nuclei (AGN) produce hard UV spectra capable of ionizing hydrogen. Although their relatively low number density implies that AGN are

unlikely to dominate reionization, recent *JWST* detections of faint AGN suggest they may have provided a non-negligible contribution (Jiang et al., 2025; Grazian et al., 2024).

Current observations place the EoR within the redshift range $6 \lesssim z \lesssim 10$. The quantity most commonly constrained is the mean neutral hydrogen fraction, $x_{\rm HI} = 1 - Q_{\rm HII}$.

One of the most direct probes of reionization comes from the optical depth to Thomson scattering. Free electrons produced during reionization scatter cosmic microwave background (CMB) photons, leading to a damping of the CMB temperature anisotropies. Using high-precision CMB data, the Planck collaboration inferred an optical depth of $\tau_e = 0.054 \pm 0.007$ (Planck Collaboration et al., 2020). This optical depth depends on the integral of the ionized fraction over redshift:

$$\tau_e(z) = c\langle n_H \rangle \sigma_T \int_0^z {\rm d}z'\, Q_{\rm HI}(z') H^{-1}(z')(1+z')^2, \tag{1.48}$$

where $\sigma_T = 6.65 \times 10^{-25}\ {\rm cm}^2$ is the Thomson cross section. Measurements of τ_e therefore provide integrated constraints on the redshift evolution of $Q_{\rm HI}$.

The Lyα transition is one of the most powerful diagnostics of reionization, as it is both bright and extremely sensitive to neutral hydrogen. Lyα photons are produced when electrons decay from the $2p$ to the $1s$ state of hydrogen, corresponding to $\lambda_\alpha = 1216$ Å ($\nu_\alpha = 2.47 \times 10^{15}$ Hz). Because of its large cross section,

$$\sigma_\alpha = 5.88 \times 10^{-13} \left(\frac{T}{100\ {\rm K}}\right)^{-1/2} {\rm cm}^2, \tag{1.49}$$

Lyα scattering is highly resonant and thus very sensitive to even trace amounts of neutral gas. For a source with intrinsic flux F_0 and observed flux $F_{\rm obs}$, the two are related by

$$F_{\rm obs}(\lambda_{\rm obs}) = F_0 \left(\frac{\lambda_{\rm obs}}{1+z}\right) \exp[-\tau(\lambda_{\rm obs})], \tag{1.50}$$

where the total optical depth through the IGM is

$$\tau_\alpha(\lambda_{\rm obs}) = \int_0^{z_s} {\rm d}z\, n_H x_{\rm HI} H^{-1} (1+z)^2 \sigma_\alpha \left(\frac{\lambda_{\rm obs}}{1+z}\right). \tag{1.51}$$

If the intrinsic spectrum of a source can be reconstructed, comparison with observations provides an estimate of the neutral fraction along the line of sight. This technique is particularly effective for bright quasars, which serve as beacons illuminating the IGM.

As reionization nears completion, residual neutral patches in the IGM produce the characteristic Lyα forest—a series of absorption features in quasar spectra. In denser regions, absorption becomes saturated, creating zero-flux segments known as dark pixels, whose fraction can be used to infer $x_{\rm HI}$ (Gallerani et al., 2008; McGreer et al., 2015).

At higher redshifts, quasars can ionize large H II regions around them, generating observable Lyα transmission blueward of the line. On the red side, one might expect negligible absorption since photons are already out of resonance upon leaving the ionized region. However, if the surrounding IGM remains partially neutral, the damping wings of the Lyα profile become prominent, producing measurable absorption even redward of the line. These damping wings offer an additional probe of $x_{\rm HI}$ (Mortlock et al., 2011; Bañados et al., 2018).

Galaxies observed through their Lyα emission—known as Lyα emitters (LAEs)—provide complementary constraints on the reionization history. The shape and strength of their Lyα line profiles reveal the neutral gas distribution around galaxies (Mason et al., 2018). Moreover, the spatial clustering of LAEs reflects the patchy morphology of reionization: neutral regions suppress Lyα visibility and modulate the apparent clustering signal (Sobacchi & Mesinger, 2015).

A compilation of current observational constraints on the neutral hydrogen fraction as a function of redshift is presented in Fig. 1.4.

Perhaps the most transformative advance has come from the *James Webb Space Telescope* (JWST), which now enables efficient spectroscopic confirmation of galaxies deep within the EoR. With its unprecedented sensitivity, JWST can directly detect Lyα emission and thereby reveal the actual topology of reionization by mapping ionized bubbles around galaxies (Lu et al., 2025; Umeda et al., 2024; Nikolić, Ivan et al., 2025). These observations provide a crucial test for theoretical models of galaxy formation and reionization, linking the growth of early galaxies to the large-scale ionization structure of the Universe (Lu et al., 2023).

Remarkably, the JWST has detected Lyα emitters (LAEs) even at redshifts $z \gtrsim 10$ (Witstok et al., 2025; Bunker et al., 2023), a time when the IGM is expected to be predominantly neutral. The very presence of detectable Lyα emission at such early times challenges our current understanding of reionization. One possible explanation is that ionized bubbles already exist at these redshifts, allowing Lyα photons to escape—suggesting that reionization may have begun earlier than previously thought. Alternatively, the observed velocity offsets between the Lyα line and the systemic redshift indicate the presence of galactic outflows. This is particularly intriguing, as it would imply that we are directly witnessing the first episodes of stellar feedback operating in the earliest galaxies.

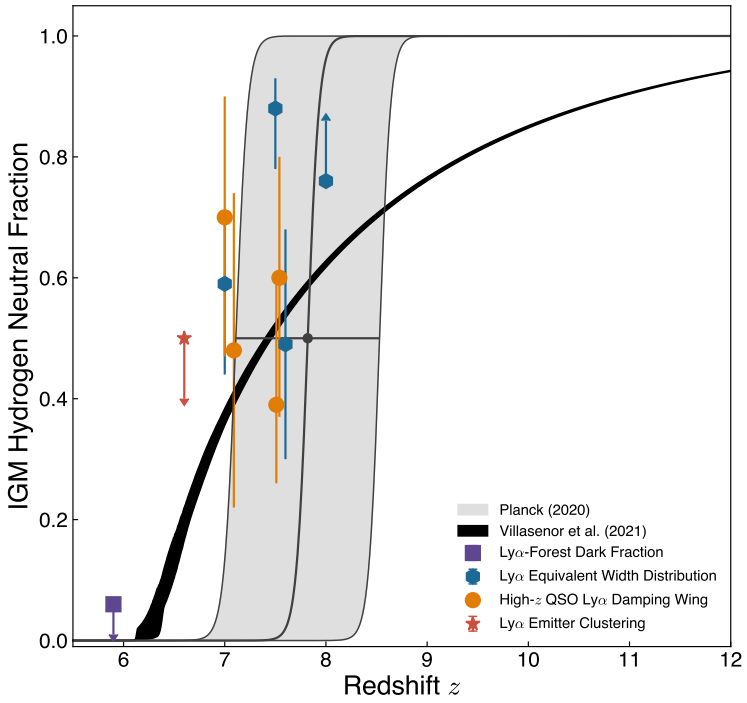

Figure 1.4: Constraints on the evolution of the hydrogen neutral fraction, $x_{\rm HI}$, in the intergalactic medium (IGM). From low to high redshift, measurements are derived from the fraction of dark pixels in the Lyα forest (purple), the clustering of Lyα emitters (red), the equivalent-width distribution of Lyα emitters (blue), quasar damping wings (orange), and the Thomson optical depth of the CMB (gray). The black solid line shows predictions from cosmological simulations of the EoR. From Robertson (2022).

1.6 Galaxies from within

So far, we have focused on the large-scale structure of the Universe. We now shift our attention to smaller scales to explore the internal structure of galaxies and the fundamental components that regulate their evolution.

On galactic scales, many key processes are regulated by the interstellar medium (ISM)—a complex and dynamic mixture of gas, dust, and radiation that occupies the space between stars. Although the ISM represents only a small fraction of a galaxy's total mass, it acts as the engine that fuels star formation and mediates the feedback mechanisms shaping galactic evolution. Composed primarily of hydrogen and helium, which together account for more than 98% of its mass, the ISM also contains heavier elements contributing the remaining $\sim 2\%$.

The interstellar gas spans an enormous range of densities (10^{-3}–10^{6} cm^{-3}) and temperatures (10–10^{7} K). Because of this diversity, it is customary to describe the ISM as a collection of coexisting phases, each characterised by distinct thermodynamic conditions and dominant physical processes. The main ISM phases are summarised below (Kohandel, 2022).

- *Molecular gas.* The densest and coldest phase of the ISM ($T \sim 10$–100 K, $n > 10^{2}$ cm^{-3}) forms giant molecular clouds (GMCs), in which hydrogen is predominantly in molecular form (H_2). These regions are the primary sites of star formation. Because H_2 lacks a permanent dipole moment, it is difficult to observe directly, so the molecular phase is typically traced using CO rotational transitions, high-density tracers such as HCN, and fine-structure lines like [C I]. Dust continuum emission in the far-infrared and submillimetre bands also serves as an indirect tracer of molecular gas.

- *Neutral medium.* The atomic hydrogen gas is organised into two main phases in approximate thermal pressure equilibrium. The cold neutral medium (CNM) has $T \sim 50$–100 K and $n \sim 20$–50 cm^{-3}, while the warm neutral medium (WNM) is characterised by $T \sim 6000$–10^{4} K and $n \sim 0.2$–0.5 cm^{-3}. Both are primarily composed of H I and are traced by the 21 cm hyperfine transition. The CNM forms dense H I clouds, whereas the WNM occupies the more diffuse intercloud medium and the outer regions of photodissociation fronts.

- *Ionised gas.* Ionised gas in the ISM appears in three principal forms. The H II regions consist of photoionised gas surrounding massive stars, with densities of $n \sim 10^{2}$–10^{3} cm^{-3} and temperatures of $T \sim 10^{4}$–10^{5} K. They are observed through hydrogen and helium recombination lines and various forbidden metal lines. The warm ionised medium (WIM) forms a more diffuse component ($n \sim 0.2$–0.5 cm^{-3}, $T \sim 8000$ K), traced primarily by Hα emission. Finally, the hot ionised medium (HIM)

represents the most tenuous phase ($n \sim 10^{-3}$–10^{-1} cm^{-3}, $T \sim 10^5$–10^6 K), produced by shock heating from supernovae and revealed by ultraviolet lines such as C IV, N V, and O VI.

- *Photodissociation regions.* The interfaces between ionised and molecular gas are known as photodissociation regions (PDRs), where far-ultraviolet (FUV) photons ($6 < h\nu < 13.6$ eV) from nearby massive stars dominate both the heating and chemical balance. Within PDRs, hydrogen transitions from atomic to molecular form, while carbon evolves from C^+ to C and finally CO. PDRs emit strongly in far-infrared and submillimetre lines, particularly [C II] 158 μm, [O I] 63 μm, and [C I] 370 μm—among the most important cooling lines of the ISM.

The typical physical conditions of these ISM phases are summarised in Table 1.2.

Table 1.2: Main physical properties of the different phases of the interstellar medium (ISM). The table lists typical gas temperature T, number density n, and ionisation state for each phase.

ISM Phase	Temperature T [K]	Density n [cm^{-3}]	n_e/n_H
Molecular Gas (H_2)	10–100	10^2–10^6	$< 10^{-6}$
Cold Neutral Medium (CNM)	50–100	20–50	$\sim 10^{-4}$
Warm Neutral Medium (WNM)	6×10^3–10^4	0.2–0.5	~ 0.1
Warm Ionised Medium (WIM)	$\sim 8 \times 10^3$	0.2–0.5	~ 0.7
H II Regions	10^4–10^5	10^2–10^3	1.0
Hot Ionised Medium (HIM)	10^5–10^7	10^{-3}–10^{-1}	1.0

Star formation is intimately linked to the physical conditions within GMCs, which represent the coldest and densest pockets of the ISM. Typical GMCs in the Milky Way have masses of 10^4–10^6 $M_\odot$ and radii of 10–100 pc (Solomon et al., 1987). Their internal structure is highly dynamic, shaped by a complex interplay of gravity, turbulence, shocks, magnetic fields, and radiative heating and cooling. The gas motions within GMCs are typically supersonic.

Despite this complexity, GMCs can often be described by a few global, averaged quantities such as mass M, radius R, and velocity dispersion σ. A convenient dimensionless parameter combining these quantities is the virial parameter (Bertoldi & McKee, 1992),

$$\alpha_{\rm vir} = \frac{5\sigma^2}{3GM}, \tag{1.52}$$

which quantifies the balance between kinetic energy $E_{\rm kin}$ and gravitational binding energy E_g. For a uniform-density, isolated cloud, this expression reduces to $\alpha_{\rm vir} = 2E_{\rm kin}/E_g$. In general, a GMC is considered self-gravitating if $\alpha_{\rm vir} \lesssim 2$, though this threshold may vary depending on magnetic support, internal structure, or external tidal forces.

The natural dynamical timescale for a self-gravitating system is the free-fall time,

$$t_{\rm ff} = \sqrt{\frac{3\pi}{32G\rho}}, \tag{1.53}$$

which represents the minimum time required for a cloud to collapse under its own gravity. The free-fall time therefore provides a useful lower limit to the collapse timescale of GMCs. If a gas mass M_g collapses over a time comparable to $t_{\rm ff}$, the corresponding star formation rate can be written as (Kennicutt & Evans, 2012)

$$\dot{M}_* = \epsilon_{\rm ff} \frac{M_g}{t_{\rm ff}}, \tag{1.54}$$

where $\epsilon_{\rm ff}$ denotes the star formation efficiency per free-fall time. If gravity were the only relevant force, we would expect $\epsilon_{\rm ff} \sim 1$, implying rapid collapse of the entire cloud. Observations and simulations, however, consistently show much lower values, $\epsilon_{\rm ff} \sim 0.01$, almost independent of scale—from dense clumps ($L \lesssim 1$ pc, $n \sim 10^4$–10^5 cm^{-3}) to diffuse regions ($L \sim 100$ pc, $n \sim 10$–100 cm^{-3}) (Kennicutt & Evans, 2012).

The remarkably low and nearly universal efficiency of star formation points to the critical role of feedback in regulating the collapse of molecular clouds. Various processes act in concert to oppose gravity, including turbulence, magnetic fields (Federrath, 2015; Girichidis et al., 2020), and stellar feedback. Among the latter, supernova explosions are particularly influential. A single supernova can inject $\sim 10^{51}$ erg of energy and substantial momentum into the surrounding ISM, driving powerful shocks that disrupt clouds and quench further star formation. Massive stars reach this stage after ~ 3 Myr, but earlier feedback mechanisms already begin to operate on shorter timescales. These early feedback channels—photoionisation, stellar winds, and radiation pressure—collectively act to expel gas and regulate star formation within GMCs.

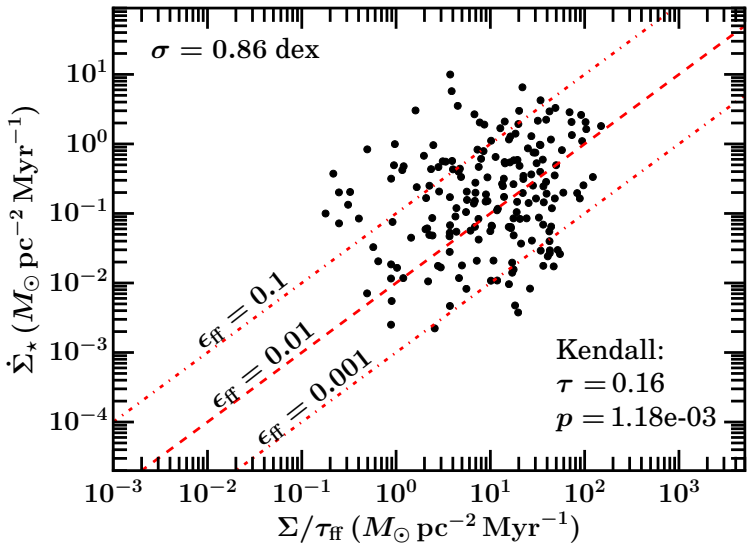

Figure 1.5: Star formation rate surface density as a function of the gas surface density divided by the free-fall time. Black points correspond to Milky Way GMCs. Red dashed lines show relations for constant $\epsilon_{\rm ff}$. The typical value is $\epsilon_{\rm ff} \sim 0.01$. From Lee et al. (2016).

- *Photoionisation.* Massive stars emit copious ionising radiation. In star-forming clouds, these photons heat the surrounding gas to $T \sim 10^4$ K, producing overpressurised regions that expand and drive ionisation fronts outward (Spitzer, 1978; Bisbas et al., 2015).
- *Stellar winds.* Stellar winds carry mass loss at typical velocities of $v_{\rm wind} \sim 3000$ km s^{-1} (Hopkins et al., 2023), generating shocks that heat the gas and inject momentum into the ISM.
- *Radiation pressure.* Each photon with energy E_ν carries momentum $p_\nu = E_\nu/c$. The cumulative effect of photon absorption and scattering exerts a net force on the gas and dust, which can become dynamically significant. Radiation pressure feedback has attracted substantial attention in both theoretical and observational studies (Smith et al., 2017; Grudić et al., 2018; Hopkins et al., 2020; Menon et al., 2023; Komarova et al., 2021; Olivier et al., 2021; Pathak et al., 2025).

Among the various forms of radiative feedback, Lyα radiation pressure stands out as particularly intriguing. Owing to the resonant nature of the Lyα transition, photons can undergo a vast number of scatterings, transferring large amounts of momentum to the gas (Adams, 1972, 1975; Bonilha et al., 1979). Despite this potential importance, the dynamical implications of Lyα feedback have been explored only in a handful of works (Smith et al., 2017; Kimm et al., 2018), owing to the complexity of modelling resonant scattering in a realistic medium. In the next chapter, we will show that it is now timely to investigate Lyα radiation pressure in detail, focusing on its feedback effects on star formation in the early Universe.

Chapter 2

Primordial Black Holes

So far, we have described the standard cosmological model, the ΛCDM paradigm, which represents the currently accepted framework for cosmology. Its solid foundation is provided by observations of the Cosmic Microwave Background (CMB), which allows us to trace the tiny primordial density fluctuations that eventually collapsed to form galaxies. However, these same fluctuations also open the possibility that some were sufficiently large to collapse directly under their own gravity, forming black holes. Black holes originating in this way are known as Primordial Black Holes (PBHs). The existence of PBHs would have far-reaching implications, enriching and potentially modifying the standard ΛCDM scenario into a more complex PBH–ΛCDM cosmology.

In this Chapter, we introduce the fundamental aspects of PBH physics, as a foundation for the modeling of cosmic backgrounds presented in Chap. 7. We first describe the formation mechanisms of PBHs in Sec. 2.1 and discuss their expected mass functions in Sec. 2.2. Finally, we provide an overview of their possible role as dark matter (DM) candidates in Sec. 2.3.

2.1 The formation of PBHs

Several physical processes could lead to the formation of PBHs, though each carries substantial theoretical uncertainty (see Carr et al. 2016 for a review). In this section, we discuss the simplest and most illustrative case—the collapse of primordial density fluctuations in the earliest moments of the Universe.

A self-gravitating system collapses only if its total energy, $E = \Omega + U$, is negative, where Ω and U are the gravitational potential and internal energies, respectively. During the radiation-dominated era, a spherical density fluctuation of radius R and density ρ has $\Omega \sim -G\rho^2 R^5$ and $U \sim \rho c^2 R^3$, the latter arising from relativistic pressure. Collapse therefore requires

$$\rho R^2 > \frac{c^2}{G}. \tag{2.1}$$

Equation (2.1) thus provides a lower limit on the density of a fluctuation at a given radius R for PBH formation.

Taking into account numerical factors, the minimum radius $R_{\min}$ (or Jeans radius R_J) of a fluctuation capable of collapse can be written as

$$R_{\min} = R_J = \sqrt{w}\, c\, \frac{5}{4\pi} \frac{1}{G\rho}, \tag{2.2}$$

where w is the equation-of-state parameter. For a radiation-dominated Universe, $w = 1/3$, although this value can vary during cosmological phase transitions such as the QCD or electroweak transitions, when particle creation or annihilation modifies the effective pressure. A fully relativistic treatment sets an upper limit to the perturbation size (Kopp et al., 2011):

$$R_{\max} = R_H = \frac{c}{H}, \tag{2.3}$$

where R_H is the Hubble radius. The radius of a perturbation that can collapse to a PBH must therefore satisfy

$$R_J \leq R \leq R_H. \tag{2.4}$$

To estimate the typical PBH mass, we can take $R \sim R_H \sim ct$, giving

$$M_{\rm PBH} = \rho R^3 \sim \frac{c^3 t}{G} \sim 10^{15} \Big(\frac{t}{10^{-23}\,\mathrm{s}} \Big)\,\mathrm{g}. \tag{2.5}$$

This simple relation shows that PBHs formed at different epochs can span an enormous mass range: from $M \sim 10^{-5}$ g for those forming at the Planck time (10^{-43} s), to $M \sim 10^5\ M_\odot$ for PBHs forming one second after the Big Bang. This wide spectrum

distinguishes PBHs from astrophysical black holes (ABHs), which have a minimum mass of about $2{-}3\ M_\odot$ (Bombaci, 1996) and can form only after the first stars (Pop III) appear at $z \sim 20{-}30$ (Bromm & Larson, 2004). PBHs, instead, would already exist at much earlier cosmic times.

In more realistic models, only a fraction γ of the horizon mass collapses into a PBH:

$$M_{\rm PBH} = \gamma M_H \approx 2.03 \times 10^5\, \gamma \left(\frac{t}{1\,\mathrm{s}}\right) M_\odot, \tag{2.6}$$

where γ depends on the collapse dynamics. Early analytical estimates suggested $\gamma \approx 0.2$ during the radiation era (Carr et al., 2021a), while later simulations found somewhat larger values, up to $\gamma \simeq 0.4$ (Green et al., 2004).

The primordial abundance of PBHs depends on the fraction of the Universe's mass that collapses into them at formation. This fraction, $\beta(M)$, can be estimated through the Press–Schechter formalism, analogous to the approach used in structure formation. It gives the probability that a region of mass $M_{\rm PBH}$ exceeds the critical overdensity threshold δ_c:

$$\beta(M_{\rm PBH}) = \int_{\delta_c}^{\infty} \frac{1}{\sqrt{2\pi}\sigma(M)} \exp\left\{\left[-\frac{\delta^2}{2\sigma(M)^2}\right]\right\} d\delta = \frac{1}{2}\,\mathrm{erfc}\left(\frac{\delta_c}{\sqrt{2}\sigma(M)}\right), \tag{2.7}$$

where $\sigma(M)$ is the variance of the density field smoothed on the mass scale M.

The present-day PBH density parameter can then be written as

$$\Omega_{\rm PBH}(M) = \beta(M)\,\Omega_r\,(1+z_{\rm coll}) = \gamma^{1/2}\left(\frac{\beta(M)}{1.15\times10^{-8}}\right)\left(\frac{M}{M_\odot}\right)^{-1/2}, \tag{2.8}$$

where the $(1+z_{\rm coll})$ factor arises because PBHs behave as matter ($\rho_{\rm PBH} \propto (1+z)^3$), while radiation energy density scales as $(1+z)^4$. This shows that even a minute mass fraction, $\beta \sim 10^{-8}$, of solar-mass PBHs could lead to a present-day density comparable to the critical value.

A key parameter in PBH formation is the critical overdensity δ_c required for collapse. Its precise value depends on both the early-Universe dynamics and the shape of the perturbations. Analytical estimates for a radiation-dominated Universe give $\delta_c \simeq 0.45$ (Carr & Hawking, 1974). Fully relativistic hydrodynamical simulations have refined this value: Niemeyer & Jedamzik (1999) confirmed the analytical prediction, while Shibata & Sasaki (1999) found a slightly lower value ($\delta_c = 0.42$). Later studies (Musco et al., 2005, 2009; Harada et al., 2013) brought the estimates back close to the original result, and more recent work found a range $\delta_c \simeq 0.4{-}0.5$, depending on the shape of the initial power spectrum of fluctuations (Germani & Musco, 2019).

2.2 The PBH mass function

PBHs can, in principle, span an enormous range of masses. Their statistical distribution is described by the PBH mass function, $\psi(M)$, defined as

$$\psi(M) = M\frac{dn}{dM} = \frac{dn}{d\ln M}, \tag{2.9}$$

which gives the number density of PBHs per logarithmic mass interval. Determining the mass function is essential for predicting both the overall abundance of PBHs and their potential observational signatures. The specific shape of $\psi(M)$ can amplify or suppress the impact of PBHs in different astrophysical or cosmological contexts.

The true form of the PBH mass function remains uncertain. It depends sensitively on the physical conditions prevailing in the radiation dominated era—particularly during and immediately after inflation—about which only limited information is available. Moreover, the fully relativistic treatment of gravitational collapse remains a complex problem. As a result, several functional forms have been proposed, each reflecting different assumptions about the initial conditions and PBH formation mechanisms.

The simplest possibility is a *monochromatic* mass function,

$$\psi(M) = \delta(M - M_0), \tag{2.10}$$

in which all PBHs share the same mass M_0. Although clearly idealised, this model is widely used as a benchmark, as it allows analytical simplicity and facilitates comparisons across different theoretical frameworks.

A more physically motivated case arises from a scale-invariant primordial power spectrum, $P(k) \propto k$, also known as the Harrison–Zel'dovich spectrum. In this scenario, density fluctuations have equal amplitude at horizon crossing, leading to a power-law mass function (Carr & Kühnel, 2020):

$$\psi(M) \propto M^{-\alpha+1}, \quad \alpha = \frac{2(1+2w)}{1+w}, \tag{2.11}$$

where w is the equation-of-state parameter of the cosmic fluid.

If instead the primordial spectrum follows a general power law, $P(k) \propto k^n$, the resulting mass function generalises to

$$\psi(M) \propto M^{-\alpha+1+\frac{n}{2}}, \tag{2.12}$$

showing how variations in the spectral index n modify the slope of the PBH distribution (Niemeyer & Jedamzik, 1999).

In scenarios where PBHs originate directly from inflationary fluctuations around smooth symmetric peaks, the expected distribution becomes approximately log-normal (Dolgov & Silk, 1993):

$$\psi(M) \propto \frac{1}{M} \exp\left[-\frac{(\ln M - \ln M_c)^2}{2\sigma^2}\right], \tag{2.13}$$

where M_c is the characteristic collapse mass and σ the width of the distribution.

These parametrised forms provide convenient tools to explore and compare different PBH formation scenarios. However, more complex, non-parametric mass functions have also been proposed. In particular, cosmological phase transitions can modify the equation of state of the early Universe, temporarily enhancing the probability of collapse. The decoupling of $W^{\pm}$ and Z^0 bosons, the quark–hadron transition, and e^+e^- annihilation each occur at distinct energy scales, producing multiple peaks in the mass spectrum that correspond roughly to the horizon mass at each transition epoch. Such models predict characteristic enhancements of $\psi(M)$ at masses of approximately 10^{-6}, 1, and $10^6\ M_\odot$ (Carr et al., 2021b; Franciolini et al., 2022).

2.3 The PBH-ΛCDM universe

Primordial black holes represent a captivating theoretical prospect in cosmology, offering a rich set of physical consequences. In what follows, we explore these effects within the broader context of a PBH–ΛCDM Universe.

The concept of black hole evaporation through quantum particle emission—now known as Hawking radiation—was first developed in the context of PBHs (HAWKING, 1974; Page & Hawking, 1976). Because PBHs can be extremely small, this effect becomes astrophysically relevant: those with masses below 10^{15} g would have already evaporated, while PBHs with $M \gtrsim 10^{15}$ g would still be radiating photons today. Detecting such emission would not only confirm the existence of PBHs but also provide direct evidence for Hawking radiation itself.

Another central idea, first proposed by Chapline (1975), is that PBHs could constitute at least part of the DM in the Universe. Since they would form before BBN, their abundance is not limited by the baryonic matter density inferred from BBN constraints, making them effectively non-baryonic. On cosmological scales, PBHs would contribute to the total matter density, ρ_m, behaving as cold dark matter because they are non-relativistic massive objects.

On galactic and sub-galactic scales (~ 100 kpc and below), PBHs could produce observable signatures that allow us to test their presence and constrain their abundance. In the 1990s, interest in PBHs was revived by the MACHO (Massive Compact Halo Object) project (Alcock et al., 1997), which aimed to detect compact dark matter candidates via gravitational microlensing. Monitoring 8.5 million stars in the Large Magellanic Cloud over two years, the collaboration detected eight microlensing events, compared with only ~ 1 expected from known stellar populations. These results implied objects of average mass $\sim 0.5\ M_\odot$, potentially contributing about half of the halo mass. Although this initially suggested that PBHs might represent a significant DM component, extended observations over 5.7 years reduced this estimate, limiting the fraction of the dark matter halo in MACHOs to below 20% (Alcock et al., 2000).

Further microlensing surveys by the EROS collaboration (1990–2003) yielded even stricter constraints. Observations of the Magellanic Clouds indicated that MACHOs contribute less than 8% of the Galactic halo mass, effectively excluding compact objects with $0.6 \times 10^{-7}\ M_\odot < M < 1\ M_\odot$ as the dominant form of dark matter (Tisserand, P. et al., 2007).

Interest in PBHs was reignited in 2016 following the LIGO–VIRGO detection of gravitational waves from merging black holes (Abbott et al., 2016). The inferred masses of these black holes, around $30\ M_\odot$, are naturally consistent with a primordial origin (Bird et al., 2016; Clesse & García-Bellido, 2017; Sasaki et al., 2016). Sasaki et al. (2016) estimated a PBH merger rate of $\sim 2\ \mathrm{Gpc}^{-3}\,\mathrm{yr}^{-1}$, comparable to the rate inferred from the GW150914 event (2–$53\ \mathrm{Gpc}^{-3}\,\mathrm{yr}^{-1}$). Later observations refined this range to 12–$213\ \mathrm{Gpc}^{-3}\,\mathrm{yr}^{-1}$ (Abbott et al., 2017b), compatible with PBHs of $\sim 30\ M_\odot$ if they constitute a fraction $0.0033 < f_{\rm PBH} < 0.022$ of the dark matter (Raidal et al., 2017). However, merger-rate predictions depend strongly on model assumptions, and current gravitational-wave detections alone cannot conclusively confirm a primordial origin. Certainly, the detection of gravitational waves from sub-solar-mass black holes would provide direct evidence for a primordial formation channel.

More recently, De Luca et al. (2020) pointed out that the spin distribution of black holes detected by LIGO–VIRGO offers an additional clue. Most observed systems exhibit very low spins (et al, 2019; Abbott, 2019), consistent with the expectation for PBHs that accrete gas slowly after formation. The dimensionless spin parameter of a black hole,

$$\chi = \frac{|\vec{J}|}{M^2}, \tag{2.14}$$

where $\vec{J}$ is the angular momentum and M the mass, is predicted to remain close to zero for PBHs with $M \lesssim 30\ M_\odot$, as gas accretion increases their mass more efficiently than their angular momentum. In contrast, a robust prediction for the spin distribution of astrophysical black holes is still lacking.

Despite the absence of definitive detections, the search for PBHs across different mass scales has led to increasingly stringent constraints on their abundance. At present, three mass windows remain where PBHs could constitute a non-negligible fraction of the dark matter: the asteroid mass range (10^{16}–10^{17} g), the sublunar mass range (10^{20}–10^{26} g), and the intermediate-mass range (10–$10^3\ M_\odot$).

The presence of PBHs would also alter the matter power spectrum. Although the total energy density of the regions where PBHs form remains constant, their formation introduces fluctuations in the relative number densities of the various components of the Universe. This occurs because, as soon as PBHs form, they behave as non-relativistic matter rather than radiation. These fluctuations are known as isocurvature perturbations, and they add extra power to the standard ΛCDM matter power spectrum (Meszaros, 1975):

$$P(k) = P_{\Lambda\mathrm{CDM}}(k) + P_{\mathrm{iso}}(k) \tag{2.15}$$

The additional power contributed by PBHs can dominate on small scales, depending on their abundance. Since the matter power spectrum determines the halo mass function, any modification to it would directly affect the formation and abundance of dark matter halos—and consequently, of galaxies (Liu & Bromm, 2022). These effects can become substantial if PBHs make up a significant fraction of the dark matter.

Because PBHs behave as dark matter, they would trace the large-scale structure of the Universe, following both diffuse intergalactic filaments and collapsed dark matter halos. Gas accretion onto PBHs would then generate background radiation across multiple wavelengths (Hasinger, 2020; Ziparo et al., 2022). The resulting emission could contribute to the observed cosmic backgrounds, offering a potential observational window into a population of accreting PBHs. The cosmic backgrounds that may hint at such a population are discussed in detail in Sec. 3.2.

As discussed in Chap. 1, radiation fields play a crucial role in regulating star formation, both on small scales—by influencing cloud dynamics—and on large scale, by setting the mass and timing of gas collapse into halos. Similarly, feedback from PBHs could significantly affect the formation of the first stars and the early evolution of galaxies (Liu & Bromm, 2023; Zhang et al., 2025). Importantly, these effects might remain non-negligible even if PBHs contribute only a small fraction of the total dark matter.

Finally, PBHs have been proposed as possible seeds for the formation of the supermassive black holes observed at high redshift (Ziparo et al., 2024). In this scenario, PBHs residing in the centers of dark matter halos begin to accrete gas once the halos reach the atomic cooling threshold. Dynamical friction within the dense gas causes PBHs to lose angular momentum, enabling them to undergo runaway mergers that result in the formation of massive black hole seeds. Remarkably, this process could occur even for very small PBH abundances, $f_{\mathrm{PBH}} \sim 3 \times 10^{-6}$. The model further predicts a specific relationship between seed mass, halo mass, and redshift—providing a framework that can be implemented in cosmological simulations and tested against current and future observations.

Chapter 3

Probing the Early Universe

We have already introduced the JWST in the context of the EoR studies, as a powerful facility to probe the early Universe. We know dedicate Sec.3.1 to present in more detail the instrument and the most relevant observations, as well as the questions that arise. In Sec. 3.2, we discuss the Near-Infrared and X-ray backgrounds, which offer a complementary view of the luminous sources present in the early Universe and may provide hints of a population of accreting PBHs.

3.1 The revolutionary view of the James Webb Space Telescope

3.1.1 The JWST

The James Webb Space Telescope (JWST) is the scientific successor to the Hubble Space Telescope (HST) and stands as the most powerful space observatory ever constructed. Operating primarily in the infrared, JWST is designed to probe the formation of the first stars and galaxies in the early Universe. Its high sensitivity and wide spectral coverage in the near-infrared enable precise spectroscopy of rest-frame ultraviolet and optical emission from distant galaxies. These observations provide key physical quantities—such as redshift, metallicity, star formation rate, and gas kinematics—offering fundamental insights into the processes governing early galaxy formation and evolution.

JWST carries four main scientific instruments within the Integrated Science Instrument Module (ISIM), jointly covering the wavelength range $0.6{-}28\ \mu\mathrm{m}$ (Gardner et al., 2023):

- NIRCam (Near-Infrared Camera) provides deep imaging and slitless spectroscopy over $\sim 0.6{-}5\ \mu\mathrm{m}$. Its multi-band capabilities allow for the identification of high-redshift galaxies via the Lyman-break technique and the selection of targets for spectroscopic follow-up.
- NIRSpec (Near-Infrared Spectrograph) operates over a similar wavelength range and enables multi-object spectroscopy at multiple dispersions and resolutions. It allows efficient spectroscopic confirmation of distant galaxy candidates and accurate measurements of key emission and absorption features.
- MIRI (Mid-Infrared Instrument) extends the wavelength coverage to $\sim\ 5{-}28\ \mu\mathrm{m}$, offering imaging and medium-resolution integral-field spectroscopy. It facilitates rest-frame optical and mid-infrared diagnostics of bright high-redshift galaxies, as well as detailed studies of dust and the interstellar medium (ISM) in lower-redshift systems.
- NIRISS (Near-Infrared Imager and Slitless Spectrograph) provides wide-field slitless spectroscopy, optimized for large-area surveys and statistical studies of the high-redshift galaxy population.

An overview of the telescope's main components is shown in Fig. 3.1.

Before the launch of JWST, galaxy candidates were identified by HST and Spitzer up to $z \sim 10{-}11$, with only a handful of spectroscopic confirmations (e.g. GN-z11). JWST has since pushed this frontier dramatically: within just a few years of operation, numerous galaxies at $z \gtrsim 10{-}15$ have been discovered photometrically, and several have been spectroscopically confirmed with NIRSpec and related programs. This breakthrough has been made possible by JWST's large collecting area, exceptional infrared sensitivity, and multi-band imaging capability extending to $5\ \mu\mathrm{m}$.

The current census includes multiple robust spectroscopic detections beyond $z \sim 10$, with confirmed galaxies at $z \gtrsim 13{-}14$. These discoveries reveal the existence of luminous, massive systems only ~ 300 Myr after the Big Bang, posing major challenges to current models of galaxy formation and early cosmic evolution.

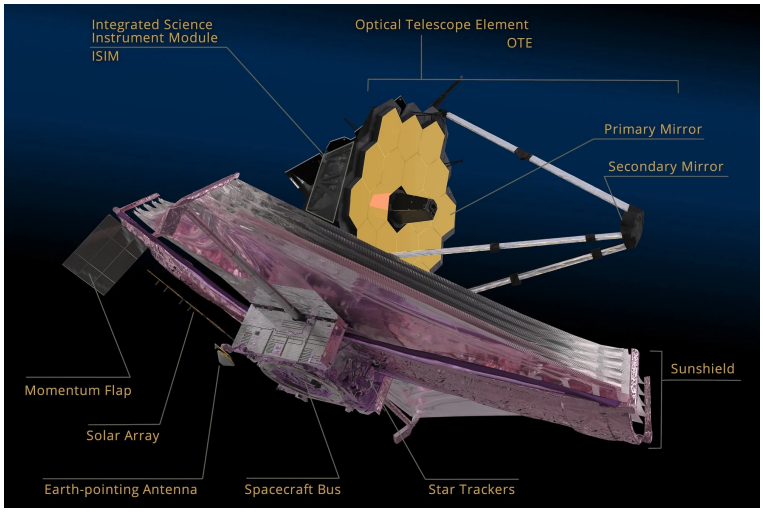

Figure 3.1: Overview of the main components of JWST. Image credit: NASA, ESA, CSA.

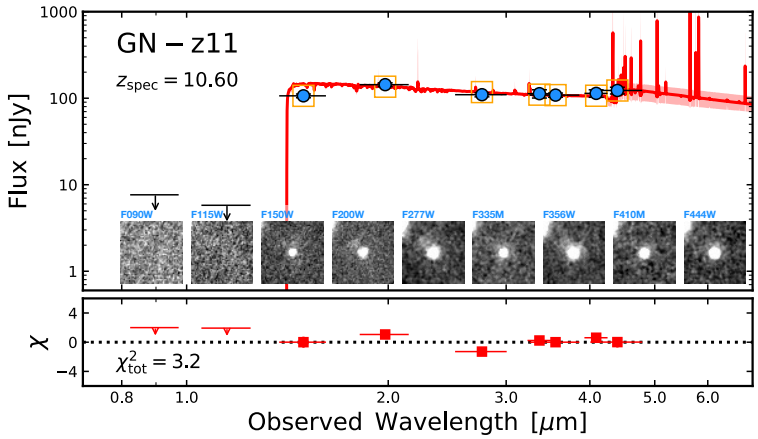

Figure 3.2: Spectral energy distribution of GN-z11, showing the prominent Lyman break between the F115W and F150W filters. From Tacchella et al. (2023).

3.1.2 The most distant galaxies

High-redshift galaxies are typically identified photometrically using the Lyman-break, or dropout, technique. As discussed in Sec. 1.5, neutral hydrogen in the intergalactic medium (IGM) absorbs rest-frame radiation blueward of the Lyα transition, producing a sharp flux discontinuity—the Lyman break—observed at a wavelength

$$\lambda_{\rm break} \simeq \lambda_\alpha (1+z), \tag{3.1}$$

where $\lambda_\alpha = 1216\,$Å is the Lyα wavelength. The corresponding redshift is then estimated as $z = \lambda_{\rm break}/\lambda_\alpha - 1$.

Photometric surveys use sets of broadband filters covering distinct wavelength ranges. The galaxy flux is measured in each filter, and the location of the flux drop identifies the break. Although the dropout method is efficient, it is not free from contamination. Galaxies with evolved stellar populations may exhibit a discontinuity at $\lambda = 3646\,$Å—the Balmer break—produced when most hydrogen atoms are in the $n = 2$ state. Radiation capable of ionising these atoms or producing Balmer lines is absorbed, mimicking the spectral signature of a Lyman break. Consequently, lower-redshift ($z \sim 4$–5) Balmer-break galaxies can imitate the colours of true high-redshift systems, making spectroscopic confirmation essential for reliable redshift measurements.

Figure 3.2 shows the spectral energy distribution of GN-z11, a galaxy at $z \simeq 10$. It was initially identified photometrically (Oesch et al., 2014) and later confirmed spectroscopically with HST (Oesch et al., 2016). JWST observations with NIRCam (Tacchella et al., 2023) and NIRSpec (Bunker et al., 2023) have refined its redshift to $z = 10.60$. The sharp flux drop between the F150W and F115W filters clearly marks the Lyman break: the galaxy is undetected in F115W but visible in all redder bands.

A major milestone has been the spectroscopic confirmation of galaxies at $z \sim 14$ in the JWST Advanced Deep Extragalactic Survey (JADES) (Eisenstein et al., 2023; Carniani et al., 2024). Their redshifts were derived from detailed modelling of the Lyman break, yielding $z = 13.90 \pm 0.17$ and $z = 14.32^{+0.08}_{-0.20}$. No strong emission lines were detected, except for a tentative C III] feature.

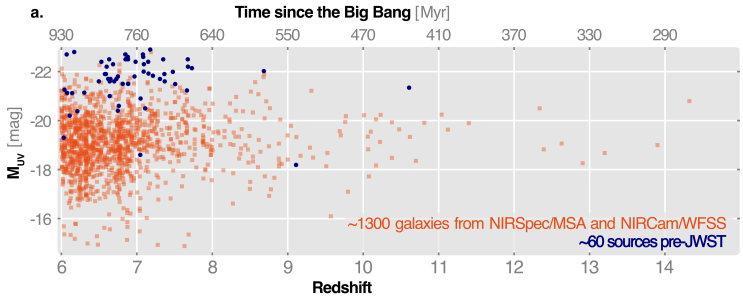

Figure 3.3: Distribution of absolute magnitudes and redshifts for spectroscopically confirmed galaxies from pre-JWST observations (blue dots) and JWST public datasets (orange squares). Adapted from Adamo et al. (2025).

The current record holder, MoM-z14, lies at $z = 14.44 \pm 0.02$ (Naidu et al., 2025), discovered in the COSMOS Legacy field (Casey et al., 2023).

The remarkable progress enabled by JWST is summarised in Fig. 3.3, which compares the redshift and UV magnitude distributions of spectroscopically confirmed galaxies before and after JWST. The telescope has not only extended the redshift frontier well beyond $z \sim 10$ but also enabled the routine detection of galaxies up to six magnitudes fainter than those observable with previous facilities.

Among galaxies at $z \gtrsim 10$, the *JWST* has spectroscopically confirmed two Lyα emitters (Witstok et al., 2025; Bunker et al., 2023), deep within the epoch of reionization (EoR) when the IGM is expected to be largely neutral. The detection of Lyα emission at such early times poses a serious challenge to our current understanding of reionization. Explaining these observations likely requires the presence of ionized bubbles surrounding the galaxies, implying that reionization may have begun earlier than previously thought. Moreover, the morphology of reionization itself strongly influences Lyα visibility, which is enhanced in scenarios where low-mass galaxies are the primary drivers of ionization (Qin & Wyithe, 2024).

An additional clue comes from the observed velocity offsets between the Lyα line and the systemic redshift, which suggest the presence of galactic outflows. In an outflowing medium, Lyα photons are Doppler-shifted out of resonance, allowing them to escape more easily through the surrounding gas. This mechanism provides a natural explanation for the observed visibility of Lyα at such high redshifts and may represent direct evidence of feedback operating in the earliest galaxies (Ferrara, 2024). Studying these outflows through the Lyα line therefore offers a unique window into the feedback processes that shaped the dawn of galaxy formation.

3.1.3 Blue Monsters and their overabundance

One of the most striking early results from JWST was the discovery of an unexpectedly large population of UV-luminous ($M_{\rm UV} \lesssim -20$) galaxies at $z \gtrsim 9$–14 (Naidu et al., 2022; Harikane et al., 2023; Robertson et al., 2024). Their number densities significantly exceed predictions extrapolated from pre-JWST observations and standard galaxy-formation models. These systems also exhibit extremely blue UV continua ($\beta < -2$) (Topping et al., 2022, 2023), earning them the nickname *"Blue Monsters"* (Ziparo et al., 2023; Ferrara et al., 2023).

The abundance of galaxies per UV magnitude is described by the UV luminosity function (UVLF). Figure 3.4 shows the UVLF at $z \sim 12$ compared with theoretical predictions made prior to JWST. While models expected a steep exponential decline at the bright end, JWST data instead suggest a shallower, nearly power-law behaviour.

The growing tension between theoretical predictions and recent observations has sparked a lively debate on how to reconcile the two. One possible explanation concerns the efficiency of star formation in high-redshift galaxies. As discussed in Sec. 1.6, several feedback mechanisms operate in the interstellar medium to regulate star formation and keep it globally inefficient. However, the physical conditions in the early Universe are expected to differ substantially from those in local galaxies. In particular, gas densities are likely much higher, a key factor that directly influences the dynamics of star formation.

Spectroscopic *JWST* observations have confirmed this expectation by resolving multiple emission lines and revealing electron densities as high as $n_e \gtrsim 10^5\ {\rm cm}^{-3}$ (Topping et al., 2024; Senchyna et al., 2024; Topping et al., 2025). In such extreme environments, the relative importance of different feedback processes changes dramatically. For giant molecular clouds (GMCs) with $n \gtrsim 3 \times 10^3\ {\rm cm}^{-3}$, the free-fall time is $t_{\rm ff} \lesssim 1\ {\rm Myr}$—shorter than the $\sim 3\ {\rm Myr}$ required for the first supernovae (SNe) to explode. As a result, SN feedback cannot act effectively to regulate star formation, leaving only early stellar feedback processes as potential regulators.

However, these early feedback channels are also expected to be weak in this regime. Stellar winds, for instance, are largely ineffective at early times: their mechanical power scales approximately as $Z^{0.9}$, making them negligible in low-metallicity environments. Only after 1–2 Myr, once stellar envelopes become metal-enriched, do winds emerge as a significant source of feedback. Photoionization feedback is also suppressed, as the corresponding H II regions remain extremely compact within the dense neutral gas. Direct radiation pressure becomes relevant only for gas surface densities $\Sigma_g \lesssim 3 \times 10^3\ M_\odot\ {\rm pc}^{-2}$ (see Sec. 4.3.2), while the clouds of

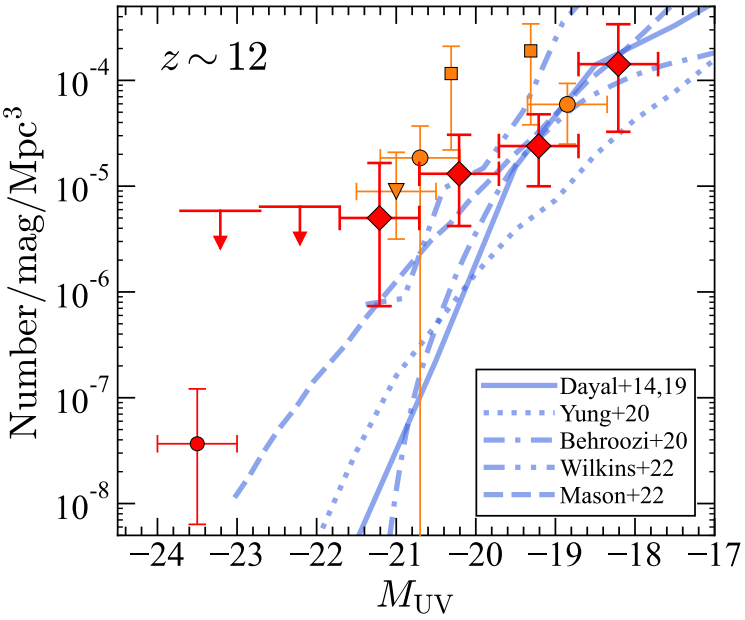

Figure 3.4: UV luminosity function at $z \sim 12$ from JWST observations (red and orange points). Blue lines indicate theoretical and empirical models. From Harikane et al. (2023).

interest here typically exceed this threshold, rendering this mechanism similarly ineffective. The same conclusion holds for dust-reprocessed infrared radiation pressure, which has been shown to have minimal impact on star formation under such conditions in full three-dimensional radiation-hydrodynamic simulations (Menon et al., 2023).

Taken together, these arguments indicate that at densities $n \gtrsim 3 \times 10^3\ \mathrm{cm}^{-3}$, none of the conventional feedback mechanisms can halt gravitational collapse. Star formation in this regime may therefore proceed essentially unimpeded, leading to so-called *feedback-free* (FF) bursts (Dekel et al., 2023), in which molecular clouds convert a large fraction—potentially up to unity—of their gas mass into stars.

Yet, this picture overlooks one crucial process: Lyα radiation pressure feedback. As introduced in Sec. 1.6, Lyα photons can exert significant forces on the gas through resonant scattering, especially in dense, metal-poor environments. This raises two fundamental questions: is truly feedback-free star formation still possible once Lyα feedback is taken into account? And if not, what is the maximum star formation efficiency permitted by Lyαradiation pressure? Part II of this thesis is devoted to addressing these questions in detail.

Another explanation proposed for the observed overabundance of bright galaxies involves modifications to the standard ΛCDM cosmological model through the introduction of PBHs. As pointed in Sec 2.3, the presence of such compact objects can alter the collapse dynamics of dark matter halos and consequently modify the halo mass function (Chapline, 1975). In particular, PBHs can accelerate the growth of structure, potentially leading to the earlier formation of galaxies and thus accounting for the apparent excess of luminous galaxies at high redshift (Liu & Bromm, 2022).

Furthermore, accreting PBHs residing at the centers of galaxies could power luminous active galactic nuclei (AGNs), thereby boosting the ultraviolet luminosity function (UVLF) to the levels observed by JWST (Matteri et al., 2025a; Matteri et al., 2025b). Beyond their relevance to the UVLF, PBHs have also attracted growing attention in light of puzzling JWST observations of black holes in the early Universe. The luminosity function of AGNs spectroscopically identified by JWST exceeds by at least an order of magnitude the values predicted by extrapolating quasar luminosity functions at $z \sim 5$–7 (Greene et al., 2024; Kokorev et al., 2024). In addition, the black holes detected at $z \gtrsim 7$ appear systematically overmassive relative to their host stellar masses, posing significant challenges for standard models of black hole seeding and growth (Furtak et al., 2024; Maiolino et al., 2024a; Kokorev et al., 2023).

These findings have motivated the development of semi-analytical frameworks linking the seeding and coevolution of black holes and galaxies to an underlying population of PBHs (Dayal, Pratika, 2024; Dayal & maiolino, 2025; Ziparo et al., 2024). Importantly, a population of accreting PBHs in the early Universe would generate radiation backgrounds well before the formation of the first stars. This raises two fundamental questions: could such backgrounds be detected observationally, and what impact would they have on the thermal and ionization history of the early Universe? In the next section, we describe the relevant radiation backgrounds associated with PBHs, and we return to these questions in Part III of this thesis.

3.2 Cosmic Backgrounds

In this section, we discuss the two cosmic radiation backgrounds most directly linked to PBHs. Observations indicate that part of these diffuse signals cannot be explained by known astrophysical populations, suggesting that PBHs could play a role in completing the picture.

3.2.1 The Near-Infrared Background

The Cosmic Infrared Background (CIB) is the diffuse infrared radiation of cosmological origin detected across wavelengths between 1 and $500\ \mu\mathrm{m}$. Its near-infrared component, the Near-Infrared Background (NIRB), extends from 1 to $10\ \mu\mathrm{m}$, corresponding to photon energies of 0.12–$1.2\ \mathrm{eV}$ or frequencies of 0.3–$3\ \mathrm{THz}$.

The concept of the CIB dates back to the work of Partridge and Peebles (1967), who predicted that ultraviolet emission from early galaxies would be redshifted into the infrared, yielding a flux of $\sim 100\ \mathrm{nW\,m^{-2}\,sr^{-1}}$ in the 5–$15\ \mu\mathrm{m}$ range (Partridge & Peebles, 1967). Measuring this diffuse light provides a way to trace the first luminous sources, even when they are too faint to be individually resolved.

Direct measurements of the CIB, however, are challenging (Matsumoto et al., 2015; Matsuura et al., 2017). The signal is contaminated by bright foregrounds from the Solar System and the Milky Way (Leinert et al., 1998): sunlight scattered by interplanetary dust forms the Zodiacal Light (ZL), while starlight scattered by interstellar dust produces the Diffuse Galactic Light (DGL). These local components must be carefully subtracted to recover the cosmological background.

A more reliable way to study the CIB is to analyse its spatial fluctuations, which are less sensitive to foreground subtraction errors. Observations taken six months apart can be differenced to remove isotropic components such as ZL and DGL, isolating the intrinsic sky variations. Using this technique, Kashlinsky et al. (2005) detected an excess of NIRB fluctuations exceeding the expectations from known galaxy populations. Subsequent analyses (Matsumoto et al., 2011; Cooray et al., 2012a) and more recent work (Kashlinsky et al., 2025) confirmed the presence of this excess.

Figure 3.5 shows the angular power spectrum of NIRB fluctuations as a function of multipole moment l. Models including both low-redshift ($z < 5$) and high-redshift ($z > 5$) galaxies underestimate the observed power on large angular scales, implying the existence of additional sources.

One possibility is that the excess originates from Direct Collapse Black Holes (DCBHs) (Yue et al., 2013b). These are massive black holes thought to form in atomic-cooling halos exposed to strong Lyman–Werner radiation, which suppresses molecular hydrogen formation and prevents fragmentation, allowing the gas to collapse directly into a black hole. DCBHs are also expected to emit X-rays, potentially linking the NIRB to the unresolved X-ray background.

An alternative explanation points to PBHs. As discussed in Sec. 2.3, PBHs are viable dark matter candidates and would therefore follow the large-scale distribution of dark matter, clustering within halos and along the filaments of the IGM. Gas accreting onto PBHs can emit radiation, contributing to the diffuse background fluctuations observed in the NIRB. In Chap. 7, we develop a detailed model of this scenario and present quantitative predictions for the NIRB signal expected from PBHs.

For completeness, it is worth noting that intra-halo light—emission from diffuse stellar components produced during galaxy mergers—has also been proposed as a possible low-redshift contributor to the observed excess (Cooray et al., 2012a).

3.2.2 The X-ray Background

The Cosmic X-ray Background (CXB) represents the diffuse X-ray radiation accumulated over cosmic time, spanning the energy range 0.5–$100\ \mathrm{keV}$. Observations from ROSAT, CHANDRA, and XMM-Newton have established that most of the CXB originates from Active Galactic Nuclei (AGN). Nevertheless, a faint unresolved component persists even after accounting for all identified sources.

Cappelluti et al. (2017a) analysed deep-field CHANDRA observations and measured an unresolved X-ray flux of $9.6\times10^{-3}\ \mathrm{nW\,m^{-2}\,sr^{-1}}$ in the 0.5–$2\ \mathrm{keV}$ band and $2.1\times10^{-2}\ \mathrm{nW\,m^{-2}\,sr^{-1}}$ in the 2–$10\ \mathrm{keV}$ band. Remarkably, follow-up analyses revealed a correlation between the spatial fluctuations of the CXB and those of the NIRB (Cappelluti et al., 2017b). An excess cross-power spectrum appears on angular scales $\theta \gtrsim 20$ arcsec, as shown in Fig. 3.6.

The solid line in the figure represents the combined contribution from known $z < 6$ sources—AGN, star-forming galaxies, and hot intracluster gas—yet these components cannot explain the observed excess.

The CXB-NIRB correlation implies that at least part of both the CXB and the NIRB may arise from the same underlying population. To quantify this link, Cappelluti et al. (2017b) introduced the coherence between the two bands, defined as

$$\mathcal{C}_{IR,X} = \frac{P^2_{IR,X}}{P_{IR}P_X}, \tag{3.2}$$

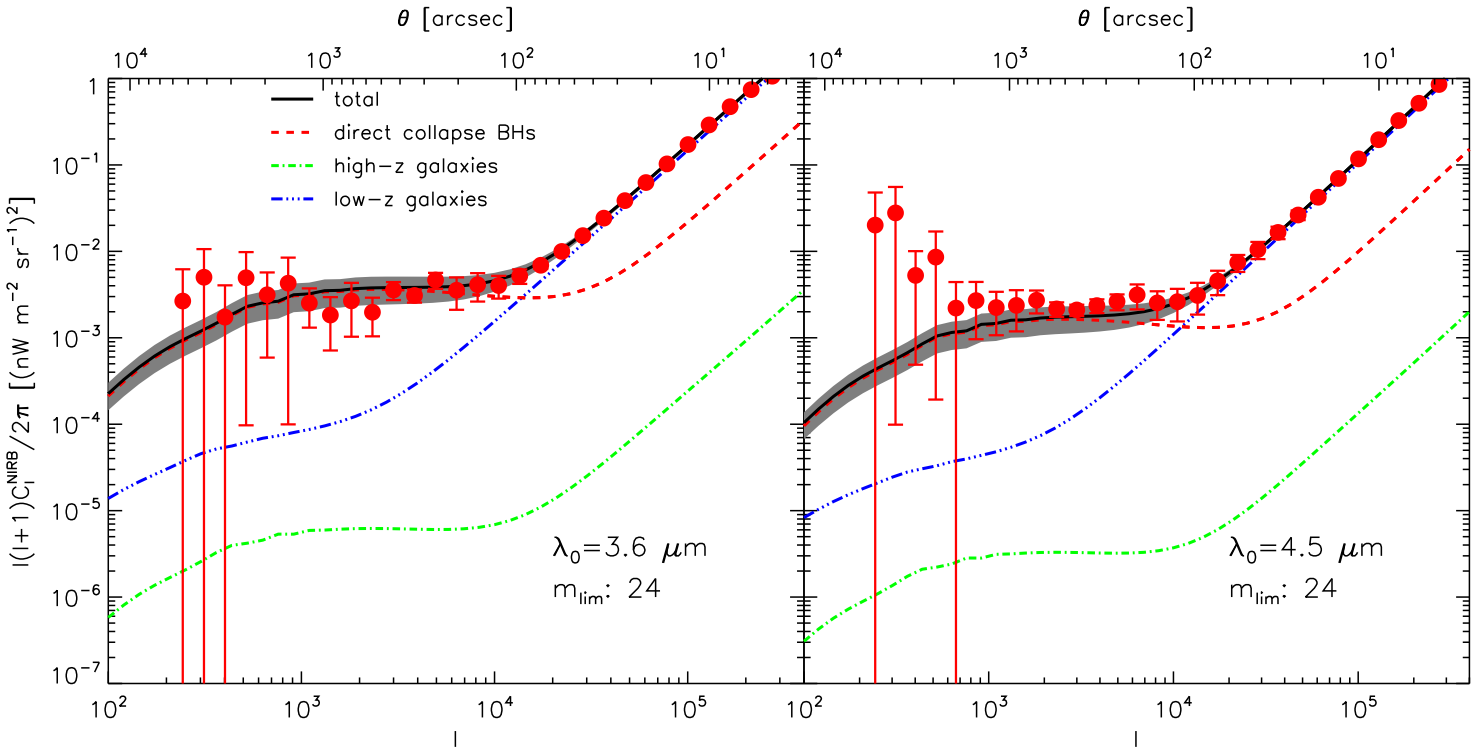

Figure 3.5: Angular power spectrum of NIRB fluctuations as a function of multipole l (or angular scale). Data from Cooray et al. (2012a) are shown as red points. Blue and green curves represent the contributions from low- and high-redshift galaxies, respectively, while the red dashed line shows the predicted signal from DCBHs. From Yue et al. (2013b).

where P_{IR} and P_X denote the auto-power spectra of the infrared and X-ray signals, respectively. They measured $\mathcal{C}_{IR,X} = 0.14$–$0.20$, indicating that roughly 15–20% of the unresolved emission in both bands originates from the same sources.

If a population contributes fractions f_{IR} and f_X of the total unresolved flux in each band, the expected coherence is $\mathcal{C}_{12} \simeq f_{IR}^2 f_X^2$. Such a level of correlation arises naturally if the same objects emit in both the infrared and X-ray bands, as in the case of accreting black holes. In this framework, the observed coherence would be consistent—at least qualitatively—with radiation from PBHs accreting in the early Universe.

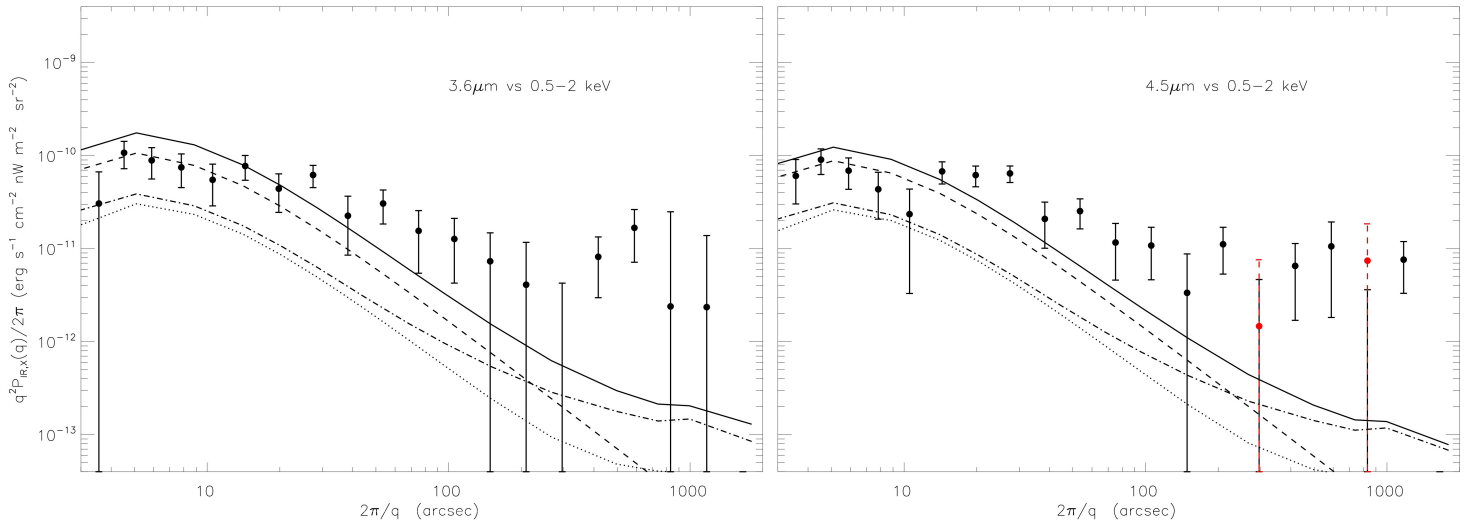

Figure 3.6: Cross-power spectrum between the NIRB at $3.6\ \mu\mathrm{m}$ and $4.5\ \mu\mathrm{m}$ and the CXB in the $0.5{-}2\ \mathrm{keV}$ band. The solid line shows the total contribution from known $z < 6$ populations: AGN (dashed), star-forming galaxies (dot–dashed), and hot intracluster gas (dotted). From Cappelluti et al. (2017b).

Part II

Lyα feedback in the Early Universe

Chapter 4

The Lyα line

We have already introduced the Lyα line in the context of the EoR and its crucial role in tracing the emergence of the first galaxies. We now turn our attention to the physical mechanisms that govern this remarkable spectral feature. In Sec. 4.1 we examine how Lyα photons are produced, discussing in detail the emission processes and the relevant atomic transitions. We then explore the propagation of these photons through neutral hydrogen in Sec. 4.2, where we introduce the Lyα radiative transfer problem and outline the methods used to approach it. Finally, Sec. 4.3 presents the concept of Lyα radiation pressure, which forms the theoretical foundation for the feedback models developed in Chaps. 5–6.

4.1 Introductory physics

Lyα photons are emitted when an electron in a neutral hydrogen atom transitions from the first excited state ($2p$) to the ground state ($1s$). The energy, wavelength, and frequency of the transition are

$$E_\alpha = 10.2\,\mathrm{eV}, \qquad \lambda_\alpha = 1216\,\text{Å}, \qquad \nu_\alpha = 2.47 \times 10^{15}\,\mathrm{Hz}. \tag{4.1}$$

This transition represents one of the most efficient cooling and diagnostic channels in astrophysics. Lyα emission is a natural by-product of photoionisation: ionising photons from young, massive stars (or other energetic sources) produce free protons and electrons, which later recombine and cascade radiatively from excited levels, frequently producing Lyα photons. An alternative channel involves collisional excitation of neutral hydrogen followed by radiative de-excitation, although in typical star-forming regions recombination emission dominates the overall Lyα output.

When an electron is captured by a proton, the resulting hydrogen atom is generally formed in an excited state labelled by its principal and orbital quantum numbers (n, l). The atom then undergoes a radiative cascade through intermediate states (n_i, l_i) until it reaches the ground level. Figure 4.1 schematically illustrates the most relevant energy levels and the main cascade paths that can produce Lyα emission.

The probability that a recombination event ultimately produces a Lyα photon can be written as

$$P_\alpha(T) = \sum_{n_{\min}}^{\infty} \sum_{l=0}^{n-1} f_{nl}(T)\, P(n, l \to \mathrm{Ly}\alpha), \tag{4.2}$$

where $f_{nl}(T)$ denotes the fraction of recombinations directly into the (n, l) level and $P(n, l \to \mathrm{Ly}\alpha)$ is the probability that the subsequent cascade results in Lyα emission. The lower limit $n_{\min}$ depends on the optical thickness of the gas. In optically thick environments, higher-order Lyman-series photons are rapidly reabsorbed, preventing direct recombinations to the ground state — the so-called case B recombination($n_{\min} = 2$). In contrast, optically thin gas allows direct recombination to the ground state, known as case A recombination ($n_{\min} = 1$).

Because the level populations depend on the gas temperature, so does $P_\alpha(T)$. In typical HII regions, where $T \simeq 10^4\,\mathrm{K}$ and case B conditions prevail, the probability that a recombination yields a Lyα photon is $P_\alpha \simeq 0.68$ (Cantalupo et al., 2008), often approximated as $2/3$ for simplicity.

For a source emitting ionising photons at a rate $\dot{N}_{\mathrm{ion}}$, the resulting Lyα luminosity from its surrounding HII region can be expressed as

$$L_\alpha = \frac{2}{3}(1 - f_{\mathrm{esc}}) E_\alpha \dot{N}_{\mathrm{ion}}, \tag{4.3}$$

where f_{esc} denotes the fraction of ionising photons escaping the region. In dense, star-forming environments this fraction is generally negligible, as nearly all ionising photons are absorbed locally.

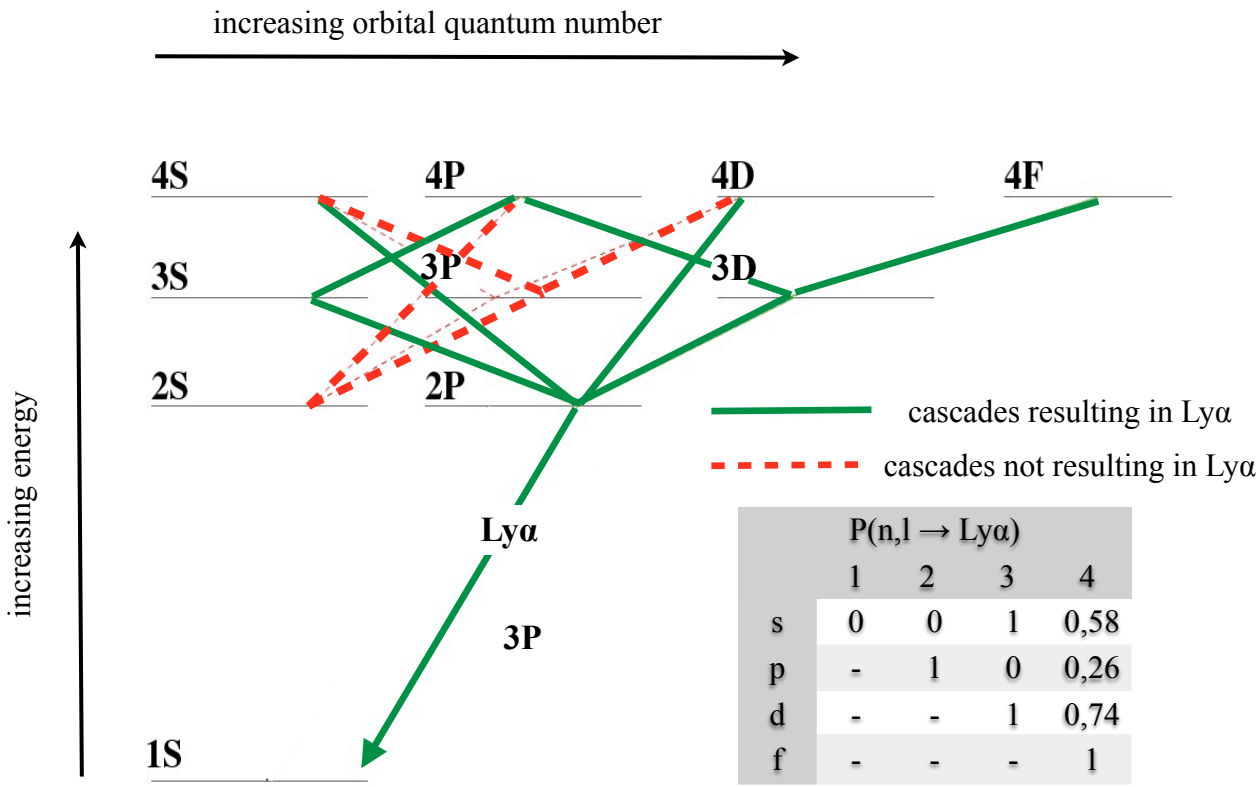

P(n,l → Lyα)	1	2	3	4
s	0	0	1	0,58
p	-	1	0	0,26
d	-	-	1	0,74
f	-	-	-	1

Figure 4.1: Energy levels of hydrogen and the main radiative cascades leading to Lyα emission. The lower-right panel shows the probability $P(n, l \rightarrow \mathrm{Ly}\alpha)$ that a cascade from (n, l) yields a Lyα photon. From Dijkstra (2014).

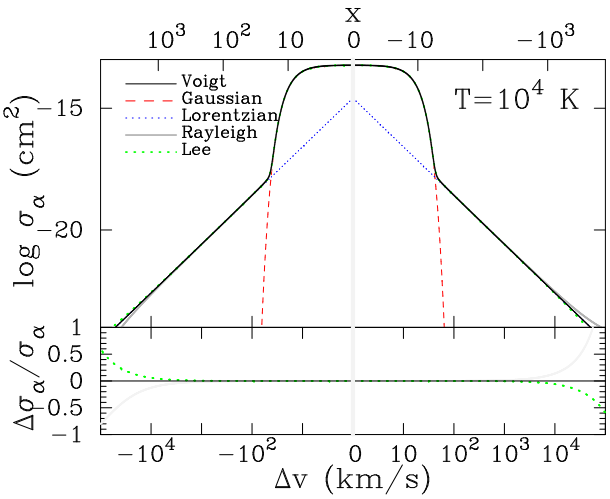

Figure 4.2: Voigt profile (solid black), compared with its Gaussian (dashed red) and Lorentzian (dotted blue) components, as a function of normalized frequency or velocity shift. Rayleigh approximation is shown in gray, while the Lee profile, derived from full quantum-mechanical treatment, in green. From Dijkstra (2014).

Once emitted, Lyα photons resonantly scatter off the neutral hydrogen that surrounds the ionised bubble. The strength of this interaction is described by the Lyα scattering cross-section $\sigma_\alpha(\nu, T)$, which depends on both frequency and temperature. It is often convenient to express frequency deviations in dimensionless form,

$$x = \frac{\nu - \nu_\alpha}{\Delta\nu_\alpha}, \tag{4.4}$$

where $\Delta\nu_\alpha = \nu_\alpha\sqrt{2k_BT/m_pc^2} \equiv \nu_\alpha v_{\rm th}/c$ is the Doppler width due to thermal motions. The cross-section is then

$$\sigma_\alpha(x, T) = \sigma_0 \frac{a_\nu}{\pi} \int_{-\infty}^{\infty} {\rm d}y \frac{e^{-y^2}}{(y-x)^2 + a_\nu^2} \equiv \sigma_0 \mathcal{H}(a_\nu, x), \tag{4.5}$$

$$\sigma_0 = \frac{f_\alpha}{\sqrt{\pi}\Delta\nu_\alpha}\frac{\pi e^2}{m_e c} = 5.9\times10^{-13}\Big(\frac{T}{100\,{\rm K}}\Big)^{-1/2}\,{\rm cm}^{-2}, \tag{4.6}$$

where $f_\alpha = 0.416$ is the Lyα oscillator strength, and the Voigt parameter is $a_\nu = 4\pi A_\alpha/\Delta\nu_\alpha = 4.7\times10^{-3}(T/100\,{\rm K})^{-1/2}$, with A_α the Einstein coefficient of the transition.

The Voigt profile $\mathcal{H}(a_\nu, x)$ represents the convolution of two broadening mechanisms: a Lorentzian (natural) component, arising from the finite lifetime of the excited state, and a Gaussian (thermal) component produced by the Maxwellian velocity distribution of the atoms,

$$\phi^L(\nu) = \frac{A_\alpha}{4\pi^2}\frac{1}{(\nu-\nu_\alpha)^2 + (A_\alpha/4\pi)^2}, \qquad \phi^G(\nu) = \frac{1}{\Delta\nu_\alpha\sqrt{\pi}}\exp\Big[-\frac{(\nu-\nu_\alpha)^2}{\Delta\nu_\alpha^2}\Big]. \tag{4.7}$$

Near the line centre, the Gaussian component dominates; far from it, the Lorentzian wings become more important. These regimes can be approximated by

$$\mathcal{H}(x) \approx \begin{cases} e^{-x^2}, & |x| < x_{\rm crit} \\ \dfrac{a_\nu}{\sqrt{\pi}x^2}, & |x| > x_{\rm crit} \end{cases} \tag{4.8}$$

with $x_{\rm crit} \sim 2$–4 depending on temperature (Smith et al., 2015). The distinction between the core and wing regimes has deep implications for Lyα scattering, as discussed in Sec. 4.2. Figure 4.2 illustrates these components for a gas at $T = 10^4$ K.

4.2 Lyα radiative transfer

Understanding how Lyα photons propagate through the interstellar and intergalactic medium is key to unveiling their role in galaxy formation and feedback. Once emitted, these photons do not travel freely: they resonantly interact with neutral hydrogen, undergoing

countless scatterings that can alter both their spatial distribution and spectral profile. This complex process is described by the theory of Lyα radiative transfer.

4.2.1 The Lyα radiative transfer equation

To quantify how the Lyα radiation field evolves in time, space, and frequency, we consider the specific intensity $I(\nu, \mathbf{r}, \mathbf{n}, t)$ at frequency ν, position $\mathbf{r}$, direction $\mathbf{n}$, and time t. In the comoving frame of the gas, the evolution of I is governed by the general radiative transfer (RT) equation (Castor, 2004; Nebrin et al., 2025):

$$\frac{1}{c}\frac{\partial I}{\partial t} + \mathbf{n}\cdot\nabla I - \frac{1}{c}\mathbf{n}\cdot\nabla\mathbf{u}\cdot\mathbf{n}\,\nu\frac{\partial I}{\partial \nu} = j_s - (\alpha+\alpha_c)I + \int \mathrm{d}\nu' \int \mathrm{d}^3\mathbf{n}'\, \alpha I(\nu') R(\nu,\nu',\mathbf{n},\mathbf{n}'). \tag{4.9}$$

Here $\mathbf{u}$ denotes the gas velocity field, which Doppler-shifts the photons as they scatter. The source function j_s represents the local emission of Lyα photons—either from recombination or collisional excitation—while the absorption coefficient $\alpha(\mathbf{r}) = n_{\rm HI}(\mathbf{r})\,\sigma_\alpha\,\mathcal{H}(\nu)$ accounts for resonant scattering by neutral hydrogen. The term α_c represents continuum absorption, primarily due to dust grains.

The last term on the right-hand side of Eq. 4.9 encapsulates the redistribution of photons in both frequency and direction rather than their destruction. The redistribution function $R(\nu,\nu',\mathbf{n},\mathbf{n}')$ specifies the probability that a photon initially at $(\nu',\mathbf{n}')$ is scattered into $(\nu,\mathbf{n})$ after an interaction.

The general RT equation cannot be solved analytically in closed form. A common simplification is to neglect the time derivative and work under the static approximation, assuming a steady-state radiation field. Even so, analytical progress remains limited, and numerical approaches become indispensable. The most powerful among these are Monte Carlo Radiative Transfer (MCRT) methods (Smith et al., 2015; Michel-Dansac et al., 2020; Byrohl et al., 2021), which trace the trajectories of discrete photon packets through the medium. Each packet undergoes a stochastic sequence of scattering events, during which its frequency and direction are updated according to the relevant physical laws. Such simulations have been extensively used in post-processing of cosmological simulations, allowing direct comparison between theoretical predictions and observed Lyα spectra (Verhamme et al., 2006; Smith et al., 2022). However, MCRT techniques are computationally expensive—particularly in highly opaque environments ($\tau \gtrsim 10^6$)—and are thus ill-suited for problems that require coupling Lyα radiative transfer with gas dynamics. So far, full radiation–hydrodynamic simulations of this kind have only been performed in one dimension, mostly to study the outflows driven by Lyα radiation pressure in early galaxies (Smith et al., 2017).

To gain qualitative insight into the diffusion of Lyα photons, it is helpful to examine the statistical properties of the redistribution function (Osterbrock, 1962), namely the expectation values of the root-mean-square and mean frequency change per scattering:

$$E(\sqrt{\Delta x^2}\,|\,x_{\rm in}) = 1, \tag{4.10}$$

$$E(\Delta x\,|\,x_{\rm in}) = 1, \quad |x_{\rm in}| \gg 1. \tag{4.11}$$

The first relation implies that the root-mean-square frequency change per scattering is approximately one Doppler width. Thus, a photon absorbed far in the wing of the line tends to remain in the wing after scattering—facilitating its escape. The second relation indicates that photons absorbed in the far wings have a mild tendency to drift back toward the line core. In other words, photons far from line centre will return to the core after roughly $N_{\rm scat}\sim x^2$ scatterings.

Consider now a Lyα source embedded in the centre of a static, homogeneous cloud of radius R and very large optical depth ($\tau \gtrsim 10^6$). Photons are emitted near line centre, where the mean free path is exceedingly short. Occasionally, however, a photon is scattered into the wing at frequency offset x, where the mean free path grows as

$$\lambda_{\rm mfp}(x) \simeq \frac{R}{\tau\,\mathcal{H}(x)} \simeq \frac{R\sqrt{\pi}x^2}{a_\nu \tau},$$

using the wing approximation of the Voigt profile. Because each scattering is a random step, the photon's spatial displacement behaves like a random walk, with total distance $\sim \sqrt{N_{\rm scat}}\lambda_{\rm mfp}$. Escape occurs when this distance becomes comparable to the size of the cloud, that is, when $N_{\rm scat}\lambda_{\rm mfp} \simeq R$. This condition implies that photons escape predominantly at frequencies

$$x_{\rm esc} = \pm(a_\nu\tau/\sqrt{\pi})^{1/3},$$

producing a characteristic double-peaked emergent Lyα spectrum.

The total time spent by photons scattering before escaping—the *trapping time*—can be estimated as

$$t_{\rm trapp} \sim N_{\rm scat}\lambda_{\rm mfp}/c = x_{\rm esc}R/c \equiv x_{\rm esc}t_{\rm cross}, \tag{4.12}$$

where $t_{\rm cross} = R/c$ is the light-crossing time of the cloud. Because of the prolonged trapping, the local Lyα energy density is significantly enhanced relative to a freely streaming field.

This enhancement directly translates into a stronger radiation force. By dimensional analysis, the trapping time satisfies $t_{\rm trapp} \sim U_\alpha/L_\alpha$, where U_α is the total energy stored in Lyα photons. The resulting force on the gas is

$$F_\alpha \sim \frac{U_\alpha}{R} \sim \frac{t_{\rm trapp}}{t_{\rm cross}}\frac{L_\alpha}{c}. \tag{4.13}$$

Hence, multiple scatterings can amplify the radiation pressure by a factor $\sim t_{\rm trapp}/t_{\rm cross} \propto (a_\nu\tau)^{1/3}$ compared to the single-scattering limit. For a cloud at $T = 100$ K and optical depth $\tau = 10^9$, the resulting force is about 170 times stronger than the simple L_α/c estimate.

While the reasoning above offers useful intuition, quantitative validation requires analytical or numerical solutions of the transfer equation. A powerful simplification is the *Fokker–Planck approximation* (Rybicki & dell'Antonio, 1994), which replaces the redistribution integral with a Taylor expansion in frequency:

$$\int {\rm d}\nu' \int {\rm d}^3\mathbf{n}'\, \alpha I(\nu') R(\nu,\nu',\mathbf{n},\mathbf{n}') = (1-p_d)\mathcal{H}J + (1-p_d)\frac{1}{2}\frac{\partial}{\partial x}\Big(\mathcal{H}\frac{\partial J}{\partial x} + 2\bar{x}\mathcal{H}J\Big). \tag{4.14}$$

Here p_d is the photon destruction probability, $\bar{x} = h\Delta\nu_\alpha/(2k_BT)$ is the recoil parameter, and $4\pi J(\nu,\mathbf{r},t) = \int {\rm d}\Omega\, I(\nu,\mathbf{r},\mathbf{n},t)$ denotes the angle-averaged intensity.

An additional simplification, known as the *Eddington approximation*, assumes that the radiation field is nearly isotropic in the comoving frame—a valid assumption in high optical depth conditions where frequent scattering redistributes the photon directions. Under these approximations, Eq. 4.9 reduces to a diffusion-like form:

$$\frac{1}{\alpha_0}\nabla\cdot\Big(\frac{1}{\alpha_0}\nabla J\Big) + \frac{\nabla\cdot\mathbf{u}}{v_{\rm th}\alpha_0}\mathcal{H}\frac{\partial J}{\partial x} = -\frac{3\mathcal{H}j_s}{\alpha_0} + 3\Big(p_d\mathcal{H}^2 + \frac{\alpha_c}{\alpha_0}\mathcal{H}\Big)J - \frac{3}{2}(1-p_d)\Big(\mathcal{H}\frac{\partial J}{\partial x} + 2\bar{x}\mathcal{H}J\Big). \tag{4.15}$$

Neglecting the explicit time dependence renders Eq. 4.15 analytically tractable. Recent work by Nebrin et al. (2025) has provided exact steady-state solutions under the assumptions of spherical symmetry, constant gas density, and a homologous velocity profile $u(r) = v_{\rm max}r/R_c$. These results, which naturally recover the static limit for $v_{\rm max} = 0$, offer the first rigorous analytical framework for Lyα transfer in expanding or contracting media with all the relevant absorption and destruction processes. A full derivation is beyond the scope of this discussion and can be found in the cited reference.

4.2.2 Analytical solutions for test cases

Analytical solutions, although restricted to idealised setups, offer valuable physical intuition about the behaviour of Lyα photons in realistic environments. They provide transparent benchmarks for testing numerical codes and help identify how key parameters—such as optical depth or source geometry—shape the emergent spectrum and radiation field.

We address here the simplest possible configuration: a static, homogeneous, and dust-free spherical cloud. Neglecting recoil and Lyα photon destruction, the radiative transfer equation simplifies to (Lao & Smith, 2020)

$$\tilde{\nabla}^2\tilde{J} + \frac{\partial^2\tilde{J}}{\partial\tilde{x}^2} = \frac{\eta(r)}{\alpha_0}\,\delta(\tilde{x}), \tag{4.16}$$

where the tilde notation denotes dimensionless variables defined through the transformations

$$\tilde{\nabla} = \frac{\tau_{\rm cl}}{\alpha_0}\nabla, \quad {\rm d}\tilde{x} = \sqrt{\frac{2}{3}}\frac{{\rm d}x}{\tau_{\rm cl}\mathcal{H}(x)}, \quad J = \tilde{J}\,L_\alpha\tau_{\rm cl}\frac{\sqrt{6}}{4\pi}. \tag{4.17}$$

Here L_α is the total Lyα luminosity of the source, $\tau_{\rm cl}$ is the optical depth of the cloud, and $\eta(r)$ represents the emissivity profile. For a point-like source located at the centre, one has $\eta(r) = \delta(r)/(4\pi r^2)$.

Equation 4.17 highlights that Lyα radiative transfer can be interpreted as a diffusion process operating simultaneously in both physical space and frequency space. In this simplified case, an analytical solution for the dimensionless intensity $\tilde{J}(\tilde{r},\tilde{x})$ exists (Dijkstra, 2014; Lao & Smith, 2020):

$$J(\tilde{r},\tilde{x}) = \frac{L_\alpha\sqrt{6}}{64\pi R_{\rm cl}^2\tau_{\rm cl}\mathcal{H}(x)}\frac{\sin(\pi\tilde{r})}{\cosh(\pi\tilde{x}) - \cos(\pi\tilde{r})}, \tag{4.18}$$

with the spatial coordinate related to the dimensionless one by ${\rm d}r = \alpha_0\,{\rm d}\tilde{r}/\tau_{\rm cl}$.

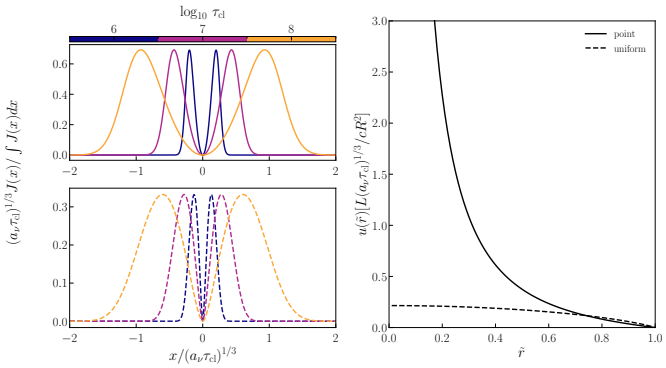

Figure 4.3: *Top left*: Normalised emergent spectrum from a homogeneous cloud with a central point source, shown for different optical depths ($\tau_{\rm cl} = 10^6, 10^7, 10^8$; blue, purple, and yellow respectively). *Bottom left*: Same, but for a uniform source distribution. *Right*: Frequency-averaged energy density as a function of normalized radius for the point-source (solid line) and uniform-source (dashed line) cases. The energy density profile is independent of optical depth.

Of particular interest is the spectrum emerging at the surface of the cloud ($r = R_{\rm cl}$):

$$\frac{J(x)}{\int_{-\infty}^{\infty} \mathrm{d}x\, J(x)} = \frac{\sqrt{\pi^3}}{24}\frac{x^2}{a_\nu\tau_{\rm cl}}\,\mathrm{sech}^2\left(\sqrt{\frac{\pi^3}{54}}\frac{x^3}{a_\nu\tau_{\rm cl}}\right). \tag{4.19}$$

The spectrum peaks at $x_{\rm esc} = \pm 0.93\,(a_\nu\tau_{\rm cl})^{1/3}$ (see Fig. 4.3), in excellent agreement with the qualitative expectations discussed in Sec. 4.2.

Another key diagnostic is the frequency-averaged energy density $u(r)$, which governs the local radiation pressure exerted on the gas, since $f_\alpha \propto \nabla u$. For a static, homogeneous cloud with a central point source, the energy density profile is

$$u(\tilde{r}) = \frac{L_\alpha}{cR^2}\Gamma\!\left(\frac{1}{3}\right)\frac{(2a_\nu\tau_{\rm cl})^{1/3}}{2\pi^{3/2}}\tilde{r}^{-1}\,\mathrm{Im}\left[\mathrm{Li}_{1/3}(e^{i\pi\tilde{r}})\right], \tag{4.20}$$

where $\Gamma(z)$ and $\mathrm{Li}_s(z)$ denote the Gamma and polylogarithm functions, respectively.

These expressions can be directly applied to Lyα transport in the idealised case of a central ionising source surrounded by a dense, neutral envelope—conditions typical of compact HII regions. In realistic star-forming clouds, however, not all stars form exactly at the centre: ionising and Lyα sources are often spatially distributed throughout the cloud. To capture this, it is useful to generalise the model to an extended source configuration.

If Lyα emission is uniformly distributed across the cloud volume, the emissivity becomes constant, $\eta(r) = 3/(4\pi R^3)$. Substituting this profile into Eq. 4.16 yields analytical solutions analogous to the point-source case, both for the emergent spectrum and for the energy density:

$$\frac{J(x)}{\int_{-\infty}^{\infty} \mathrm{d}x\, J(x)} = -\sqrt{\frac{6}{\pi}}\frac{x^2}{a_\nu\tau_{\rm cl}}\ln\left[1 - e^{-\sqrt{\frac{2\pi^3}{27}}\frac{|x^3|}{a_\nu\tau_{\rm cl}}}\right], \tag{4.21}$$

$$u(r) = \frac{3L_\alpha}{cR^2}\Gamma\left(\frac{1}{3}\right)\frac{(2a_\nu\tau_{\rm cl})^{1/3}}{2\pi^{7/2}}\tilde{r}^{-1}\mathrm{Im}\left[\mathrm{Li}_{1/3}(-e^{-i\pi\tilde{r}})\right]. \tag{4.22}$$

Figure 4.3 compares the emergent spectra and energy densities for both point-like and spatially extended sources.

The comparison reveals that the energy density profile is significantly flatter in the uniform-source case. This behaviour arises because the spatially extended emission produces partial flux cancellation, leading to weaker energy density gradients across the cloud. As we will see in the next section, this reduction in gradient translates directly into a lower net radiation force on the gas, with relevant consequences for Lyα feedback dynamics.

4.3 Lyα feedback

In Sec. 4.2, we anticipated that resonant scattering can substantially amplify the momentum transferred to the gas by Lyα photons. There, we derived intuitive scaling relations based on simple physical arguments. Equipped with the analytical solutions of Lyα radiative transfer, we can now move beyond intuition and quantify this effect rigorously. In this section we introduce the *force multiplier*,

which measures the enhancement of the radiative force relative to the single-scattering limit, and we explore under which physical conditions Lyα feedback is expected to dominate over other forms of stellar feedback.

4.3.1 The force multiplier

The fundamental quantity that encapsulates the dynamical importance of Lyα radiation pressure is the *force multiplier*, M_F. It is defined as the ratio between the total Lyα force acting on a gas distribution and the direct (single-scattering) radiation force:

$$M_F = \frac{F_\alpha}{L_\alpha/c} = L_\alpha^{-1} \iint \mathrm{d}x\, \mathrm{d}V\, \alpha\mathcal{F} = \frac{c}{3L} \int \mathrm{d}V\, \nabla u, \tag{4.23}$$

where the Lyα flux $\mathcal{F}$ has been expressed using Fick's law, $\mathcal{F} = -c\nabla u/3\alpha$, valid in optically thick conditions. The force multiplier is an integrated measure of the overall momentum coupling between the radiation field and the gas; it depends directly on the spatial gradient of the Lyα energy density $u(r)$.

Using the analytical solutions for $u(r)$ derived for static, homogeneous, dust-free clouds, we can evaluate M_F explicitly. Substituting Eqs. 4.20–4.22 into Eq. 4.23 gives (Lao & Smith, 2020):

$$M_F^{\mathrm{point}} \simeq 3.51(a_\nu \tau_{\mathrm{cl}})^{1/3}, \tag{4.24}$$

$$M_F^{\mathrm{unif}} \simeq 0.51(a_\nu \tau_{\mathrm{cl}})^{1/3}, \tag{4.25}$$

for point-like and spatially uniform sources, respectively.

To appreciate the magnitude of these values, consider a typical molecular cloud where feedback-free bursts of star formation might occur. Such clouds generally have densities of $n_{\mathrm{HI}} \sim 10^{3.5}\ \mathrm{cm}^{-3}$ and radii of $R \sim 15\ \mathrm{pc}$. At a temperature of $T \sim 10^4\ \mathrm{K}$, these parameters correspond to an enormous optical depth of $\tau_{\mathrm{cl}} \sim 8 \times 10^9$, yielding a force multiplier of approximately $M_F \sim 500$. This indicates that, in the absence of dust, Lyα radiation pressure could exceed the single-scattering limit by orders of magnitude.

The large enhancement derived above assumes dust-free conditions. In practice, however, even early galaxies at high redshift show evidence of non-negligible metal enrichment, with typical metallicities of $Z/Z_\odot \sim 0.02$ (Curti et al., 2024). Dust absorption inevitably reduces the number of effective Lyα scatterings, thereby lowering M_F.

A simple but insightful way to incorporate the effect of dust is through the parameter $\epsilon \equiv \alpha_c/\alpha = \sigma_d/\sigma_\alpha$, where σ_d is the dust absorption cross-section (Hansen & Oh, 2006; Tomaselli & Ferrara, 2021). Using Milky Way dust properties (Weingartner & Draine, 2001), one obtains

$$\epsilon \simeq 2.73 \times 10^{-8} \Big(\frac{T}{10^4\ \mathrm{K}}\Big)\Big(\frac{D}{D_\odot}\Big), \tag{4.26}$$

where D is the dust-to-gas ratio.

It is possible to define a critical optical depth τ_{cl}^* above which Lyα photons are predominantly absorbed by dust rather than scattered. After N_{scat} scatterings in the wing, the probability for a photon to be absorbed before returning to the line core is $P_{\mathrm{abs}} \sim N_{\mathrm{scat}}(x)\epsilon\mathcal{H}(x) \sim x^2\epsilon\sqrt{\pi}x^2/a_\nu$. Setting $P_{\mathrm{abs}} \sim 1$ yields the absorption frequency $x_{\mathrm{abs}} \sim (a_\nu/\sqrt{\pi}\epsilon)^{1/4}$. If this frequency is smaller than the escape frequency x_{esc}, photons are absorbed before they can escape. Equating $x_{\mathrm{abs}} = x_{\mathrm{esc}}$ gives the critical optical depth:

$$\tau_{\mathrm{cl}}^* \sim \pi^{1/8} a_\nu^{-1/4} \epsilon^{-3/4} \sim 3 \times 10^6 \Big(\frac{T}{10^4\ \mathrm{K}}\Big)^{-1/4} \Big(\frac{D}{D_\odot}\Big)^{-3/4}. \tag{4.27}$$

Above this threshold, the force multiplier saturates because most Lyα photons are absorbed before contributing to the radiation force. The resulting expression for M_F in the dusty case is

$$M_F(\tau_{\mathrm{cl}}) = \min[M_F(\tau_{\mathrm{cl}}, D = 0), M_F^*(D)], \tag{4.28}$$

$$M_F^*(D) \simeq 40 \Big(\frac{T}{10^4\ \mathrm{K}}\Big)^{-1/4} \Big(\frac{D}{D_\odot}\Big)^{-3/4}. \tag{4.29}$$

Although we have so far expressed the effect of dust in terms of the dust-to-gas ratio D, it is often more practical to relate it directly to metallicity. The most common assumption in galaxy formation simulations is $D/D_\odot = Z/Z_\odot$ (Hopkins et al., 2023). However, observations in the local Universe indicate that the dust-to-gas ratio decreases more steeply at sub-solar metallicities (Rémy-Ruyer et al., 2014). High-redshift observations further suggest that, within $0.1 \lesssim Z/Z_\odot \lesssim 1$, dust abundances are comparable to or slightly lower than local values (Algera et al., 2025). Consequently, the linear scaling $D/D_\odot = Z/Z_\odot$ likely overestimates the true dust content, and thus the attenuation of Lyα radiation. To remain conservative, we adopt this upper-limit relation when computing the dust-suppressed force multiplier, replacing $D/D_\odot \to Z/Z_\odot$ in Eq. 4.29.

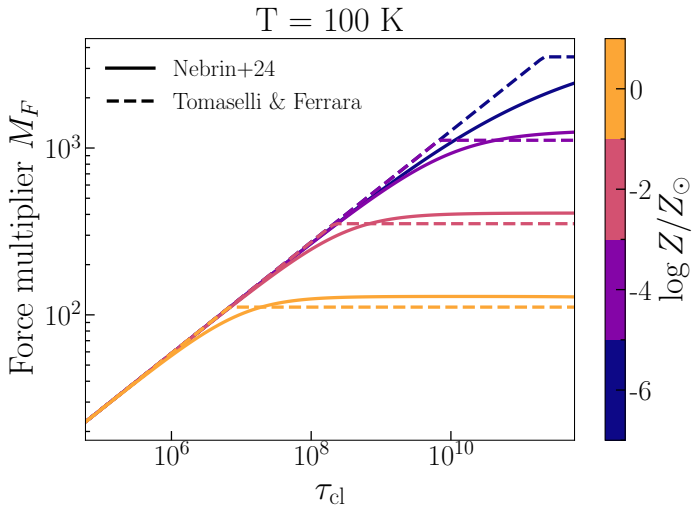

Figure 4.4: Force multiplier as a function of the cloud optical depth, from Nebrin et al. (2025) (solid) and Tomaselli & Ferrara (2021) (dashed). Different colours indicate metallicity values. Both approaches show the same saturation behaviour at high optical depth.

The relations above rely on simplified physical arguments rather than on a direct solution of the full Lyα transfer equation (Eq. 4.15). Nonetheless, they agree remarkably well with the exact steady-state solutions recently derived by Nebrin et al. (2025). Figure 4.4 compares the two approaches, showing M_F as a function of the cloud optical depth for $T = 100$ K and various metallicities. Both methods predict that M_F increases with $\tau_{\rm cl}$ and saturates once dust absorption becomes dominant.

As an example, for a typical high-redshift metallicity of $Z/Z_\odot \sim 10^{-2}$, feedback-free (FF) clouds with $\tau_{\rm cl} \sim 10^{10}$ lie well within the saturation regime. Neglecting Lyα photon destruction by dust would therefore lead to a significant overestimate of the true force multiplier.

4.3.2 When Lyα radiation pressure dominates?

The discussion so far indicates that Lyα radiation pressure becomes particularly important in dense and metal-poor environments. Under these conditions, resonant scattering enhances the coupling between radiation and gas, with significant implications for the maximum star formation efficiency (SFE) that molecular clouds can reach (see Sec. 1.6). To assess the true dynamical importance of Lyα feedback, it is necessary to compare it quantitatively with other feedback mechanisms operating in star-forming regions.

As discussed in Sec. 1.6, several feedback channels regulate star formation within giant molecular clouds (GMCs). Since we are mainly interested in systems with free-fall times $t_{\rm ff} \lesssim 3$ Myr, we focus on the *early* feedback processes acting before the onset of supernova explosions—namely, photoionisation, stellar winds, and radiation pressure.

To compare the strength of these mechanisms, we compute for each the momentum injection rate per unit stellar mass, i.e. the force from feedback per unit stellar mass, $\langle \dot{p}_*/m_* \rangle$. In a cloud with stellar mass M_* and initial gas mass M_c, the total feedback force is then

$$\dot{p}_* = \langle \dot{p}_*/m_* \rangle M_* = \langle \dot{p}_*/m_* \rangle \epsilon_* M_c, \tag{4.30}$$

where $\epsilon_* \equiv M_*/M_c$ denotes the overall star formation efficiency of the cloud.

Assuming spherical geometry, feedback drives an expanding shell of gas. Star formation halts once the outward force from feedback balances gravity, preventing further collapse:

$$\dot{p}_* = F_g \rightarrow \langle \dot{p}_*/m_* \rangle M_* = \frac{G M_{\rm gas}(M_* + M_{\rm gas}/2)}{R_c^2}, \tag{4.31}$$

where both stellar gravity and gas self-gravity are included. Introducing the gas surface density $\Sigma_g = M_c/\pi R_c^2$, we can solve for the equilibrium SFE:

$$\frac{\hat{\epsilon}_*}{1-\hat{\epsilon}_*^2} = \frac{\Sigma_g}{\Sigma_{\rm crit}}, \tag{4.32}$$

where the critical surface density is defined as

$$\Sigma_{\rm crit} \equiv \frac{1}{\pi G} \langle \dot{p}_*/m_* \rangle. \tag{4.33}$$

The parameter $\Sigma_{\rm crit}$ thus sets the maximum surface density at which feedback can still balance gravity and suppress further star formation. For $\Sigma_g \gtrsim \Sigma_{\rm crit}$, feedback becomes inefficient and $\hat{\epsilon}_* \to 1$. The derived $\hat{\epsilon}_*$ represents an upper limit, as star formation effectively ceases once $\hat{M}_* = \hat{\epsilon}_* M_c$ is reached.

With this framework, we can now evaluate $\langle \dot{p}_*/m_* \rangle$ and the corresponding $\Sigma_{\rm crit}$ for each feedback mechanism.

The pressure of ionised gas ($P_{\rm HII}$) acting on the expanding shell yields

$$\dot{p}_{\rm ion} \simeq 4\pi R_{\rm HII}^2 P_{\rm HII}, \tag{4.34}$$

where $R_{\rm HII}$ is the radius of the ionised region. The pressure in the H II region is $P_{\rm HII} \sim n_{\rm HII} k_{\rm B} T_{\rm HII}$, with $T_{\rm HII} \approx 10^4$ K. Assuming photoionisation equilibrium, the gas number density is $n_{\rm HII} = (3\dot{N}_{\rm ion}/4\pi\alpha_B R_{\rm HII})^{1/2}$. For a reference ionising photon rate $\dot{N}_{\rm ion} = 10^{46.88}(M_*/M_\odot)\,{\rm s}^{-1}$ corresponding to a Salpeter IMF (1–100 $M_\odot$), the momentum injection rate per stellar mass and critical density are (Nebrin, 2025)

$$\langle \dot{p}_{\rm HII}/m_* \rangle \sim 10^{-8} \Big(\frac{R_{\rm HII}}{1\,{\rm pc}}\Big)^{1/2} \Big(\frac{M_*}{10^5\,M_\odot}\Big)^{1/2} {\rm cm\,s^{-2}} \tag{4.35}$$

$$\Sigma_{\rm crit,HII} \sim 500 \Big(\frac{R_{\rm HII}}{1\,{\rm pc}}\Big)^{1/2} \Big(\frac{M_*}{10^5\,M_\odot}\Big)^{1/2} {\rm M_\odot\,pc^{-2}}. \tag{4.36}$$

Massive stars drive high-velocity winds with mass-loss rate $\dot{M}_{\rm w}$ and terminal velocity $v_{\rm w}$. The instantaneous momentum injection rate is

$$\dot{p}_{\rm w} = \dot{M}_{\rm w} v_{\rm w}, \tag{4.37}$$

with $v_{\rm w} \sim 3000\,{\rm km\,s^{-1}}$ (Deng et al., 2024). Integrating over the IMF gives a mean momentum injection per stellar mass of (Hopkins et al., 2023; Nebrin, 2025)

$$\langle \dot{p}_{\rm wind}/m_* \rangle \sim 3 \times 10^8 \Big(\frac{Z}{Z_\odot}\Big)\,{\rm cm\,s^{-1}}. \tag{4.38}$$

Stellar winds therefore become increasingly important at near-solar metallicities, where metal lines efficiently transfer radiation momentum to the wind. The corresponding critical surface density is (Nebrin, 2025)

$$\Sigma_{\rm crit,wind} \sim 1800 \Big(\frac{Z}{Z_\odot}\Big)\,{\rm M_\odot\,pc^{-2}}. \tag{4.39}$$

For continuum radiation, the maximum force on the cloud is L_*/c, with L_* the bolometric stellar luminosity. The resulting momentum injection rate per stellar mass is (Nebrin, 2025)

$$\langle \dot{p}_{\rm rad}/m_* \rangle = \frac{\Psi}{c} \sim 6 \times 10^{-8}\,{\rm cm\,s^{-2}}, \tag{4.40}$$

where $\Psi \sim 10^3\,{\rm L_\odot/M_\odot}$ is the light-to-mass ratio (Dekel et al., 2023; Hopkins et al., 2023). This value is comparable to the momentum injected by stellar winds at solar metallicity. The corresponding critical surface density is

$$\Sigma_{\rm crit,rad} \sim 3000\,{\rm M_\odot\,pc^{-2}}. \tag{4.41}$$

Finally, the contribution from Lyα photons can be expressed as

$$\langle \dot{p}_\alpha/m_* \rangle = M_F \frac{L_\alpha}{cM_*} \sim 10^{-6} \Big(\frac{M_F}{100}\Big)\,{\rm cm\,s^{-2}}, \tag{4.42}$$

with a corresponding critical surface density

$$\Sigma_{{\rm crit},\alpha} \sim 3 \times 10^4 \Big(\frac{M_F}{100}\Big)\,{\rm M_\odot\,pc^{-2}}, \tag{4.43}$$

where M_F denotes the Lyα force multiplier.

From these estimates, it is evident that Lyα radiation pressure can dominate over other early feedback mechanisms, especially in metal-poor environments where dust absorption is minimal and M_F reaches large values. Even for the parameters typical of feedback-free (FF) clouds, Lyα feedback exceeds other early feedback channels by at least an order of magnitude. We therefore conclude that Lyα radiation pressure likely represents the principal feedback mechanism in the early Universe, and must be included in galaxy-formation simulations to capture realistic star formation regulation.

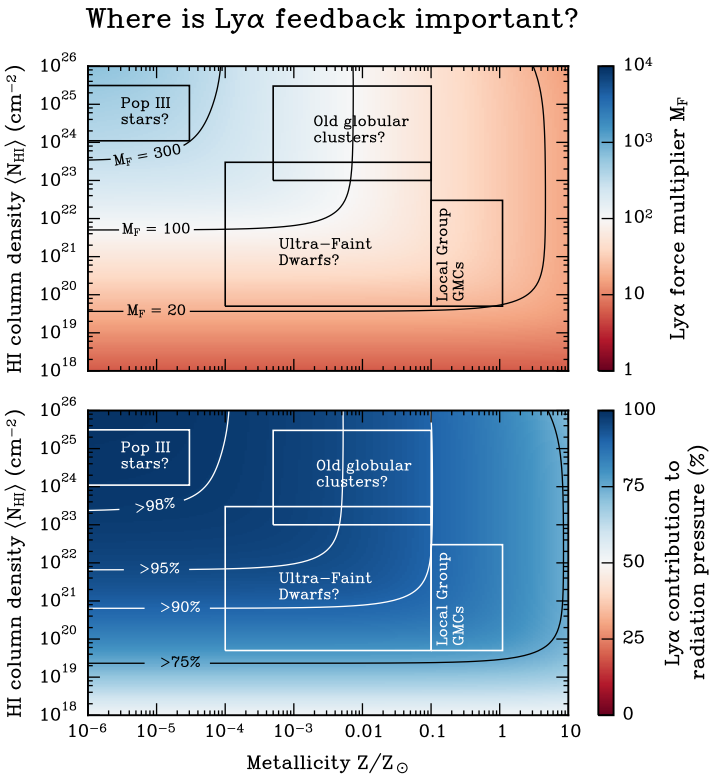

Figure 4.5: *Top:* Lyα force multiplier M_F as a function of gas column density and metallicity. *Bottom:* Fractional contribution of Lyα radiation pressure to the total available radiation pressure (L_*/c). From Nebrin et al. (2025).

A clear overview of the parameter space where Lyα feedback dominates is shown in Fig. 4.5, from Nebrin et al. (2025). The upper panel shows the force multiplier M_F as a function of gas column density and metallicity, computed under conservative assumptions (see Nebrin et al. 2025 for details). Notably, M_F can reach several hundred in the most metal-poor and dense environments where Population III stars are expected to form. Including Lyα feedback in Pop III models could therefore have profound consequences for their predicted properties—such as final masses, initial mass function, and clustering. The lower panel shows the fractional contribution of Lyα radiation pressure to the total radiation pressure (L_*/c), demonstrating that Lyα dominates across a wide range of column densities and metallicities, particularly in dense, low-Z regimes.

Armed with this framework and understanding of Lyα radiation pressure, we can now proceed to model its dynamical effects in detail and explore how resonant scattering influences the SFE of clouds in the early Universe.

Chapter 5

Lyα radiation pressure regulates star formation efficiency

5.1 Introduction

The James Webb Space Telescope (JWST) has opened exciting new avenues for understanding the galaxy formation process (Naidu et al., 2022; Roberts-Borsani et al., 2022; Castellano et al., 2023; Adams et al., 2023; Robertson et al., 2023, 2024). Among JWST's unexpected findings is a striking overabundance of bright ($M_{\rm UV} < -20$), very blue (UV slope $\beta \lesssim -2$) galaxies at redshift $z \gtrsim 10$ (Harikane et al., 2023; McLeod et al., 2024). The abundance of these "blue monsters" challenges our current understanding of galaxy formation (Mason et al., 2023; Mirocha & Furlanetto, 2023).

UV luminosity functions (LFs) derived from JWST observations can be reconciled with current galaxy formation models if early galaxies suffer minimal dust obscuration (Ferrara et al., 2023). This condition is achieved when the galaxy luminosity exceeds the Eddington limit, and radiation-driven outflows expel dust from the galaxy (Ziparo et al., 2023; Ferrara, 2024).

A straightforward alternative involves increasing the star formation rate (SFR) by requiring remarkably high star formation efficiencies (order-unity) in early galaxies (Dekel et al., 2023; Li et al., 2023). This condition could be met if star formation takes place in molecular clouds undergoing feedback-free bursts (FFBs) (Dekel et al., 2023). If the free-fall time of a star-forming cloud is shorter than the delay time of supernova explosions (≈ 1 Myr), star formation can proceed unimpeded during this phase, converting nearly all gas mass into stars. Analytical estimates and numerical simulations (Dekel et al., 2023; Menon et al., 2023) show that neither photoionisation feedback nor radiation pressure on dust appears to significantly limit SFE.

However, additional feedback could be provided by Lyman-α (Lyα) radiation pressure (Nebrin et al., 2025; Ferrara, 2024). Lyα is a resonant line, and multiple scatterings of Lyα photons with neutral hydrogen can impart significant momentum to the gas. The strength of Lyα feedback can be characterized by the force multiplier M_F, defined as $M_F \equiv \dot{p}_\alpha/(L_\alpha/c)$ (Dijkstra & Loeb, 2008), where $\dot{p}_\alpha$ represents the force from Lyα multiple scattering, and L_α/c is the force in the single-scattering limit. The force multiplier roughly scales as $M_F \propto \tau^{1/3}$ (Neufeld, 1990), where τ is the total Lyα optical depth at line centre, with additional dependencies on geometry, dust content and gas velocity (Nebrin et al., 2025; Smith et al., 2025).

For typical feedback-free (FF) clouds at redshift $z \gtrsim 10$, with optical depths $\log \tau_0 \gtrsim 10$ and metallicities $Z \gtrsim 0.02\, Z_\odot$ (Dekel et al., 2023), we expect $M_F \sim 100$ (Tomaselli & Ferrara, 2021; Nebrin et al., 2025). Analytical estimates further suggest that the force from Lyα photons is ~ 20 times stronger than the force from photoionisation and UV radiation pressure onto dust (Tomaselli & Ferrara, 2021).

The role of Lyα feedback has been investigated in various contexts. Using analytical estimates, Abe & Yajima (2018) derived the critical star formation efficiency, $\hat{\epsilon}_*$, above which Lyα feedback can evacuate the gas and suppress star formation. For typical FF clouds, their findings suggest $\hat{\epsilon_*} \sim 0.6$.

Kimm et al. (2018) used 3D RHD simulations of a metal-poor dwarf galaxy, including a subgrid model for Lyα momentum transfer, to study Lyα radiation pressure feedback. They found that Lyα radiation pressure regulates star-forming cloud dynamics before supernovae, reducing star formation efficiency and star cluster numbers by factors of two and five, respectively.

Recently, Nebrin et al. (2025) and Smith et al. (2025) derived analytical solutions of Lyα RT in the diffusion approximation for a uniform cloud, incorporating previously neglected physics such as velocity gradients, Lyα photon destruction, and recoil. The authors also provide convenient fits for the force multiplier, which could significantly improve existing subgrid models.

Ideally, to fully assess the impact of Lyα scattering on gas dynamics - and consequently on star formation - 3D RHD simulations with on-the-fly Lyα RT should be performed. However, the computational cost would be prohibitive with standard Monte Carlo radiative transfer (MCRT) methods. Instead, the resonant discrete diffusion Monte Carlo algorithm (rDDMC) offers a feasible solution (Smith et al., 2018), making 3D Lyα RHD simulations achievable in the near future. To date, the only Lyα RHD simulation has been carried out

in spherical symmetry by Smith et al. (2017), who investigated the dynamical impact of Lyα pressure on galactic winds, using both stars and black holes as sources. Their results confirmed that Lyα radiation pressure plays a crucial role in driving galactic winds and leaves observable imprints. In this Letter, we investigate the maximum SFE allowed by Lyα feedback using a shell expansion model. Lyα radiation pressure is accounted for adopting force multiplier fits provided in (Nebrin et al., 2025).

The Chapter is structured as follows. We first present the Methods in Sec.5.2 introducing the shell model, which we validate with 1D hydro simulations. In Sect. 5.3 we derive the SFE vs. cloud surface density for different gas metallicities, discussing also the role of extended sources. Sect. 5.4 provides a critical discussion and final conclusions.

5.2 Methods

5.2.1 Lyα-driven shells

Consider a uniform spherical giant molecular cloud (GMC) with mass M_c and density ρ. The virial parameter $\alpha_{\rm vir}$ is defined as

$$\alpha_{\rm vir} = \frac{5\sigma^2 R_c}{3GM_c}. \tag{5.1}$$

In virial equilibrium, $\alpha_{\rm vir} = 5/3$, and we can derive from Eq. 5.1 the expressions for the cloud radius $R_c = \sigma t_{\rm ff}$, free-fall time $t_{\rm ff} = (3/4\pi G\rho)^{1/2}$ and 1D velocity dispersion $\sigma = (GM_c/t_{\rm ff})^{1/3}$. The gas surface density is defined as $\Sigma_g = M_c/\pi R_c^2$.

Once a star cluster of mass M_* has formed at the centre of the cloud, massive stars producing H-ionising photons drive the formation and expansion of an H II region. Part of these photons are converted into Lyα photons by recombinations. Lyα radiation pressure sweeps neutral gas into a geometrically thin shell.

Shell models have already been applied to the study of GMC disruption by H II region expansion and radiation pressure (Krumholz & Matzner, 2009; Fall et al., 2010; Murray et al., 2010; Kim et al., 2016). Here we include Lyα radiation pressure, neglected in previous works. We then perform 1D hydro simulations in spherical symmetry to validate the shell model approach (see Sec.5.2.2 for the methods).

The time evolution of the shell radius, $R_s(t)$, is described by the momentum equation,

$$\frac{\rm d}{{\rm d}t}[M_s\dot{R}_s] = M_F(R_s)\frac{L_\alpha}{c} - \frac{GM_s(M_* + M_{\rm s}/2)}{R_{\rm s}^2}. \tag{5.2}$$

where $M_s = M(< R_s) = 4\pi(1-\epsilon_*)\rho R_s^3/3$ is the gas mass accumulated in the shell. The final outcome of the shell motion can be either cloud disruption or recollapse, depending on the balance of the forces on the right-hand side of Eq. 5.2. The second term is the gravity force, F_g, which includes the shell self-gravity. The first term is the Lyα force, F_α, which is the novel ingredient of our shell model. The strength of Lyα feedback is determined by the Lyα luminosity L_α and by the force multiplier M_F.

The Lyα luminosity is related to the ionisation rate $\dot{N}_\gamma$ by $L_\alpha = (2/3)E_\alpha\dot{N}_\gamma$, where $E_\alpha = 10.2$ eV is the energy of Lyα photons. For a burst of star formation the ionisation rate is $\dot{N}_\gamma = 10^{46.88}(M_*/M_\odot)\,{\rm s}^{-1}$, assuming a fixed[1] $Z/Z_\odot = 1/50$ (consistent with the value measured in early galaxies) and a 1-100 $M_\odot$ Salpeter IMF (Schaerer, 2003). The corresponding Lyα luminosity is $L_\alpha = 8.3\times10^{35}(M_*/M_\odot)\,{\rm erg\,s^{-1}} = l_\alpha(M_*/M_\odot)$, where we have defined the Lyα luminosity per unit stellar mass as l_α.

The force multiplier M_F depends on the Lyα optical depth at line centre τ and scales as $M_F \propto \tau^{1/3}$ in static, dust-free media. To account for Lyα destruction by dust, we adopt the fits to M_F provided in (Nebrin et al., 2025). The force multiplier in dusty media depends on the gas-to-dust ratio D. Here we follow the standard assumption from galaxy formation simulations, $D/D_{\rm MW} = Z/Z_\odot$ (Hopkins et al., 2023), where the Milky Way value is $D_{\rm MW}$=1/162.

The shell optical depth can be written as $\tau(R_s) = (1-\epsilon_*)\rho/m_p\sigma_\alpha R_s$, considering pure hydrogen gas. The Lyα cross section at line centre is $\sigma_\alpha = 5.88\times10^{-13}(T/100\,{\rm K})^{-1/2}$. With this setup, the only model free parameter is the SFE $\epsilon_* = M_*/M_c$. We determine its maximum possible value in Sect. 5.3.

For illustration, we plot the predicted evolution of the shell radius and velocity from the shell model in Fig. 5.1 by solid lines. Filled circles mark the disruption time when $R_s = R_c$. We present the results for $\Sigma_g = 10^4\,M_\odot\,{\rm pc^{-2}}$, $\log(Z/Z_\odot) = -2$ and $\epsilon_* =$ 1%, 5%, 10%, and 30%. Hydro simulation results are shown for comparison by dashed lines. For a detailed discussion of the hydro simulations, see Sec. 5.2.2.

The SFE controls both the disruption timescale and the terminal shell velocity. A larger SFE produces faster disruption and higher final velocities.

The shell solution agrees well with the hydro simulations. This consistency holds across the full range of metallicities, surface densities, and SFEs explored. Therefore, we can rely on Eq. 5.2 solutions to estimate the maximum SFE instead of running full hydro simulations.

[1]We ignore the metallicity dependence of $\dot{N}_\gamma$, as it introduces deviations smaller than $\lesssim 40\%$

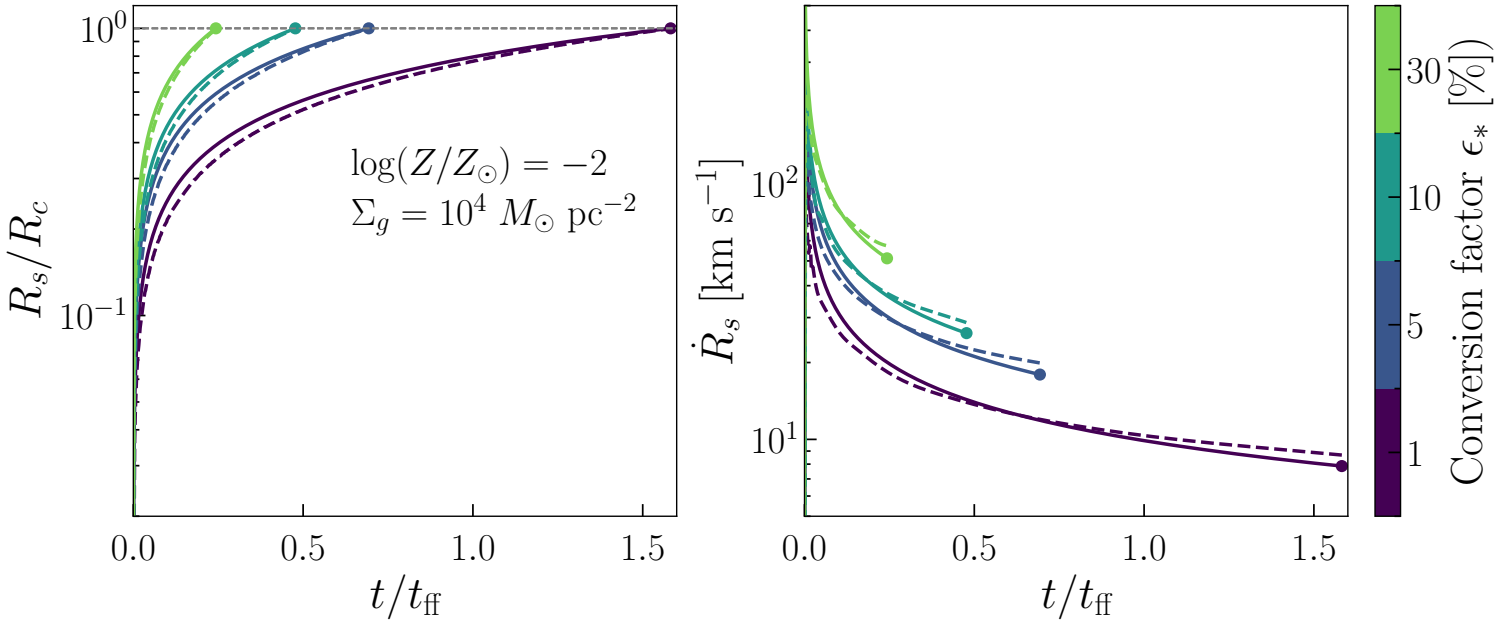

Figure 5.1: *Left panel:* Shell radius as a function of time normalized to the free-fall time for $\epsilon_* = 1\%$ (green), 5% (water green), 10% (blue) and 30% (purple). The clouds surface density and metallicity are $\Sigma_g = 10^4\,M_\odot\,\mathrm{pc}^{-2}$ and $\log(Z/Z_\odot) = -2$, respectively. Both the shell solution (Eq. 5.2, solid line) and the hydro-simulation predictions (dashed) are shown. *Right:* Same for the shell velocity.

5.2.2 Hydro model

To validate the shell model, we perform 1D spherically symmetric hydrodynamical simulations adopting a finite-volume formulation. We use a fixed uniform grid with 1000 cells with boundaries $(0.01, 1) \times R_c$. We apply free boundary conditions and compute the intercell fluxes with an HLLC Riemann solver. We enforce density and pressure floors to avoid complete gas depletion from the cells. As initial condition, we adopt a uniform cloud in pressure equilibrium with an ambient gas of density $\rho_{\rm amb} = 10^{-3}\rho$. The gas is almost isothermal (polytropic index $\gamma \approx 1$) at $T = 30$ K.

The fluid's state vector $\mathbf{Q}_i = (m_i, p_i, E_i)$ encoding the mass, momentum and energy of each cell i is evolved according to

$$\frac{\mathrm{d}\mathbf{Q}_i}{\mathrm{d}t} = -\int_{\partial V_i} \mathbf{F}(\mathbf{U}) d\mathbf{n} + \mathbf{S}_i, \tag{5.3}$$

$$\mathbf{F}(\mathbf{U}) = \begin{pmatrix} \rho \\ \rho v \\ (\rho e + P)v \end{pmatrix}, \quad \mathbf{S}_i = \begin{pmatrix} 0 \\ F_g + F_\alpha \\ v(F_g + F_\alpha) \end{pmatrix}. \tag{5.4}$$

The gravity force in each cell with centre of mass R_i is $F_g = GM(< R_i)m_i/R_i^2$. To compute the Lyα force we first compute the Lyα optical depth at cell boundaries, $\tau_{i\pm1/2} = \tau(R_{i\pm1/2})$. The net Ly$\alpha$ force on the cell is then given by:

$$F_\alpha = [M_F(\tau_{i+1/2}) - M_F(\tau_{i-1/2})]\frac{L_\alpha}{c}. \tag{5.5}$$

Here we note that the force multipliers in Nebrin et al. (2025) were derived under the assumption of a uniform cloud. However, as soon as the shell forms, this approximation breaks down and in spherical symmetry an arbitrary density profile is not equivalent to a homogeneous representation in optical depth space. Nevertheless, adopting Eq. 5.5 is consistent within a factor of $\lesssim 2$ (Lao & Smith, 2020).

As an illustration we discuss the hydro model with $\Sigma_g = 10^4\,M_\odot\,\mathrm{pc}^{-2}$, $\log(Z/Z_\odot) = -2$, and $\epsilon_* = 30\%$. Fig. 5.2 shows the number density and velocity profiles for different snapshots, with time in units of the free-fall time indicated by the colorbar. A thin shell forms and increases its density as it expands. We identify the shell as the densest cell at each time.

The lower panel of Fig.5.2 shows the shell velocity over time (dashed black line). The velocity peak is slightly offset with the shell position, coinciding with low density gas just behind it. As a result the curve does not coincide with the velocity peaks. This suggests that a fraction of Lyα photons originates from fast-moving ionized gas just behind the shell. These photons are Doppler-shifted out of resonance with the slowly moving neutral gas beyond the shell and with the gas in the shell moving in the opposite direction. However, as discussed in Sect. 5.4, only velocities of order $v \sim 500\,(N_{\rm HI}/10^{20}\ \mathrm{cm}^{-2})^{1/2}\ \mathrm{km\,s}^{-1}$ can substantially suppress the

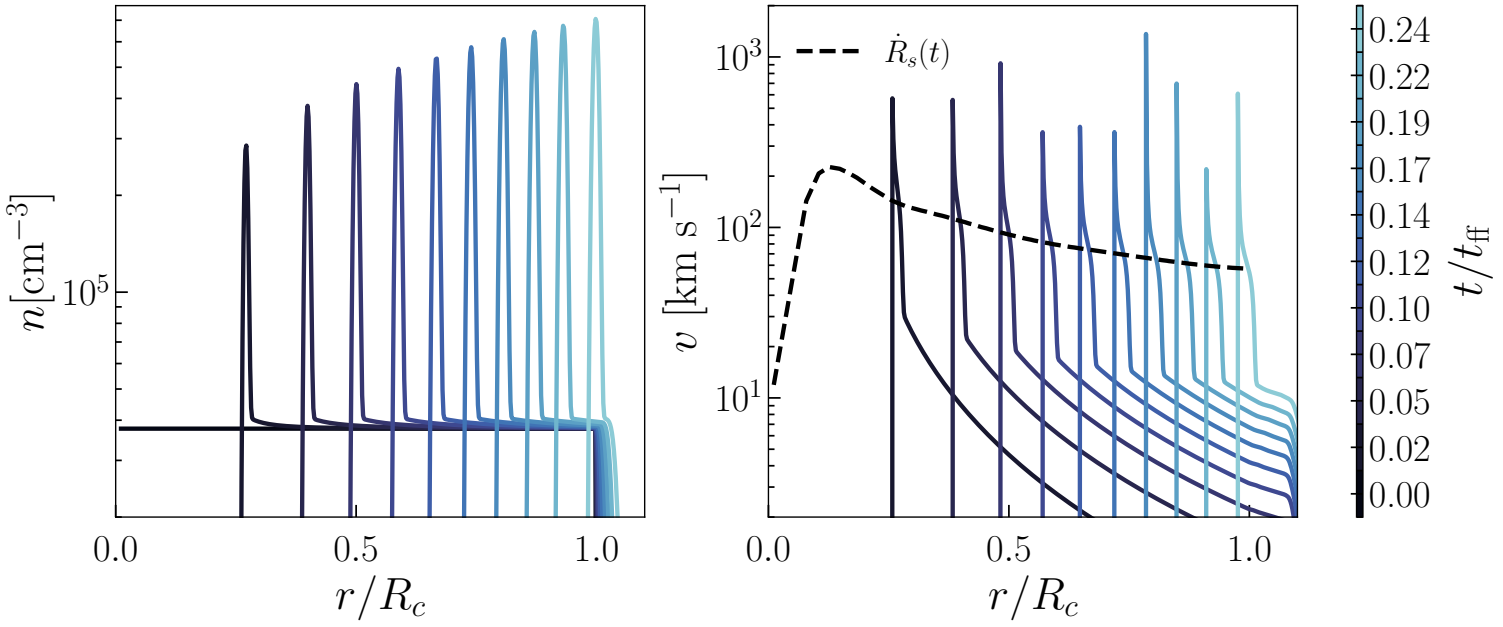

Figure 5.2: *Upper panel:* Number density profiles for different snapshots of the simulation. Time in free-fall time units is colour-coded. The surface density of the cloud is $\Sigma_g = 10^4\ M_\odot\ \mathrm{pc}^{-2}$, with metallicity $\log(Z/Z_\odot) = -2$ and SFE $\epsilon_* = 30\%$. *Lower:* Same for the velocity profiles. The black dashed line shows the time evolution of the shell velocity, corresponding to the velocity of the cell with highest density.

force multiplier. This behaviour was derived by Tomaselli & Ferrara (2021) for Doppler-shifted Lyα photons interacting with static gas. The velocity shifts in our models are too weak to affect Lyα radiation pressure, especially in the densest clouds.

The shell accelerates quickly at early times and then slows down due to mass accumulation and gravity. With this parameter set the cloud is disrupted on a short timescale, $t_d = t(R_s = R_c) = 0.24\ t_{\mathrm{ff}}$.

5.3 Results

5.3.1 Maximum SFE efficiency allowed by Lyα feedback

The simplest approach would be to deduce the SFE by requiring that Lyα and gravitational forces balance when the shell reaches the cloud radius. Setting the left-hand side of Eq. 5.2 to zero (i.e. $F_{\mathrm{tot}} = F_\alpha - F_g = 0$), and further imposing $R_s = R_c$, we find (see also Kim et al., 2016; Abe & Yajima, 2018; Nebrin et al., 2025):

$$\frac{\hat{\epsilon}_*}{1-\hat{\epsilon}_*^2} = \frac{\Sigma_g}{\Sigma_{\mathrm{crit}}}, \tag{5.6}$$

where the critical surface density is given by

$$\Sigma_{\mathrm{crit}} = \frac{M_F l_\alpha}{\pi G c M_\odot} = 316 M_F(\Sigma_g, Z)\ M_\odot\ \mathrm{pc}^{-2}. \tag{5.7}$$

This solution is straightforward, however it provides no timescale information. Moreover, if the cloud takes longer than a free-fall time to be disrupted, additional star formation could occur. This would lead to an underestimate of the final SFE.

To proceed, we solve Eq. 5.2 numerically. To derive the maximum SFE $\hat{\epsilon}_*$, a cloud disruption criterion must be specified. We first compute the shell evolution for a given SFE, up to the final time $t_d = t(R_s = R_c)$. We then check if one of the two conditions is satisfied: (a) $F_{\mathrm{tot}} = 0$, or (b) $\dot{R}_s = v_{\mathrm{esc}} = [(1+\epsilon_*)GM_c/R_c]^{1/2}$. If neither of the two conditions are satisfied, we iterate adjusting ϵ_*.

Condition (a) requires that when Lyα pressure balances gravity, the collapse of the gas halts and star formation ceases. In contrast, the stricter requirement $\dot{R}_s = v_{\mathrm{esc}}$ in condition (b) ensures that cloud is totally dispersed preventing any future collapse. This condition demands stronger feedback, since gravity can already be balanced by Lyα radiation pressure even when the shell velocity remains below v_{esc}. Consequently, the values of $\hat{\epsilon}_*$ from condition (b) are always larger than those from condition (a).

Fig. 5.3 shows the resulting maximum SFE for both cases as a function of surface density, for metallicities $\log(Z/Z_\odot) = -6, -4, -2, 0$. If condition (a) is applied the SFE reduces to Eq. 5.6, once the dependence of the critical surface density on gas

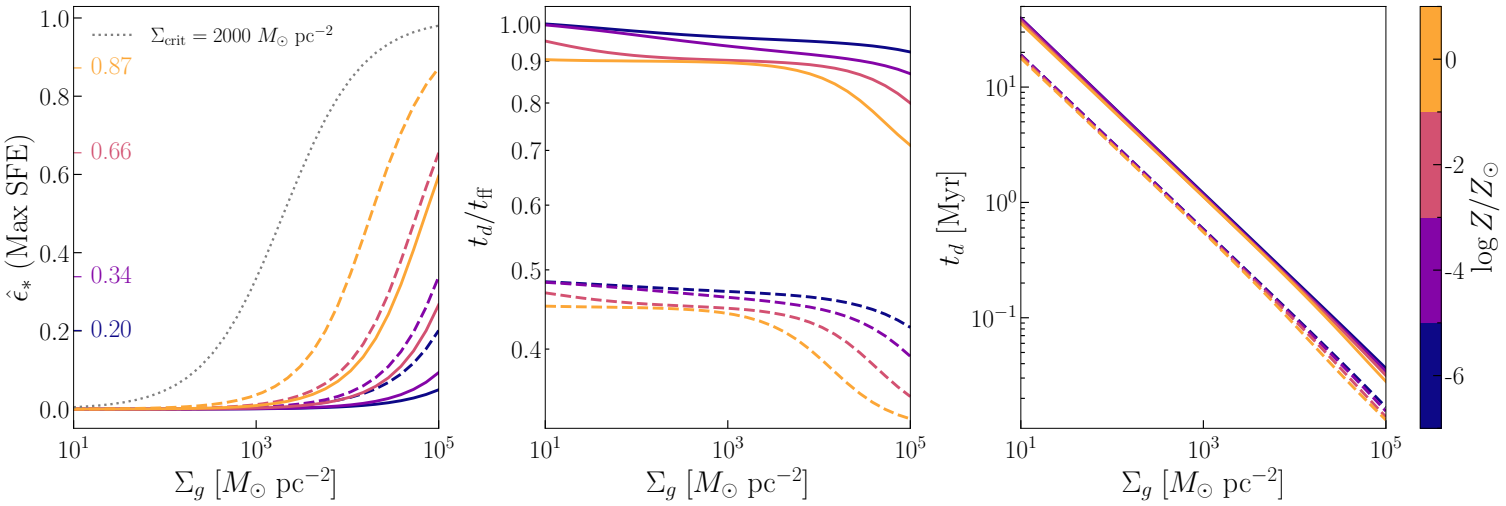

Figure 5.3: *Left panel:* Maximum SFE as a function of surface density for metallicity $\log(Z/Z_\odot) = -6$ (blue), -4 (purple), -2 (red), 0 (orange). Solid or dashed curves show where the zero-force ($F_{\rm tot} = 0$) or the escape velocity ($\dot{R}_s = v_{\rm esc}$) conditions are satisfied. The dotted curve show the time-independent solution (Eq. 5.6) for the reference value $\Sigma_{\rm crit} = 2000\,M_\odot\ {\rm pc}^{-2}$ used by Somerville et al. (2025). Coloured ticks mark the maximum SFE across the surface density range for each metallicity. *Middle:* Cloud disruption time in units of the free-fall time as a function of the cloud surface density for various metallicities as indicated in the colorbar. Solid or dashed curves show where the zero-force ($F_{\rm tot} = 0$) or the escape velocity ($\dot{R}_s = v_{\rm esc}$) conditions are satisfied. *Right:* As the middle panel, with t_d in units of Myr.

surface density and metallicity is included. For comparison, we also show the maximum SFE obtained from Eq. 5.6, for a fixed $\Sigma_{\rm crit} = 2000\,M_\odot\ {\rm pc}^{-2}$ (see e.g. Somerville et al. 2025). For reference, we find $\Sigma_{\rm crit} = 1.4 - 1.7 \times 10^5\,M_\odot\ {\rm pc}^{-2}$ for $\log(Z/Z_\odot) = -2$ across our gas surface density range. The final time, t_d – when the shell radius reaches R_c – is shown in units of the cloud free-fall time and in Myr in the central and right panels of Fig. 5.3.

Lyα strongly limits the SFE, even for the densest clouds. At $\log(Z/Z_\odot) = -2$, typical of high-redshift galaxy metallicities, the SFE is $0.01 \lesssim \hat{\epsilon}_* \lesssim 0.66$ for $10^3 \lesssim \Sigma_g[M_\odot\ {\rm pc}^{-2}] \lesssim 10^5$. For very metal-poor GMCs, $\log(Z/Z_\odot) \leq -4$, the SFE is always $\hat{\epsilon}_* \lesssim 0.34$. Near-unity SFEs are possible only for extreme surface densities, $\Sigma_g = 10^5\ M_\odot\ {\rm pc}^{-2}$, and near-solar metallicities. We have quoted here the less restrictive values from condition (b).

We note that the cloud disruption timescale is always $t_d \lesssim t_{\rm ff}$, independent of density. 3D RHD simulations of GMCs that include stellar wind and radiative (UV, optical and IR) feedback show that the stellar mass is assembled over $\sim 3 - 4\,t_{\rm ff}$ (Hopkins et al., 2023; Menon et al., 2023). In these simulations, the star formation rate declines after reaching its peak, and in our model the central cluster has already formed. Given the suppressed star formation rate and the short timescale, almost no additional stellar mass forms as the shell expands. Hence, the derived $\hat{\epsilon}_*$ values represent a reliable upper limit.

5.3.2 Impact of extended sources

The spatial extent of the Lyα source can limit feedback, particularly in dusty media (Nebrin et al., 2025). 3D RHD simulations of GMCs show that UV radiation pressure can be reduced by flux cancellation (Menon et al., 2023).

We now examine how source extension affects the force multiplier and, consequently, the maximum star formation efficiency (SFE). For a uniform, static cloud of total optical depth τ, the force multiplier is

$$M_F(\tau) = N(a_\nu \tau)^{1/3},$$

where $a_\nu = 4.7 \times 10^{-3}(T/100\ {\rm K})^{-1/2}$ is the Voigt parameter. The constant N encodes the effect of source geometry: for a point source $N = 3.51$, while for a source uniformly distributed throughout the cloud it decreases by a factor of ~ 7 to $N = 0.51$ due to flux cancellation. Additional suppression arises from Lyα photon destruction by dust, which is more significant for extended sources. These effects are included in the fitting relations of Nebrin et al. (2025), to which we refer for further details.

In our shell model, we can account for both point-like and extended components of the source. For a uniform source of radius R_*, stars located within the shell act as point sources, contributing a luminosity

$$L_\alpha^{\rm point} = \begin{cases} L_\alpha (R_s/R_c)^3, & R_s < R_*, \\ L_\alpha, & R_s \geq R_*, \end{cases} \tag{5.8}$$

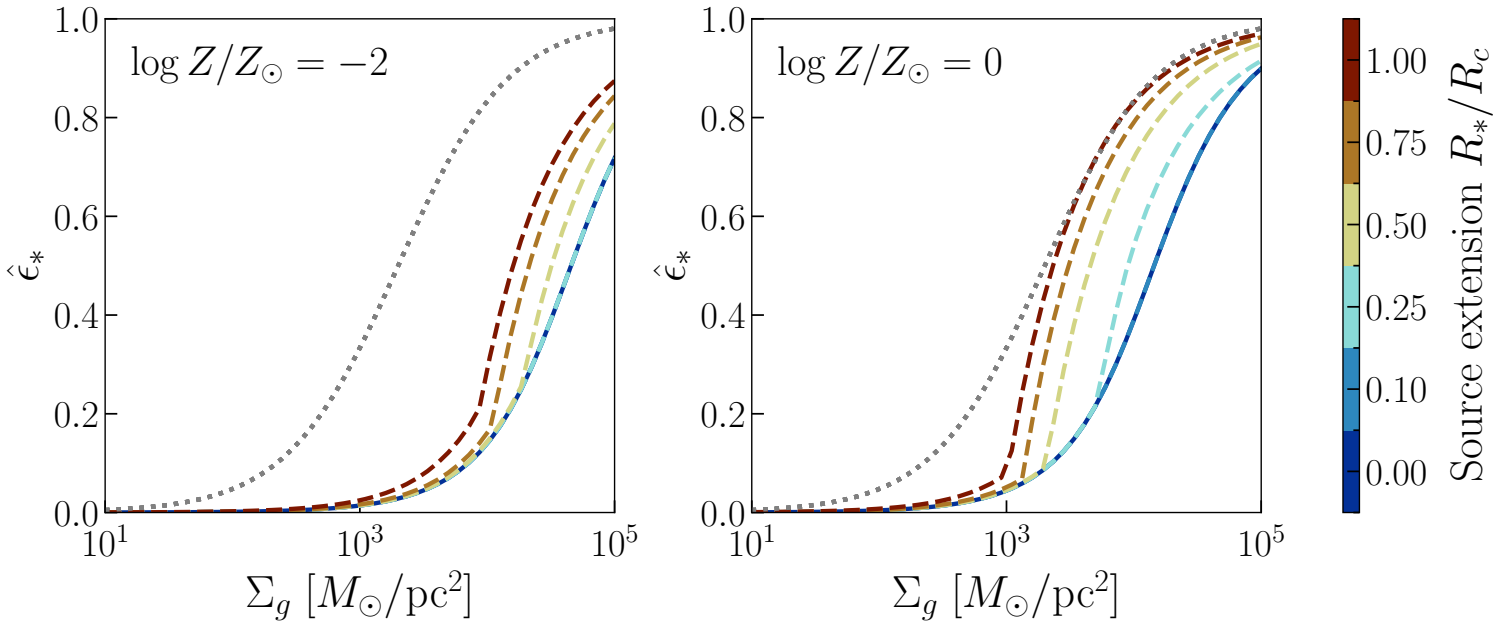

Figure 5.4: Maximum SFE as a function of cloud surface density for different source extensions: $R_* = 0.1$ (cyan), 0.25 (light blue), 0.5 (yellow), 0.75 (orange), and 1 (red), shown with dashed lines. The point-source case is shown in solid blue. For reference, the SFE corresponding to $\Sigma_{\rm crit} = 2000\,{\rm M}_\odot\,{\rm pc}^{-2}$ is indicated by a gray dotted line.

while the remaining luminosity is uniformly distributed,

$$L_\alpha^{\rm uni} = L_\alpha - L_\alpha^{\rm point}.$$

The total Lyα force on the shell is then

$$F_\alpha = M_F^{\rm point}\frac{L_\alpha^{\rm point}}{c} + M_F^{\rm uni}\frac{L_\alpha^{\rm uni}}{c}. \tag{5.9}$$

We evaluate the resulting maximum SFE for source extensions $R_*/R_c = 0, 0.1, 0.25, 0.5, 0.75$, and 1 (Fig. 5.4). The results are shown only for $\log(Z/Z_\odot) = -2$ and 0, as the influence of source extension increases with metallicity. The escape-velocity condition is adopted and the results are similar for the zero-force case. For $\log(Z/Z_\odot) = -2$, the SFE remains identical to the point-source case for $R_*/R_c \leq 0.25$, with noticeable enhancement only for $R_* \gtrsim 0.5$. At solar metallicity, the effect becomes significant for $R_* \gtrsim 0.1$, reflecting stronger attenuation of the force multiplier through combined flux cancellation and Lyα destruction by dust.

5.4 Discussion and summary

Key to our results is the value of the force multiplier M_F. In our model, we neglected some physical effects that could limit Lyα feedback, such as velocity gradients, the Lyα source extension and turbulence.

All the gas in the shell has the same velocity, and therefore we should deal with a bulk velocity. Significant suppression of the force multiplier is expected only at velocities $v \sim 500\,{\rm km/s}\,(N_{\rm HI}/10^{20}{\rm cm}^2)^{1/2}$ (Tomaselli & Ferrara, 2021) for clouds with H I column density $N_{\rm HI}$. Within our parameter range, $21 \lesssim \log N_{\rm HI} \lesssim 25$, strong suppression of the force multiplier is expected at velocities around $1500\ {\rm km\,s^{-1}}$ for the least dense clouds. However, since the simulated shell velocities remain within 0–$1000\ {\rm km\,s^{-1}}$, the velocity dependence of the force multiplier can be neglected, particularly for the massive clouds that are the main focus of this study.

In turbulent media, Lyα photons escape more easily through low-density channels. Fluctuating velocity gradients introduce large Doppler shifts, which further aid photon escape. Nebrin et al. (2025) showed that the suppression of M_F scales as $M^{-8/9}$, where $M = \sigma/c_s$ is the Mach number. For $M = 10$ and $\log(Z/Z_\odot) = -2$, the force multiplier is suppressed by a factor of ~ 3, yielding $\Sigma_{\rm crit} = 4.9 - 6.7 \times 10^4\,M_\odot\,{\rm pc}^{-2}$. The qualitative behaviour of the SFE is unchanged: order-unity SFE occurs only at $\Sigma_g \gtrsim \Sigma_{\rm crit}$.

We found that Lyα feedback disrupts clouds on short timescales, $t_d \lesssim t_{\rm ff}$. For $\Sigma_g \gtrsim 10^3\ M_\odot\ {\rm pc}^{-2}$, the free-fall time is < 1 Myr. This is comparable or even shorter than the delay to the first supernova explosions. Thus, Lyα radiation pressure acts as an efficient pre-supernova feedback channel and prevents a feedback-free phase.

Our model assumes that a stellar cluster of mass $M_* = \epsilon_* M_c$ forms at the cloud centre. In reality, Lyα radiation pressure operates as soon as the first massive stars form. Lyα -driven shells create low-density ionized bubbles around individual stars. Their

expansion and overlap suppress further star formation and reduce the star formation rate until the final SFE is reached. A more detailed investigation of this process is presented in Chap. 6.

We note that in our model the shell is driven solely by Lyα radiation pressure. In reality, several additional feedback channels operate. The swept-up gas in the shell is neutral, and lies outside the Strömgren radius R_s. The H II region thus provides a kick-start to the shell expansion. Photoionisation and radiation pressure on dust also contribute. The latter is dominated by the more numerous non-ionising photons and becomes more important as Z increases. Finally, stellar winds from massive stars, neglected here, inject yet further energy.

Therefore, our results represent generous upper limits to the actual SFE, since they neglect both the impact of early Lyα feedback on star formation and the contribution of other feedback channels.

We have combined a shell model and radiation hydrodynamic simulations to study Lyα radiation pressure feedback in GMCs. We derived the momentum equation for a shell including gravity and Lyα force. We validated the solution with 1D hydro simulations in spherical symmetry, finding good agreement. From these models we deduced the upper limit on SFE set by Lyα feedback, requiring a total vanishing force or shell velocity equal to the cloud escape velocity at the cloud boundary.

We found that Lyα radiation pressure can strongly limit the SFE achievable in molecular clouds. Once a central star cluster forms, the Lyα-driven shell reaches the cloud boundary in $\lesssim t_{\rm ff}$, at any surface density. This is shorter than the delay to the first supernova explosions for $\Sigma_g \gtrsim 10^3\,M_\odot\,{\rm pc}^{-2}$. Thus, Ly$\alpha$ radiation pressure prevents a feedback-free phase of star formation.

At $\log(Z/Z_\odot) = -2$, relevant for high-redshift galaxies, the SFE is $0.01 \lesssim \hat{\epsilon}_* \lesssim 0.66$ for $10^3 \lesssim \Sigma_g[M_\odot\,{\rm pc}^{-2}] \lesssim 10^5$. For very metal-poor GMCs, $\log(Z/Z_\odot) \leq -4$, the SFE is always $\hat{\epsilon}_* \lesssim 0.34$. Near-unity SFEs are possible only for extreme surface densities, $\Sigma_g = 10^5\,M_\odot\,{\rm pc}^{-2}$, and near-solar metallicities.

Our results are likely to overestimate the SFE, since they neglect both the impact of early Lyα feedback on star formation and the contribution of other feedback channels.

Chapter 6

Is feedback free star formation possible?

6.1 Introduction

The hydrogen Lyman-α (Lyα) line is often the most prominent emission feature (Osterbrock & Ferland, 2006) in the spectra of galaxies and has historically been used as a key tracer of star-forming systems (Partridge & Peebles, 1967; Djorgovski & Thompson, 1992; Rhoads et al., 2000; Taniguchi et al., 2005; Ouchi et al., 2009; Hu et al., 2010; Pentericci et al., 2011; Kashikawa et al., 2011; Ouchi et al., 2018; Shibuya et al., 2018). Surveys such as HETDEX (Hill & HETDEX Consortium, 2016), VLT/MUSE (Herenz et al., 2019), and SILVERRUSH (Ouchi et al., 2018; Shibuya et al., 2018, 2019) have also revealed a significant population of Lyα emitters across a wide redshift range.

In comparison, much less attention has been paid to the *dynamical* role of Lyα photons. As Lyα often carries a significant fraction of the bolometric luminosity in young, metal-poor galaxies, it has long been suspected that its radiation pressure could significantly impact gas dynamics (Cox, 1985; Bithell, 1990).

This physical effect might play a pivotal role in our understanding of the earliest galaxies now routinely investigated by the *James Webb Space Telescope* (JWST). One of the major JWST findings so far has been the discovery of a population of surprisingly bright, blue galaxies at $z \gtrsim 10$ (Naidu et al., 2022; Harikane et al., 2023; McLeod et al., 2024; Robertson et al., 2024). These sources, often termed "blue monsters," exhibit ultraviolet luminosities and colors that challenge existing models of early galaxy formation (Mason et al., 2023; Mirocha & Furlanetto, 2023).

To reconcile observations with theory, several mechanisms have been proposed: extremely low dust attenuation (Ferrara et al., 2023), top-heavy (or even PopIII-dominated Maiolino et al. 2024b) initial mass functions (Trinca et al., 2024; Schaerer et al., 2024), or modified cosmological initial conditions (Liu & Bromm, 2022; Padmanabhan & Loeb, 2023).

A particularly straightforward explanation suggests that such galaxies formed stars with extremely high efficiency, potentially converting nearly all their gas mass into stars during short-lived, 'feedback-free' bursts (FFB, Dekel et al., 2023; Li et al., 2023). In this scenario, if the free-fall time of a star-forming molecular cloud is shorter than the delay before the first supernovae (typically ~ 3–5 Myr), star formation proceeds essentially unregulated, yielding star formation efficiencies (SFEs) approaching unity. Analytical arguments and radiation-hydrodynamic (RHD) simulations have claimed that early feedback processes—such as photoionization heating and UV radiation pressure on dust—are insufficient to halt star formation under these conditions (Li et al., 2023; Menon et al., 2023).

However, the FFB scenario neglects the momentum imparted by resonantly trapped Lyα photons, which can become dynamically dominant well before the first SNe. At the extremely high neutral hydrogen column densities expected in compact, metal-poor systems, Lyα photons undergo $\gg 10^6$ scatterings, with the resulting radiation pressure capable of disrupting gas clouds and quenching further star formation (Tomaselli & Ferrara, 2021; Kimm et al., 2018; Nebrin et al., 2025). Crucially, this occurs on timescales shorter than the SN delay time, contradicting the key assumption of the FFB model.

As Lyα often carries a significant fraction of the bolometric luminosity in young, metal-poor galaxies, it has long been suspected that its radiation pressure could impact gas dynamics (Adams, 1972; Harrington, 1973; Neufeld, 1990; Tan & McKee, 2003; Oh & Haiman, 2002). Early analytic and numerical studies suggested that trapped Lyα photons could slow accretion onto protostars and dark matter halos, while Monte Carlo radiative transfer simulations showed that the momentum transfer from multiple scatterings can drive supersonic outflows (Dijkstra & Loeb, 2008; Dijkstra & Loeb, 2009).

The dynamical influence ot Lyα photons is often characterized by the *force multiplier* $M_F \equiv \dot{p}_\alpha/(L_\alpha/c)$, which quantifies how photon trapping boosts the radiation force. In static, dust-free media, this multiplier scales as $M_F \propto \tau_0^{1/3}$, where τ_0 is the Lyα line-center optical depth (Adams, 1972; Smith et al., 2017; Kimm et al., 2018). For typical star-forming clouds at high redshift, the optical depths are enormous ($\log \tau_0 \gtrsim 10$), leading to $M_F \sim 100$ or higher (Tomaselli & Ferrara, 2021; Nebrin et al., 2025), even in the presence of a moderate dust content (Tomaselli & Ferrara, 2021).

The first hydrodynamical simulations explicitly incorporating Lyα momentum coupling found that it can significantly alter the

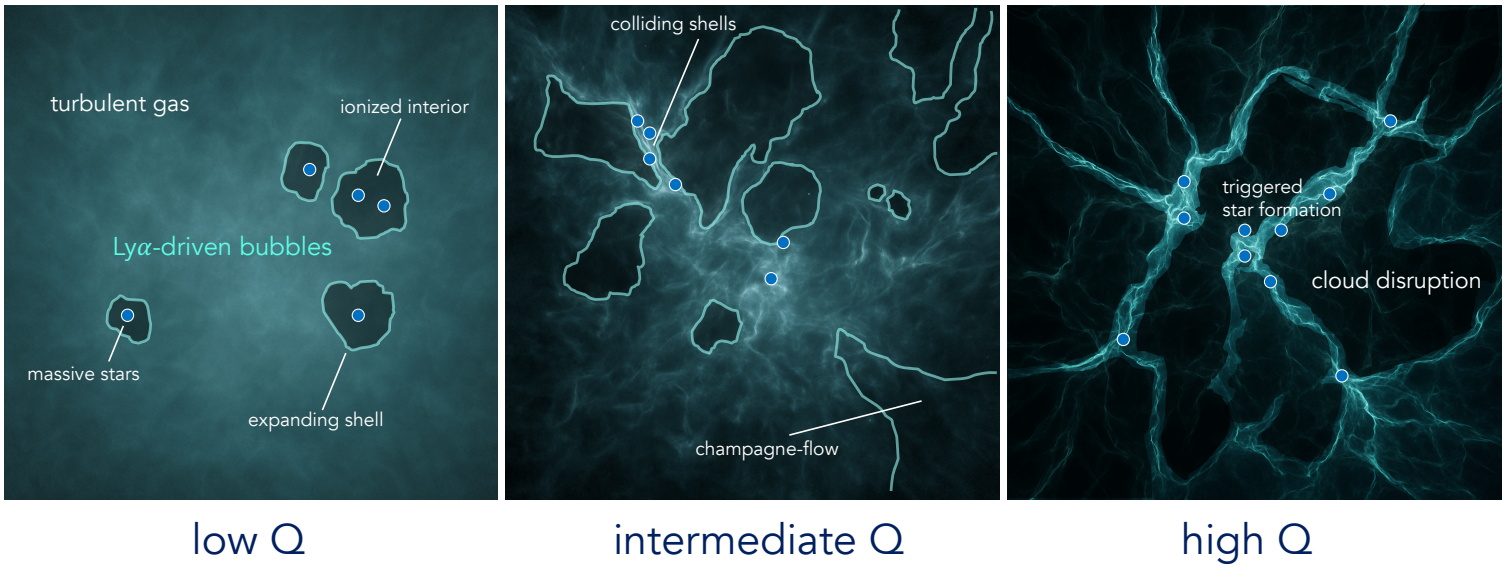

Figure 6.1: Illustrative sketch of the Lyα-driven bubble evolution in a star forming GMC. Ionized bubbles surrounded by neutral shells form around massive stars and expand due to Lyα radiation pressure. While in the bubble interior star formation is suppressed, shells could become gravitationally unstable, fragment and form stars. As the volume filling factor $Q(t)$ increases, star formation is also facilitated by shell collisions in which the gas is highly compressed. Such triggered star formation accelerates the growth of bubbles until the remaining gas is either completely ionized or evacuated from the potential well of the GMC.

dynamics of early star-forming clouds. Smith et al. (2016, 2017, 2018, 2019) showed that Lyα pressure can drive gas shell expansion faster than ionizing radiation alone, while Kimm et al. (2018) implemented a subgrid model calibrated via MCRT simulations using the RASCAS code (Michel-Dansac et al., 2020), accounting for recoil, dust, and deuterium effects. Their results suggested that Lyα feedback can potentially reduce star formation efficiency (SFE) and regulate cloud evolution prior to supernova (SN) explosions. Notably, M_F saturates at high τ_0 due to dust absorption, with values ranging from ~ 50 for solar metallicity to $\gtrsim 100$ in primordial environments.

Recent works have begun to highlight the regulatory role of Lyα feedback. Using RHD simulations with subgrid Lyα momentum coupling calibrated via Monte Carlo radiative transfer, Kimm et al. (2018) showed that Lyα pressure can reduce SFE and star cluster formation by factors of a few. Analytic models further indicate that Lyα pressure alone can exceed the combined force from photoionization and UV continuum pressure by an order of magnitude (Abe & Yajima, 2018; Tomaselli & Ferrara, 2021; Nebrin et al., 2025). Notably, this regulation occurs well before the onset of SN explosions, fundamentally challenging the notion of a feedback-free star formation phase.

In this Thesis, we argue that Lyα radiation pressure is the dominant early feedback mechanism that regulates SFE in star-forming clouds. We study the evolution and overlap of bubbles whose expansion is driven by Lyα radiation pressure. This feedback is capable of halting star formation and reducing the cloud's ability to convert gas into stars. Our model combines analytic estimates of Lyα trapping and momentum coupling with a detailed treatment of cloud evolution under Lyα-driven feedback.

The Chapter is organized as follows. In Sec. 6.2 we compute the Lyα-driven shell evolution and overlap. In Sec. 6.3 we use the model to determine the SFE of star-forming clouds when Lyα feedback is included. Sec. 6.4 discusses additional effects due to dust destruction of Lyα photons, the presence of HII regions and other Lyα radiative transfer aspects. Sec. 6.4.4 summarizes the chapter.

6.2 Methods

6.2.1 Lyα-driven bubbles

Take a star-forming giant molecular cloud (GMC) of a given gas mass, M_c, and number density, $n = \rho/\mu m_p$, where $\mu = 1.22$ is the mean molecular weight for an atomic neutral H+He mixture, and m_p is the proton mass. Assuming the GMC to be in virial equilibrium, we define the virial parameter as

$$\alpha_{\rm vir} = \frac{5}{3}\frac{\sigma^2 R_c}{fGM_c} \tag{6.1}$$

where f is a geometrical factor related to the cloud internal density profile. For spherical clouds with a radial density profile $\rho \propto r^{-\gamma}$, it is $f = (1-\gamma/3)/(1-2\gamma/5)$. We assume $f = 1$ for our homogeneous cloud and $\alpha_{\rm vir} = 5/3$, which is consistent with local

observations (Heyer et al., 2009) and simulations of GMCs (Grisdale et al., 2018). From eq. 6.1 we derive the expression for the cloud radius $R_c = \sigma t_{\rm ff}$, free-fall time $t_{\rm ff} = (3/4\pi G\rho)^{-1/2}$, and 1D velocity dispersion $\sigma = (GM_c/t_{\rm ff})^{1/3}$. Finally, for some purposes the following expression for the gas surface density, $\Sigma_g = M_c/\pi R_c^2$, is useful:

$$\Sigma_g = 800 \left(\frac{M_c}{10^6\ M_\odot}\right)^{1/3} \left(\frac{n}{10^3\ {\rm cm}^{-3}}\right)^{2/3}\ M_\odot\ {\rm pc}^{-2} \tag{6.2}$$

If one writes the mean star formation rate in the cloud using the standard Schmidt-type law, then using the previous expressions we find

$$\dot{\rm SFR}_0 = \epsilon_{\rm ff}\frac{M_c}{t_{\rm ff}} = \epsilon_{\rm ff}\frac{\sigma^3}{G}. \tag{6.3}$$

In the following we take the 'instantaneous' efficiency per free-fall time as $\epsilon_{\rm ff} = 0.01$ based on the average value of local measurements obtained by Krumholz & Tan (2007).

As soon as they form, massive stars (mass m_*), produce H-ionizing photons at a rate $\dot{N}_\gamma$. Part of these photons are converted by recombinations into Lyα photons exerting a radiation pressure onto the surrounding gas. As a result, the gas is compressed in an expanding thin shell enclosing a low-density bubble, whose radius, R_s, increases with time according to the solution of the momentum equation,

$$\frac{d}{dt}[M(<R_s)\dot{R}_s] = M_F(R_s)\frac{L_\alpha}{c} \tag{6.4}$$

Interestingly, this mechanism works even in metal-free gas as it does not rely on the presence of dust grains (or free electrons, in the standard Eddington case) to transfer the radiation momentum to the gas. In eq. 6.4 we have neglected the gravity force, $F_g = Gm_*M_s/R_s$ exerted by the star on the shell, which can be shown to be negligible before shells start to overlap. If individual bubbles are small with respect to the cloud radius $R_s \ll R_c$, the tidal effects of the global cloud gravity field can also be neglected.

The Lyα luminosity[1], $L_\alpha = (2/3)E_a\dot{N}_\gamma$, where $E_\alpha = 10.2$ eV is the energy gap of the transition, drives the radiation pressure. The ionization rate depends on stellar mass and metallicity. We adopt a metallicity[2] consistent with that measured in early galaxies ($\approx 1/50\ Z_\odot$) and use the results in Schaerer (2002):

$$\log \dot{N}_\gamma = 27.80 + 30.68x - 14.80x^2 + 2.50x^3, \tag{6.5}$$

with $x = \log(m_*/M_\odot)$. For a $1 - 100\ M_\odot$ Salpeter IMF which we adopt here, the IMF-weighted mean ionizing luminosity of massive ($m_* > 8M_\odot$) stars is $\dot{N}_\gamma = 10^{48.7}\ {\rm s}^{-1}$ corresponding to a characteristic stellar mass $\hat{m}_* = 26.6\ M_\odot$. The previous value of $\dot{N}_\gamma$ implies $L_\alpha = 1.3 \times 10^4 L_\odot = 5 \times 10^{37}\ {\rm erg\ s}^{-1}$. Note that L_α would be even larger for a top-heavy IMF.

The force is amplified by the resonant nature of the Lyα scattering, resulting in the aforementioned force multiplier, M_F. Physically, M_F represents the ratio of the trapping time (due to multiple scatterings) of Lyα photons to the light crossing time in a system of characteristic size ℓ: $M_F = t_{\rm trap}/(\ell/c)$. In the absence of dust (see below), the force multiplier can be written, following **?** (see also Lao & Smith 2020), as

$$M_F \approx 3.51\ (a_v\tau_0)^{1/3}, \tag{6.6}$$

where $\tau_0 = \sigma_0 N_{\rm HI}$ is the optical depth at the line center, $\sigma_0 = 5.88 \times 10^{-14} T_4^{-1/2} {\rm cm}^2$, $T = 30$ K is the adopted gas temperature[3], and $N_{\rm HI}$ is the neutral hydrogen column density collected by the shell, on which radiation pressure acts; finally, $a_v = 4.7 \times 10^{-4} T_4^{-1/2}$. Here, we set $N_{\rm HI} = nR_s$. We note that eq. 6.6 is valid for a central point source, which should be appropriate in the context of this study.

If dust is present, radiation pressure is limited by the fact that Lyα photons are absorbed by grains, thus decreasing the force multiplier M_F. To account for this effect we use the derivation by Tomaselli & Ferrara (2021), and cap M_F above a certain τ_0 where dust absorption becomes important. This is equivalent to imposing the following condition:

$$M_F = \min[M_F, M_F(D)] \tag{6.7}$$

where M_F is given by eq. 6.6, and

$$M_F(D) = 35.2\ (T_4 D)^{-1/4}, \tag{6.8}$$

and D is the dust-to-gas ratio normalized to the Milky Way value (1/162), which we take to be proportional to the metallicity, $D \propto Z$. Expression eq. 6.7 is also in excellent agreement with the M_F predictions obtained by Nebrin et al. (2025) (see their Fig. 5) from a novel

[1] A negligible LyC escape fraction from the GMC is assumed.

[2] We note that $\dot{N}_\gamma$ is only weakly dependent on metallicity, varying by a factor $\lesssim 2$ in $0.01 < Z/Z_\odot < 1$.

[3] We use the notation $Y_X = Y/10^X$.

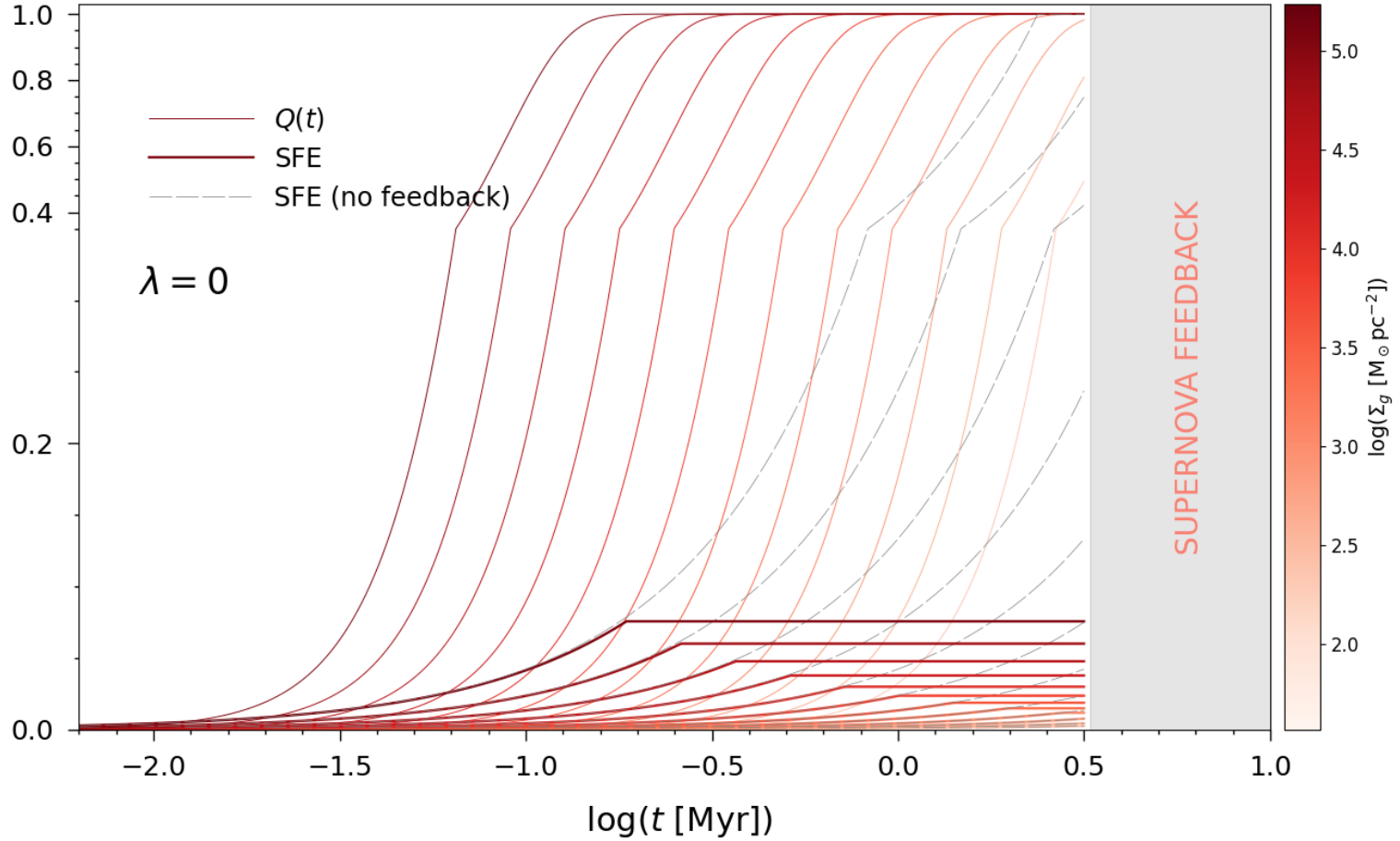

Figure 6.2: Time evolution of Lyα-driven bubbles volume filling factor Q (thin red lines) and star formation efficiency (SFE), $\epsilon_* = M_*/M_c$ (thick red curves) up to the onset of SN explosions at $t = 3$ Myr for a constant star formation rate ($\lambda = 0$, see Sec. 6.3.1). The curves are color-coded according to the cloud gas surface density, Σ_g, as shown in the colorbar. Also shown (gray dashed lines) is the SFE expected for each cloud in the absence of Lyα feedback. Note that the vertical axis has been expanded for display purposes.

analytical Lyα radiative transfer solution that includes the effects of continuum absorption, gas velocity gradients, Lyα destruction, ISM turbulence and atomic recoil.

Let us introduce the non-dimensional variables $y = R_s/R_c$, $\dot{y} = \dot{R}_s/\sigma$, and $\tau = t/t_{\rm ff}$. We also write $M_F = 3.51\,(a_v\sigma_0 n R_c)^{1/3}x^{1/3} \equiv M_0 x^{1/3}$. Eq. 6.4 becomes:

$$\frac{d}{d\tau}[y^3\dot{y}] = \mathcal{K}_\alpha y^{1/3}, \tag{6.9}$$

where $\mathcal{K}_\alpha(n,\sigma) = M_0 G L_\alpha/\sigma^4 c$ is the non-dimensional radiation pressure force coefficient. The solution of eq. 6.9 shows that the shell radius increases as a power-law function of time:

$$y(\tau) = \left(\frac{121\mathcal{K}_\alpha}{78}\right)^{3/11}\tau^{6/11}. \tag{6.10}$$

The expansion described by eq. 6.10 continues until the stars explode as SNe at the end of their life. Using the fits provided in Raiteri et al. (1996), the lifetime of a $\hat{m}_* = 26.6\,M_\odot$ star at $Z = 1/50\,Z_\odot$ is $t_* = 6.6$ Myr. As the main goal of this paper is to study the pre-SN feedback phase and assess whether radiation pressure from massive stars can disperse the cloud and limit star formation, we concentrate in the following on evolutionary times $t \leq t_*$.

6.2.2 Bubble overlap

Armed with the solution for the growth of bubbles around individual stars, we now concentrate on their collective behaviour. The volume filling factor, $Q(t)$, i.e. the fraction of the GMC volume filled with bubbles, is determined by the following differential equation:

$$\frac{dQ}{dt} = \nu\,\mathrm{SFR}\,\frac{V_s(t)}{V_c}(1-Q). \tag{6.11}$$

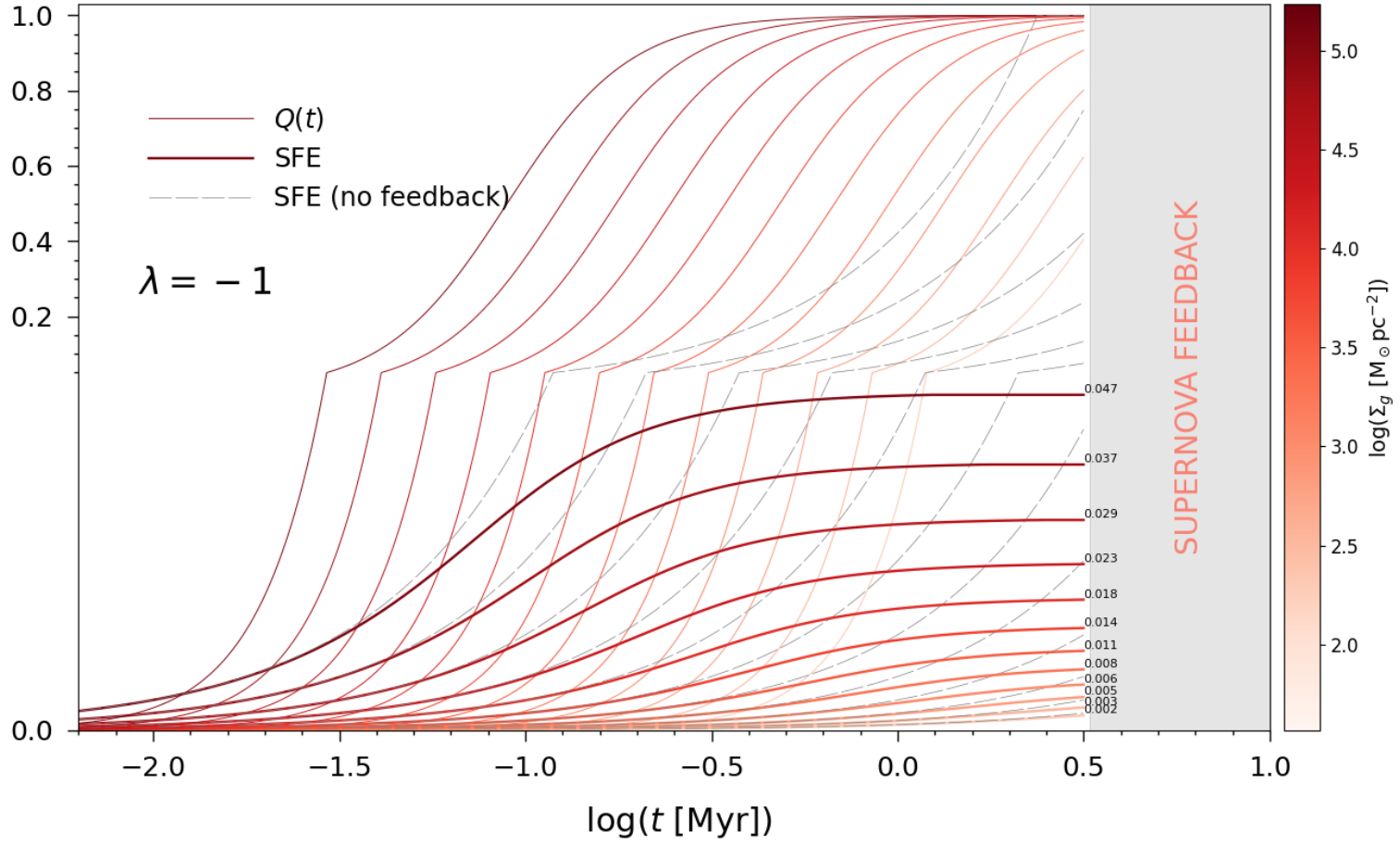

Figure 6.3: As Fig. 6.2 but including the negative feedback of Lyα-driven bubbles on the SFR ($\lambda = -1$, see Sec. 6.3.2). The numbers indicate the final value of the SFE, $\epsilon_* = M_*/M_c$, just before the onset of SN explosions at $t = 3$ Myr.

The $(1 - Q)$ term on the r.h.s. accounts for bubble overlapping, $V_s/V_c = (R_s/R_c)^3 = y^3$, and $\nu = 1/52.89$ is the number of massive ($> 8\ M_\odot$) stars per unit stellar mass formed appropriate for the adopted IMF. We first solve eq. 6.11 imposing a constant star formation rate SFR_0 (eq. 6.3); we then generalize the result to cases in which the SFR is itself a function of Q.

If we neglect overlapping, and we denote with $Q_0(t)$ the solution in this case, we find

$$Q_0(t) = \nu \frac{\mathrm{SFR}_0}{V_c} \int_0^t V_s(t - t')dt', \tag{6.12}$$

which in terms of normalized variables becomes

$$Q_0(\tau) = N_* \left[\frac{11}{29} \left(\frac{121 \mathcal{K}_\alpha}{78} \right)^{9/11} \tau^{29/11} \right], \tag{6.13}$$

where $N_* = (\nu\ \mathrm{SFR}_0\ t_{\mathrm{ff}})$ is the number of massive stars formed per free-fall time.

The previous formula is valid as long as the filling factor is low ($Q \lesssim 0.3$). For larger values, bubble overlapping becomes important, so the solution of eq. 6.11 takes the form

$$Q(\tau) = 1 - e^{-Q_0(\tau)}. \tag{6.14}$$

As the Lyα-driven bubbles expand, they carve low-density, ionized bubbles surrounded by dense shells. The probability that, at time τ, a given point in the GMC is located within a bubble, is given by $Q(\tau)$.

The above treatment assumes that the SFR is constant. This is equivalent to neglecting the feedback of bubbles on the star formation process. This feedback can be both negative or positive. Negative feedback occurs because the bubble interior contains low-density, ionized gas where star formation is virtually impossible. Hence, the overall SFR should be decreased by a factor $(1 - Q)$. On the other hand, gas collected in the expanding shells can become gravitationally unstable, fragment and form stars (see sketch in Fig. 6.1). This process represents a positive feedback on the SFR, whose strength increases with Q.

To describe this behaviour we write the SFR in the following generic form:

$$\mathrm{SFR} = \mathrm{SFR}_0(1 + \lambda Q), \tag{6.15}$$

where λ is an arbitrary constant. Note that $\lambda \geq -1$ in order to avoid an unphysical negative SFR for large Q. If $\lambda < 0$, negative feedback dominates, and as Q increases, star formation is suppressed. If instead $\lambda > 0$, the positive feedback produces a SFR increase. Finally, the special case in which negative and positive feedback exactly balance each other (or the presence of bubbles is ignored) corresponds to the case $\lambda = 0$ with a solution given by eq. 6.14. Physically-motivated values of λ will be discussed in the following Section.

To obtain the general solution for any value of $\lambda \geq -1$, we substitute eq. 6.15 into eq. 6.11 and solve for $Q(t)$:

$$Q(\tau) = \begin{cases} \dfrac{e^{(1+\lambda)Q_0(\tau)} - 1}{\lambda + e^{(1+\lambda)Q_0(\tau)}}, & \text{if } \lambda > -1, \\ \dfrac{Q_0(\tau)}{1 + Q_0(\tau)}, & \text{if } \lambda = -1. \end{cases} \tag{6.16}$$

Note that if $\lambda = 0$ we recover the constant SFR case described by eq. 6.14. In the following we will use this solution to discuss the fate of the GMC under the action of Lyα radiation pressure feedback.

6.3 Results

Using the formalism developed in the previous Sections, we want to determine the value of the gas-to-stars conversion factor, $\epsilon_* = M_*/M_c$, where M_* is the total mass of stars formed before SN explosions take place at $t = t_*$. We will derive this quantity as a function of the cloud properties. We explore two cases corresponding to either constant (eq. 6.3) or evolving (eq. 6.15) SFR.

6.3.1 Constant SFR

The constant SFR case is obtained by setting $\lambda = 0$ in eqs. 6.15–6.16, and therefore $\mathrm{SFR} = \mathrm{SFR}_0$. The key features for this case are illustrated in Fig. 6.2 for clouds with Σ_g in the range[4] $(37 - 1.7 \times 10^5)\ M_\odot\ \mathrm{pc}^{-2}$ bracketing the observed and predicted range for GMCs in different environments.

The filling factor Q grows with time for all clouds. As Q increases, a larger fraction of the GMC volume is filled with low-density, ionized gas in which SF is not possible. Eventually, SF stops when $Q \approx 1$. We define the time at which SF is quenched as t_Q. We note that this treatment is not completely self-consistent as the SFR should in principle decrease with time as the filling factor increases.

The condition $Q = 1$ is only reached by clouds with $\Sigma_g \gtrsim 100\ M_\odot\ \mathrm{pc}^{-2}$ before SNe start to explode at $t_{\mathrm{SN}} = 3$ Myr (roughly the lifetime of the most massive stars). Due to their higher SFR, the most massive clouds reach $Q = 1$ already at $t_Q \approx 0.2$ Myr.

Next, we compute the stellar mass formed, M_*, by time-integrating the SFR for each cloud; this mass is removed from the available gas mass. We then define the cloud star formation efficiency as $\epsilon_* = M_*/M_c$. The evolution of $\epsilon_*(t)$ is shown by the thick red curves in Fig. 6.2. As we see, feedback from Lyα radiation pressure limits the SFE to very low values ($\epsilon_* < 0.08$), ending SF well well before 3 Myr.

Although the constant SFR is a special (and unlikely) case in which positive and negative feedback exactly balance, it allows a direct comparison with the standard feedback-free star formation model, if we further remove the condition that SF is completely quenched once $Q = 1$. For comparison, we also show (gray dashed lines) the SFE expected for each cloud in the absence of Lyα feedback. Indeed, clouds with $\Sigma_g > 4 \times 10^4\ M_\odot\ \mathrm{pc}^{-2}$ can reach a SFE $\epsilon_* > 0.4$ before SNe occur. The most massive cloud, with its $\mathrm{SFR} = 0.43\ \mathrm{M_\odot yr^{-1}}$, is able to transform all its gas into stars in merely 2.4 Myr. This is in striking contrast with the results obtained when Lyα feedback is considered. Thus, if Lyα feedback is included, the potential feedback-free star formation mode yielding large SFE values is essentially erased. The SF suppression can be even more drastic during the pre-SN phase, as we are neglecting here the effects of HII regions. We'll return to this point in Sec. 6.4.2.

6.3.2 Evolving SFR (negative feedback only)

As we have noticed in Sec. 6.2, Lyα feedback can either quench or boost star formation depending on λ. We first discuss the negative feedback-only case, in which SFR is suppressed within bubbles. This case corresponds to $\lambda = -1$ and it is shown in Fig. 6.3.

The emerging picture is not fundamentally different from the constant SFR case analyzed above. Now the SFR decreases with time and this slows down the growth of $Q(t)$. While in principle the system has more time available to form stars before the cloud is dispersed at $Q = 1$, this advantage is counterbalanced by the slower conversion of gas into stars. As a result the final value of ϵ_* is roughly the same as in the constant SFR case.

[4] In practice, we fix $M_c = 10^6\ M_\odot$ and vary n to obtain the desired range.

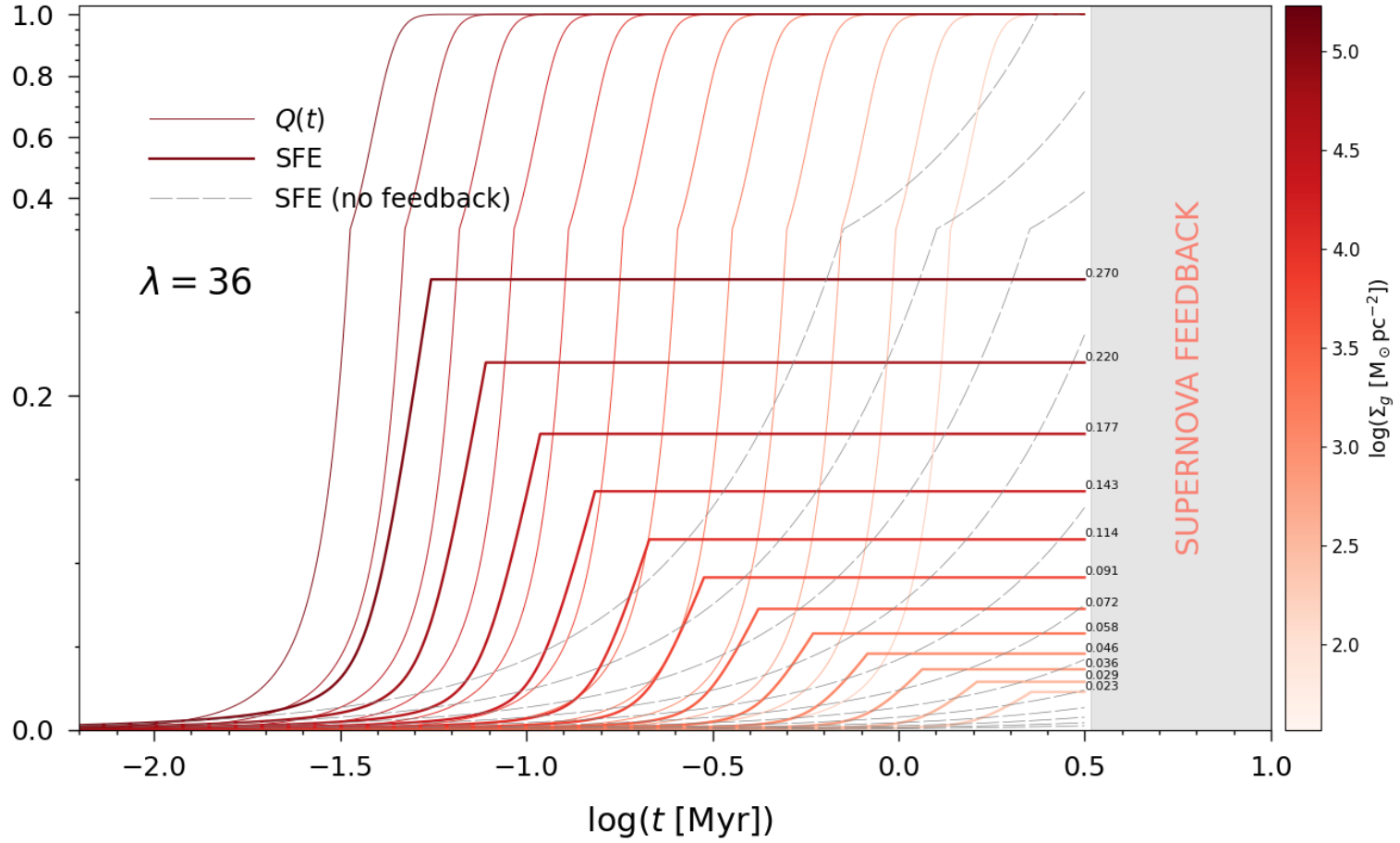

Figure 6.4: As Fig. 6.2 but including both negative and positive feedback of Lyα-driven bubbles on the SFR (we show results for the 'optimistic' case $\lambda = 36$, see Sec. 6.3.3). The numbers indicate the final value of the SFE, $\epsilon_* = M_*/M_c$, just before the onset of SN explosions at $t = 3$ Myr.

From Fig. 6.3 we see that the condition $Q = 1$ is now reached by the most massive clouds with $\Sigma_g \gtrsim 8000\ M_\odot\ \mathrm{pc}^{-2}$ before SNe start to explode. In these clouds the SFE is $\epsilon_* < 0.048$ (see the individual values shown in the Figure; also note that the y-axis scale has been expanded for a better display). Less massive clouds continue to form stars up to 3 Myr as their SFR is too low to produce a strong Lyα feedback; however, and for the same reason, their ability to convert gas into stars is very modest ($\lesssim 1\%$).

We conclude that – unless Lyα-driven bubbles produce some sort of positive feedback in addition to the negative one – there is no pre-SN feedback-free phase in which the SFE exceeds $5 - 10\%$.

6.3.3 Evolving SFR with triggered star formation

The treatment in Sec. 6.3.1 assumes that SFR is completely suppressed inside bubbles (negative feedback). While this remains a motivated assumption, it neglects the possibility that SFR can be instead enhanced (positive feedback) in swept-up shells and in the web of filaments produced by their collisions, a picture preliminary discussed in Sec. 6.2 (see sketch in Fig. 6.1). If positive feedback overcomes the negative one, the feedback parameter λ becomes positive too.

While radiation-hydrodynamical simulations including the dynamical treatment of Lyα radiation are necessary to fully characterize the importance of such triggered (or self-propagating) star formation process, some preliminary, educated guess of the λ value can nevertheless be made.

If the shells become gravitationally unstable, fragment and form stars, from eq. 6.3 we see that the SFR enhancement over the mean value SFR_0 is controlled by three processes: (a) the fraction of the shell mass that ends up into gravitationally-bound fragments, δM_s, (b) the density enhancement, δn, of the shell gas with respect to the mean, (c) the star formation efficiency per free-fall time enhancement, $\delta\epsilon_{\rm ff}$, with respect to the global value $\epsilon_{\rm ff}$. Thus, we can estimate λ from the relation

$$\lambda \simeq \delta M_s \times \delta\epsilon_{\rm ff} \times (\delta n)^{1/2}, \tag{6.17}$$

where the square-root dependence on δn comes from the free-fall time in eq. 6.3. Let us qualitatively evaluate these three factors.

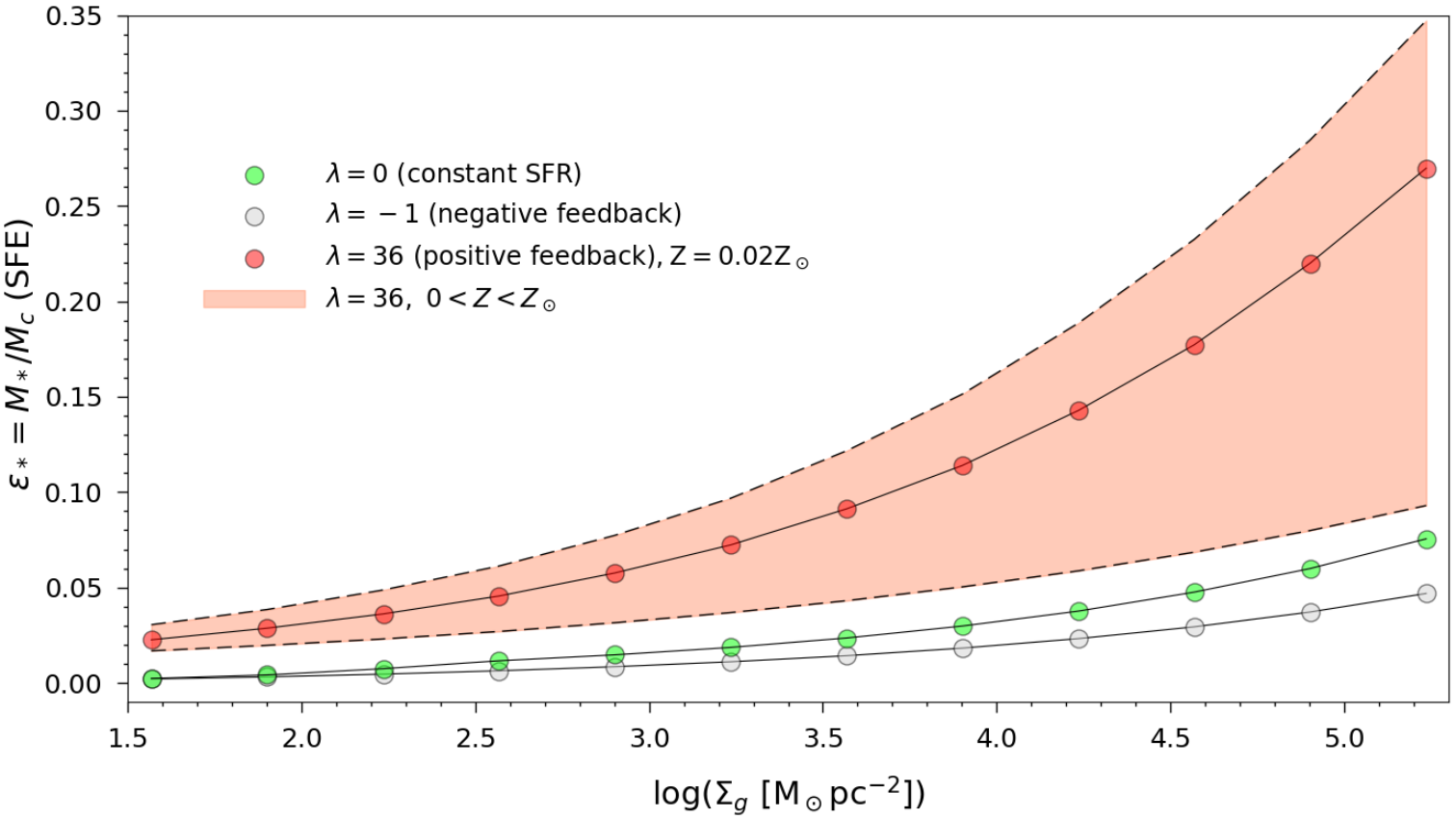

Figure 6.5: Summary plot showing the predicted dependence of the SFE of star-forming clouds on the cloud gas surface density, Σ_g, including the effects of Lyα feedback. We show the three cases corresponding to different values of the feedback parameter $\lambda = 0$ (green circles, constant SFR), $\lambda = -1$ (grey circles, including negative feedback only), $\lambda = 36$ (red circles, including negative and optimistic positive feedback). For the latter case we show the impact of varying the gas metallicity in the range $0 < Z < Z_\odot$ (coral shaded area) as discussed in Sec. 6.4.1.

Simulations of SN–driven and HII region–driven shells (Dale et al., 2009; Walch et al., 2013) typically find that, for thin shells, the fraction of mass ending up in bound clumps is $\delta M_s \approx 0.1$. For an isothermal strong shock, the post-shock density enhancement scales with the Mach number as $\delta n = \mathcal{M}^2$. In the case of Lyα-driven shells, the velocity evolves according to the derivative of eq. 6.10, $\dot{y} \propto \tau^{-5/11}$. At $t \approx 3$ Myr, depending on the initial gas surface density Σ_g, we find $\mathcal{M} \approx 1{-}15$. To maximize the star-formation enhancement, we adopt the upper value $\mathcal{M} = 15$, corresponding to $(\delta n)^{1/2} = 15$.

Clumps produced by shell fragmentation are expected to be dense and compact (Decataldo et al., 2019), allowing them to self-shield efficiently against UV radiation and resist gas ablation. Their star formation efficiency could therefore exceed that of the parent cloud (Lada et al., 2010; Krumholz et al., 2019). Murray (2011), by analyzing a sample of 32 star-forming GMCs in the Milky Way, found that while for the cloud-averaged value of $\epsilon_{\rm ff}$ is in the range is 0.002-0.2 (consistent with our choice $\epsilon_{\rm ff} = 0.01$), for individual clumps, $\epsilon_{\rm ff}$ raises to $0.14{-}0.24$. Adopting again the maximum value, we find $\delta\epsilon_{\rm ff} = 24$. Inserting these values into eq. 6.17 yields an optimistic estimate of $\lambda = 36$.

The results for $\lambda = 36$ are shown in Fig. 6.4. This choice corresponds to a scenario in which the SFR is overwhelmingly dominated (36:1) by triggered star formation resulting from Lyα-driven shell fragmentation. The final star formation efficiency prior to the onset of SN feedback increases with cloud surface density, rising from $\epsilon_* = 0.023$ at $\Sigma_g = 37\ M_\odot\ {\rm pc}^{-2}$ to $\epsilon_* = 0.27$ at $\Sigma_g = 1.7 \times 10^5\ M_\odot\ {\rm pc}^{-2}$. Given the optimistic assumptions adopted, these numbers should be regarded as upper limits. For comparison, the more conservative value $\lambda = 14$ yields $0.015 < \epsilon_* < 0.186$ over the same Σ_g range.

The relatively low final SFE is primarily driven by the rapid suppression of star formation caused by the swift expansion of Lyα-driven bubbles, which ionize and/or expel gas from the GMC, thereby removing it from the star formation cycle. Under such sustained SFR, the bubbles fill the entire GMC volume before the onset of SN explosions; in the most massive clouds, this occurs in $\lesssim 10^5$ yr.

We therefore conclude that Lyα radiation pressure imposes a stringent limit on the fraction of GMC gas that can be converted into stars during the feedback-free pre-SN phase.

6.4 Discussion and summary

The simple yet robust model we have developed shows that the SFE of molecular clouds in the pre-SN phase is regulated by an often ignored physical process, Lyα radiation pressure from young, massive stars. As low density, ionized bubbles grow and fill an increasingly large fraction, Q of the cloud volume, star formation is suppressed in such cavities, but could be triggered in the boundary shells which fragment into dense and opaque clumps.

Describing this process in detail is difficult, and dedicated, high-resolution RHD simulations in which Lyα dynamics is properly included are necessary. Although there a few early and promising attempts in this direction none of these studies can provide a definite answer yet due to the lack of one of the key ingredients. While pioneering studies (Dijkstra & Loeb, 2009), corroborated by the most recent and advanced analytical models (Tomaselli & Ferrara, 2021; Nebrin et al., 2025; Smith et al., 2025), have indisputably shown the importance of Lyα radiation pressure feedback in various environments, and most notably at high redshifts, numerical simulations are still falling short of providing quantitative and detailed predictions.

In fact, state-of-the-art multi-physics RHD galaxy simulations, such as e.g. SERRA (Pallottini et al., 2022) or FIRE (Hopkins et al., 2020), include various radiative feedback channels (photoionization, dust radiation pressure, etc.) but historically did not include, mostly due to their computational cost, on-the-fly Lyα radiation transfer and associated dynamical effects.

This gap is beginning to be filled by some studies (Smith et al., 2018; Kimm et al., 2018; Michel-Dansac et al., 2020). In particular, Smith et al. (2017) explored on-the-fly Lyα RHD in 1D/idealized setups and developed algorithms (rDDMC / resonant DDMC) to massively accelerate Lyα RT so that it can be coupled to hydrodynamics in 3D in the near future. Once fully implemented, these simulations will represent perfect follow-up experiments to test the present results, pin-point uncertain processes, and assess the role of triggered star formation.

The results found here are summarized in Fig. 6.5. There we show the relation between the final SFE ϵ_* at the end of the pre-SN phase (taken here to be 3 Myr) as a function of the cloud surface density Σ_g. We do confirm an increasing trend of the SFE ϵ_* in more massive clouds. This behaviour has been already suggested by previous authors (Li et al., 2023; Menon et al., 2025; Somerville et al., 2025) for HII regions- and SN-driven feedback. The SFE follows with good accuracy a power-law of the type $\epsilon_*(\Sigma_g, \lambda) = A(\lambda)\Sigma_g^{\gamma}$, with $\gamma \simeq 0.3$. Interestingly, the feedback does not modify the power-law index γ; rather, it controls the normalization factor A via the feedback parameter λ. For the three cases explored here we find $A(\lambda) = (1.2, 1.9, 7.2) \times 10^{-3}$ for $\lambda = (-1, 0, 36)$, respectively.

6.4.1 Dust effects

The results discussed so far have been obtained for a gas metallicity $Z = 0.02 Z_{\odot}$. In this context, metallicity controls two quantities: (a) the stellar ionizing photon production rate, $\dot{N}_{\gamma}$, and (b) the dust-to-gas ratio, D, which we assume to scale linearly with Z. Concerning (a) we have already noted (see footnote 2) that the the effect is negligible. The dust abundance is instead more critical and we discuss it in the following.

Dust, by absorbing Lyα photons, can decrease the value of M_F below the dust-free case (eqs. 6.6 and 6.8). Although the reduction depends weakly on D, it does affect the results. To illustrate this point we have rerun the positive feedback $\lambda = 36$, for a range of metallicities, spanning the range $0 < Z < Z_{\odot}$. The outcome is shown by the coral shaded area in Fig. 6.5. For solar metallicity (top boundary of the area) a reduced M_F value allows a 27% increase of the SFE from the fiducial case with $Z = 0.02 Z_{\odot}$. For a metal free gas though, the SFE is strongly suppressed, and it is about 3 times lower ($\epsilon_* = 0.09$).

Thus, Lyα radiation pressure effectively limits star formation even for solar metallicities. Surprisingly, though, many important works have neglected Lyα radiation pressure at solar metallicity, e.g. Arthur et al. (1996); Draine (2011). Moreover, we have to note that our study does not include direct radiation pressure on dust grains, which is mainly due to the much more numerous non-ionizing photons. Clearly, as Z increases, this pressure force becomes more important. Including this extra term is beyond the purpose of the present work; for reference, the relative importance of Lyα and dust-mediated radiation pressure on the gas has been discussed in detail in Tomaselli & Ferrara (2021). However, it is clear that dust, if present, might be another factor in erasing the alleged feedback-free star formation pre-SN phase by providing and extra radiation pressure channel. We stress again that advanced RHD simulations including dust dynamics are required to test our results under the idealized geometry adopted. For example, Nebrin et al. (2025) showed that dust destruction of Lyα photons can be stronger for extended sources.

6.4.2 HII regions

So far, we have neglected the effects of HII regions around massive stars. Qualitatively, we expect that over-pressurized, ionized regions also drive expanding bubbles in the GMC, similar to the Lyα-driven bubbles studied here. Therefore, neglecting HII regions likely leads to an *overestimate* of the SFE. As we have seen, $\epsilon_* \propto \Sigma_g^{0.3}$, meaning the most massive and dense clouds are those attaining a relatively high SFE (e.g., above 10%). From Fig. 6.5, taking the most favourable case $\lambda = 36$, this occurs for $\Sigma_g \gtrsim 10^4\ M_{\odot}\ \mathrm{pc}^{-2}$.

To illustrate the point, let us examine the most massive cloud in our range, with $\Sigma_g = 1.7 \times 10^5\ M_\odot\ \mathrm{pc}^{-2}$ and a corresponding density of $n = 3 \times 10^6\ \mathrm{cm}^{-3}$ (eq. 6.2). For the fiducial value $\log \dot{N}_\gamma = 48.6$, the Strömgren radius, which delimits the ionized region, is $R_I = 2.5 \times 10^{-3}$ pc. The ionization front (IF) reaches this radius in approximately a recombination time, $t_r = (\alpha_B n)^{-1} \approx 0.04$ yr. By that time, the size of the Lyα bubble (from eq. 6.10) would be $R_s = (1/16)R_I$. Thus, Lyα driving acts on the neutral layer just beyond R_s. In other words, the HII region provides a 'kick-start' to the Lyα-driven bubble.

Once the transition to a D-type IF occurs, the bubble begins to expand dynamically, driven by the internal pressure of the ionized gas. This expansion generates a shock in the surrounding neutral gas. Assuming an isothermal shock, and uniform, photoionization-equilibrium conditions in the ionized region, the velocity of the IF at radius R can be expressed as (Sommovigo et al., 2020):

$$\frac{1}{c_\mathrm{I}}\frac{dR}{dt} = \left(\frac{R_\mathrm{I}}{R}\right)^{3/4} - C\left(\frac{R}{R_\mathrm{I}}\right)^{3/4}, \tag{6.18}$$

where $C = (c_\mathrm{s}^2 + \sigma^2)/(c_\mathrm{I}^2 + \sigma^2)$, and c_I and c_s are the sound speeds in the ionized and neutral gas, respectively. With the boundary condition $r(t = 0) = R_\mathrm{I}$, eq. 6.18 can be integrated analytically. However, for our purposes, it suffices to determine the maximum (stalling) radius, $R_{I,\mathrm{max}}$, of the expanding HII region. Setting $dR/dt = 0$ yields:

$$R_{I,\mathrm{max}} \simeq R_I \left[1 + \left(\frac{c_I^2}{\sigma^2}\right)\right]^{2/3}. \tag{6.19}$$

The expansion stalls at $R_{I,\mathrm{max}}$ once the internal pressure is balanced by the external turbulent pressure, $\rho\sigma^2$. In eq. 6.19, we have also used the fact that $c_s \ll c_I$.

For our most massive molecular cloud, taking $c_I = 10\ \mathrm{km\,s}^{-1}$, we find $c_I/\sigma = (10/56.2) \simeq 0.18$. From eq. 6.19, this implies that $R_{I,\mathrm{max}}$ is only 2% larger than R_I – meaning the HII region barely expands beyond R_I.

We conclude that, in the absence of Lyα radiation pressure, HII regions would have a negligible impact on star formation and its efficiency of the most massive clouds, given their extremely low volume filling factor. The influence of HII regions becomes more significant for smaller clouds. However, this is largely irrelevant here, as such clouds already exhibit low ϵ_* values.

These preliminary conclusions must be verified through detailed numerical simulations that include the evolution of IFs and the combined effects of Lyα and dust-mediated radiation pressure. Nevertheless, our results provide robust upper limits on the SFE of star-forming clouds in the pre-SN phase.

6.4.3 Other neglected effects

We have not made any attempt to include the effects of velocity gradients, atomic recoil, or turbulent density fluctuations on the force multiplier, M_F. While the first two processes have been shown (Nebrin et al., 2025) to be largely subdominant[5] with respect to Lyα photon destruction due to dust (see Sec. 6.4.1), some authors (e.g. Munirov & Kaurov, 2023) have claimed that turbulent fluctuations with a finite correlation length, ℓ_t, could in principle reduce the average number of scatterings (and therefore M_F) suffered by Lyα photons before escaping the cloud. This effect becomes important when the correlation length is small, i.e. when the ratio $\ell_t/\lambda_\mathrm{mfp} \lesssim 10^4$, where $\lambda_\mathrm{mfp} = (n\sigma_0)^{-1}$ is the mean free path of a Lyα photon at the line centre. The above relation can be translated in a condition on $\ell_t < 0.05/n$ pc. As ℓ_t is measured to be $10 - 100$ pc in GMCs, for any density value considered here, turbulence should not have any significant effects on M_F. This conclusion is also supported by the results in Nebrin et al. (2025).

Finally, we recall that we have not included the energy input due to stellar winds from massive stars. Although the cumulative energy per unit stellar mass formed is only $\approx 1\%$ of that in ionizing radiation (see Fig. 2 of Pallottini et al. 2017), the more efficient winds energy coupling with the gas can partly compensate for the mismatch. Stellar winds could represent yet another, although maybe subdominant, SFE limiting factor during the first 3 Myr.

6.4.4 Summary

We have investigated whether Lyα radiation pressure from young, massive stars is effective in limiting the conversion of gas into stars (i.e. the star formation efficiency, SFE) in their parent molecular clouds prior to the onset of SN explosions (≈ 3 Myr from the beginning of star formation). The main goal of the study is to assess whether an early feedback-free evolutionary phase during which star formation occurs almost unimpeded by feedback processes and reach high SFE values.

[5] Using their analytical model solutions, Nebrin et al. (2025) have shown that for the point source geometry of interest here atomic recoil and velocity gradients do not appreciably modify the M_F trend in eq. 6.6. An additional effect, destruction of Lyα photons by $2p \rightarrow 2s$ transitions, might become important at high Σ_g thus mimicking dust effects in pristine environments.

To this aim we have developed a simple model describing the evolution and overlap of Lyα-driven bubbles, until star formation is quenched at a time t_Q corresponding to a bubble volume filling factor, $Q \simeq 1$, when the cloud gas is either fully ionized and/or evacuated. Our study examines a wide range of cloud gas surface densities, $\Sigma_g = 37 - 1.7 \times 10^5\ M_\odot\ \mathrm{pc}^{-2}$ bracketing the observed and predicted range for GMCs in different environments. The main results are:

- If Lyα bubbles do not feed back on the star formation rate ($\mathrm{SFR} \approx \mathrm{const.}$ or feedback parameter $\lambda = 0$ in eq. 6.16), Lyα radiation pressure limits the SFE to very low values ($\epsilon_* < 0.08$) independently of Σ_g, quenching the formation of new stars well before 3 Myr. This result is in stark contrast with the standard 'feedback free' model predictions, according to which clouds with $\Sigma_g > 4 \times 10^4\ M_\odot\ \mathrm{pc}^{-2}$ reach a SFE $\epsilon_* = 0.4 - 1.0$ before SNe occur.
- The impact of Lyα radiation pressure on the SFE is even more dramatic if we account for the decrease of the SFR within Lyα-driven bubbles ($\lambda = -1$, negative feedback). The condition $Q = 1$ is reached at $t < 3$ Myr by clouds with $\Sigma_g \gtrsim 8000\ M_\odot\ \mathrm{pc}^{-2}$; in these systems, $\epsilon_* < 0.048$. Less massive clouds continue to form stars up to 3 Myr as their SFR is too low to produce a strong Lyα feedback; however, and for the same reason, their SFE is very modest ($\lesssim 1\%$).
- Higher SFE values can only be attained if Lyα-driven shells fragment and form stars (triggered star formation) thus causing an increase in the SFR ($\lambda > 0$, positive feedback). While advanced RHD simulations are necessary to determine the value of λ, based on the physical arguments given, we argue that $\lambda \lesssim 36$. Adopting this value as an optimistic guess, we find that the SFE increases with cloud surface density, rising from $\epsilon_* = 0.023$ at $\Sigma_g = 37\ M_\odot\ \mathrm{pc}^{-2}$ to $\epsilon_* = 0.27$ at $\Sigma_g = 1.7 \times 10^5\ M_\odot\ \mathrm{pc}^{-2}$. Given the optimistic assumptions adopted, these numbers should be regarded as upper limits.
- We conclude that Lyα radiation pressure strongly limits the fraction of GMC gas that can be converted into stars, essentially erasing the possibility that a genuine feedback-free star formation mode with $\epsilon_* \gtrsim 0.4$ exists in the pre-SN phase.
- Our conclusion remains valid even when (i) the dust/metal content of the cloud is varied from metal-free to solar values, (ii) we allow for the presence of HII regions adding another negative feedback on the SFR, (iii) the effects of velocity gradients, atomic recoil, and turbulent density fluctuations on the Lyα force multiplier are considered.

Part III

Primordial Black Holes in the Early Universe

Chapter 7

PBHs as NIRB sources

7.1 Introduction

The Near Infrared Background (NIRB) is the diffuse radiation of cosmological origin observed after subtracting the local foregrounds in the band 1–10 μ m (Kashlinsky et al., 2018). Since early studies by Partridge & Peebles (1967), the NIRB has been considered a valuable tool to investigate the emission from the first stars and galaxy populations, as ultraviolet (UV) and optical light from high-z sources is redshifted to the near-infrared band.

Actual measurements of the mean NIRB intensity (Tsumura et al., 2013; Matsumoto et al., 2015; Sano et al., 2015; Matsuura et al., 2017) give a lower bound $I \gtrsim 10$ nW m^{-2}sr^{-1}, in excess with respect to the contribution of known galaxy populations derived from galaxy number counts (Driver et al., 2016). However, direct measurements of the NIRB suffer from large uncertainties due to the subtraction of foregrounds (Leinert et al., 1998), namely interplanetary dust emission (zodiacal light), galactic stars light and galactic interstellar medium radiation (cirrus).

Being foregrounds smooth, a more robust technique is computing the power spectrum of NIRB fluctuations (Kashlinsky et al., 1996; Kashlinsky & Odenwald, 2000), to which foregrounds contribution is limited. Moreover, from the power spectrum measurements, a lower limit to the I_ν contribution from unknown sources can be derived (Kashlinsky et al., 2007). The latest measurements of the NIRB power spectrum (Cooray et al., 2012a; Kashlinsky et al., 2012) established an excess power on scales larger then $\gtrsim 1$ arcmin, irreconcilable with emission from known galaxies up to $z \sim 5$ (Helgason et al., 2012). The origin of such a signal is still unknown.

Population III stars (PopIII) were one of the first hypothesis proposed about the sources of the NIRB excess (Santos et al., 2002; Salvaterra & Ferrara, 2003). Although intriguing, this idea was soon after discarded because of the very high formation efficiency required (Madau & Silk, 2005) and since it would overpredict the number of high-z dropout galaxies (Salvaterra & Ferrara, 2006). Several works explored the possibility of high redshift galaxies ($z \gtrsim 5$) being the sources of the NIRB excess, but models failed to reproduce the required levels of fluctuations (Fernandez et al., 2010; Cooray et al., 2012b; Yue et al., 2013a; Helgason et al., 2016).

An alternative solution was the intrahalo light (IHL), i.e light from stars stripped from their parent galaxy (Cooray et al., 2012a; Cheng & Bock, 2022). Despite its success in reproducing observations, such idea has to rely on poorly understood abundance of intrahalo stars (Ferrara, 2012). Moreover, this model cannot account for the observed cross-correlation of the NIRB with the soft-X background (SXB) (Cappelluti et al., 2013, 2017b). Such a feature is difficult to explain even with galaxies spectra, but could be naturally justified by X-ray emission from accretion disks around black holes. Yue et al. (2013b) developed a model to explain both NIRB fluctuations and NIRB-SXB cross correlation with accreting direct collapse black holes (DCBHs), even though it is unclear whether the specific conditions of DCBHs formation are actually realized during cosmic evolution (Latif & Ferrara, 2016).

Given the puzzling nature of the NIRB excess, a new scenario has been recently suggested, invoking Primordial Black Holes (PBHs) (Kashlinsky, 2016; Cappelluti et al., 2022). PBHs are black holes formed deep into radiation dominated era from the collapse of overdensity peaks (Zel'dovich & Novikov, 1967; Carr & Hawking, 1974) and interest on them have been rejuvenated after the first detection of gravitational waves from black holes merger (Abbott et al., 2016; Bird et al., 2016; Blinnikov et al., 2016; Sasaki et al., 2016). The primordial origin of LIGO/VIRGO black holes is a viable solution to explain their observed mass spectrum and merger rates (Raidal et al., 2017; Ali-Haïmoud et al., 2017; Wong et al., 2021). Moreover, they could justify why most of the measured effective spins are close to zero (Abbott et al., 2019; De Luca et al., 2020) and could accomodate for black holes with masses in the pair-instability supernovae mass gap (45–120 $\mathrm{M}_\odot$) (Abbott et al., 2020a; De Luca et al., 2021; O'Brien et al., 2021) and in the low mass gap (2.5–5 $\mathrm{M}_\odot$) (Abbott et al., 2020c,b; Clesse & García-Bellido, 2022). Finally, the recent evidence of a gravitational-wave background reported by the NANOGrav collaboration (Agazie et al., 2023) could directly probe PBH formation from high amplitude peaks of the primordial power spectrum (Clesse & García-Bellido, 2017; Vaskonen & Veermäe, 2021; Franciolini et al., 2023).

A key aspect about PBHs is that they were proposed as cold dark matter candidates (Chapline, 1975). This hypothesis has been investigated in a plethora of studies, providing constraints on the fraction of DM comprised by PBHs (see Carr & Kühnel (2020) for a

review). The presence of PBHs would entail a variety of astrophysical phenomena, such as gamma rays emission from evaporating PBHs (Laha, 2019; Coogan et al., 2021), microlensing effects (Niikura et al., 2019; Blaineau et al., 2022) and disruption of wide binaries or ultra-faint dwarfs (Monroy-Rodríguez & Allen, 2014; Brandt, 2016). In addition, accreting PBHs would impact the CMB spectrum and anisotropies (Poulin et al., 2017; Serpico et al., 2020), the 21 cm power spectrum (Mena et al., 2019) and would produce radio and X-ray backgrounds (Cappelluti et al., 2022; Ziparo et al., 2022).

When deriving constraints on the abundance of PBHs, it is commonly assumed that PBHs have the same mass (i.e. a δ-function), although these constraints actually depend on the adopted PBH mass function (Kühnel & Freese, 2017). In particular, PBH formation models in slow-roll inflation predict an approximately lognormal mass function (Dolgov & Silk, 1993; Kannike et al., 2017), while latest simulations of PBH formation across the QCD epoch derived a mass function peaked around $M_{\rm PBH} \sim 1\,{\rm M}_{\odot}$, with a non-trivial shape departing from lognormal (Franciolini et al., 2022).

If PBHs constitute a fraction of dark matter, they would add a poissonian component to the matter power spectrum (Meszaros, 1975; Afshordi et al., 2003; Ali-Haïmoud, 2018), accelerating structure formation and consequently enhancing the abundance of haloes in which stars can form (Kashlinsky, 2016). This effect on the star formation process is particularly relevant for what concerns the NIRB excess puzzle, since a higher star formation rate density at high-z can then provide the required levels of NIRB fluctuations (Cappelluti et al., 2022). Moreover, PBHs could directly contribute to the NIRB with the radiation emitted by accreting gas from their surroundings.

Hasinger (2020, hereafter H20) computed cosmic backgrounds from gas accretion onto PBHs and could recover only 0.3 per thousand of the NIRB with his model. However, H20 considered gas accretion only in the intergalactic medium (IGM), while PBHs could accrete matter also in dense virialized structures, i.e DM haloes. In particular, Ziparo et al. (2022, hereafter Z22) have shown that the contribution of PBHs accreting in DM haloes to X-ray and Radio backgrounds is > 60 per cent larger than those accreting in the IGM.

In this Chapter, following the model by Z22, we compute the NIRB produced by PBHs taking into account both PBH accretion in DM haloes and a self-consistent treatment of X-ray ionization and heating of the IGM. We further improve the Z22 model both considering the modification of the matter power spectrum induced by the presence of the PBHs, previously neglected, and generalizing the framework to extended mass functions. In Section 7.2 we summarize the basic model and present its extensions. In Section 7.3 we present the main results of this work. Finally, we discuss our results and state our conclusions in Section 7.4.

Throughout the paper we assume a flat Universe with the following cosmological parameters: $\Omega_m = 0.3075$, $\Omega_\Lambda = 1 - \Omega_m$, $\Omega_b = 0.0486$, $H_0 = 67.74$ km s^{-1}Mpc^{-1} , $n_s = 0.965$ and $\sigma_8 = 0.811$ (**?**).

7.2 Methods

To investigate the contribution of PBHs to the NIRB we rely on the formalism described in Z22. We first revisit their model in order to introduce the framework (Section 7.2.1, 7.2.2). We then compute the intensity and angular power spectrum of the NIRB in Section 7.2.3. In the last two Sections we extend the model to account for the modification of matter power spectrum induced by PBHs (Section 7.2.4) and extended mass functions (Section 7.2.5).

7.2.1 Cosmological distribution of PBHs

Assume that a DM fraction $f_{\rm PBH}$ is made of PBHs of mass $M_{\rm PBH}$. DM distribution on cosmological scales can be described as a diffuse component with density equal to the mean DM density, and virialized regions where matter has collapsed into DM haloes. As PBHs are distributed as the DM, we decompose the number density of PBHs as

$$n_{\rm PBH}(z) = \frac{f_{\rm PBH}\Omega_{\rm DM}\rho_c(1+z)^3}{M_{\rm PBH}} = n^{\rm IGM}_{\rm PBH}(z) + n^{h}_{\rm PBH}(z), \tag{7.1}$$

where $n^{\rm IGM}_{\rm PBH}$ ($n^{h}_{\rm PBH}$) is the number density of PBHs in the intergalactic medium (haloes). The abundance of PBHs in haloes is related to the collapsed fraction of DM in haloes $f_{\rm coll}$, which can be computed as

$$f_{\rm coll}(M_h, z) = {\rm erfc}\Big(\frac{\delta_{\rm crit}(z)}{\sigma_M}\Big) \tag{7.2}$$

in the Press-Schechter formalism (Press & Schechter, 1974). Here $\delta_{\rm crit}(z) = 1.68/D(z)$ is the critical overdensity for collapse, $D(z)$ is the growth factor and σ^2_M is the mass variance of the linearly extrapolated matter overdensity field. Thus, the number density of PBHs in the IGM and in haloes are

$$n^{\rm IGM}_{\rm PBH}(z) = (1 - f_{\rm coll})n_{\rm PBH}(z), \quad n^{h}_{\rm PBH}(z) = f_{\rm coll}n_{\rm PBH}(z). \tag{7.3}$$

PBH distribution inside haloes

The distribution of PBHs inside haloes follows the DM density profile, here assumed to be NFW (Navarro et al., 1996):

$$\rho_{\rm DM}(x) = \frac{\rho_c \delta_c}{cx(1+cx)^2}, \tag{7.4}$$

where $x = r/r_{\rm vir}$ is the radial distance in virial radius units and c is the concentration parameter from Macciò et al. (2007). Following Z22, we model its redshift evolution as $c \propto (1+z)^{-1}$. The parameter δ_c is a function of both the concentration parameter and the overdensity at the collapse redshift Δ_c (Barkana & Loeb, 2001):

$$\delta_c = \frac{\Delta_c}{3} \frac{c^3}{\ln(1+c) - c/(1+c)}, \tag{7.5}$$

with $\Delta_c = 18\pi^2 + 82d - 39d^2$, $d = \Omega_m^z - 1$ and $\Omega_m^z = \Omega_m(1+z^3)/(\Omega_m(1+z^3) + \Omega_\Lambda)$. Being PBHs distributed as DM, the number of PBHs within radius r an $r + {\rm d}r$ is

$$ {\rm d}N_{\rm PBH}(r) = \frac{f_{\rm PBH}}{M_{\rm PBH}} 4\pi r^2 \rho_{\rm DM}(r) {\rm d}r. \tag{7.6}$$

7.2.2 PBHs accretion

To estimate the accretion rate of gas onto PBHs, we adopt the Bondi–Hoyle–Lyttleton formula (Bondi, 1952; Edgar, 2004):

$$\dot{M} = \lambda 4\pi \frac{G^2 M_{\rm PBH}^2 \rho_b}{(c_s^2 + v_{\rm BH}^2)^{3/2}}, \tag{7.7}$$

where ρ_b and c_s are the density and sound speed of the accreting gas, respectively, $v_{\rm BH}$ is the relative velocity between the PBH and the gas, and λ is the accretion parameter that accounts for non gravitational effects (i.e radiative feedback, gas pressure, outflows). Following Poulin et al. (2017), we adopt the value $\lambda = 0.01$, which is a benchmark for an advection dominated accretion flow (ADAF, Yuan & Narayan, 2014).

Accretion conditions in the IGM and inside haloes differ substantially: in the following we describe the relevant physical quantities, i.e. ρ_b, c_s and $v_{\rm BH}$, separately for the two cases.

Accretion in the IGM

Following Ricotti et al. (2008), we assume a uniform gas density in the IGM, equal to

$$\rho_{\rm IGM}(z) = 250\, \mu m_p \Big(\frac{1+z}{1000}\Big)^3 \, {\rm g\ cm^{-3}}, \tag{7.8}$$

where $\mu = 1.22$ is the mean molecular weight for a gas of primordial composition and m_p is the proton mass. The sound speed of the gas is given by:

$$c_s = \sqrt{\frac{k_B T_{\rm IGM}}{\mu m_p}}, \tag{7.9}$$

where k_B is the Boltzmann constant and $T_{\rm IGM}$ is the IGM temperature. The relative velocity between baryons and PBHs is gaussianly distributed on linear scales, hence its modulus follows a maxwellian distribution, with variance given by (Ali-Haïmoud & Kamionkowski, 2017)

$$\sigma_{\rm rel}^2(z) \equiv \langle v_{\rm BH}^2 \rangle = 30\ min\Big[1, (1+z)/1000\Big] \, {\rm km\ s^{-1}}. \tag{7.10}$$

To properly account for the distribution of relative velocities, it is useful to define an effective velocity $v_{\rm eff}$ (Ricotti et al., 2008), whose analytical expression is (Mena et al., 2019)

$$v_{\rm eff} = \sigma_{\rm rel}(z) \Big[\Big(\frac{3}{2}\Big)^{3/2} U\Big(\frac{3}{2}, 1, \frac{3}{2}\Big(\frac{\sigma_{\rm rel}}{c_s}\Big)^{-2}\Big)\Big]^{-1/3}, \tag{7.11}$$

where $U(a,b,z)$ is the confluent hypergeometric function of second kind. The accretion rate of PBHs in the IGM is finally obtained by substituting the relevant quantities computed above in equation (7.7).

Accretion within haloes

To model the internal structure of haloes, we assume that the gas is in thermal equilibrium at the virial temperature $T_{\rm vir}$. Moreover, we impose hydrostatic equilibrium between DM and gas. Given these assumptions, the density profile of gas is described by the following equation (Makino et al., 1998):

$$\rho_b(r) = \rho_{b,0} \exp\Big[- \frac{\mu m_p}{2 k_B T_{\rm vir}} \Big(V_{\rm esc}^2(0) - V_{\rm esc}^2(r) \Big) \Big], \tag{7.12}$$

where $V_{\rm esc}$ is the escape velocity, given by:

$$V_{\rm esc}^2(r) = 2 \int_r^{r_{\rm vir}} {\rm d}r' \frac{G M(r')}{r'^2}, \tag{7.13}$$

and $\rho_{b,0}$ is a normalization constant set by imposing:

$$4\pi \int_0^{r_{\rm vir}} {\rm d}r r^2 \rho_b(r) = \frac{\Omega_b}{\Omega_{\rm DM}} M_h, \tag{7.14}$$

where M_h is the halo mass, Ω_b and $\Omega_{\rm DM}$ are the total baryon and DM densities in units of the critical density. The sound speed in haloes can be computed via equation (7.9), substituting $T_{\rm IGM}$ with $T_{\rm vir}$. As a consequence of hydrostatic equilibrium assumption, we set $v_{\rm BH} = 0$.

7.2.3 NIRB

To compute the specific luminosity of PBHs we follow Z22. Given the accretion rate $\dot{M}$, the bolometric luminosity of a single PBH is $L = \varepsilon \dot{M} c^2$, where $\varepsilon = 0.1$ is the radiative efficiency. We assume that, as for astrophysical black holes, the spectrum of PBHs can be described by a double power-law with an exponential cut-off (H20):

$$L_\nu \propto \begin{cases} \left(\frac{\nu}{\nu_c}\right)^{\alpha_{\rm sync}} & \nu \leq \nu_c \\ \left(\frac{\nu}{\nu_c}\right)^{\alpha} & \nu > \nu_c \end{cases} \tag{7.15}$$

where the cut-off frequency is $\nu_{\rm cut} = 200\,{\rm keV}$ and $\alpha = -0.7$. Below the critical frequency $\nu_c = \lambda_c / c$, with $\lambda_c = 0.45 (M_{\rm PBH}/{\rm M}_\odot)^{0.4} \mu\,{\rm m}$, synchrotron emission dominates and the power law index is $\alpha_{\rm sync} = 1.86$ (H20). The above spectral shape is consistent with an ADAF accretion model with accretion rates $\dot{m} = \dot{M}/\dot{M}_{\rm EDD} \gtrsim 10^{-2}$, which holds for those PBHs producing the bulk of the background radiation in our model. We fix the normalization of the spectrum by setting the bolometric correction in the 2–10 keV band to $f_X = 0.1$ (H20).

Given the specific luminosity, L_ν, the specific emissivity of a population of PBHs accreting in the IGM is

$$\dot{\rho}_{\rm IGM}(\nu, z) = n_{\rm PBH}^{\rm IGM}(z) L_\nu(z). \tag{7.16}$$

The specific luminosity of an entire halo can be computed by:

$$L_\nu^h(z) = \int_0^{R_{\rm vir}} {\rm d}r \frac{{\rm d}N_{\rm PBH}}{{\rm d}r} L_\nu(r, z). \tag{7.17}$$

The specific emissivity of a population of PBHs accreting inside haloes is then given by integrating over the halo mass function (Murray et al., 2013):

$$\dot{\rho}_h(\nu, z) = \int_{M_{\rm min}}^{M_{\rm max}} {\rm d}M L_\nu^h(M) \frac{{\rm d}n}{{\rm d}M}, \tag{7.18}$$

where $M_{\rm max} = M_h(T_{\rm vir} = 10^4)$ is the minimum mass of haloes inside which stars can form and $M_{\rm min}$ is the minimum mass of haloes required to form a baryon overdensity (Barkana & Loeb, 2001):

$$M_{\rm min}(T_{\rm IGM}, z) = 1.3 \times 10^3\,{\rm M}_\odot \Big(\frac{10}{1+z} \Big)^{3/2} \Big(\frac{T_{\rm IGM}}{1\,{\rm K}} \Big)^{3/2}. \tag{7.19}$$

Inside haloes with $M_h < M_{\rm min}$, the gas density is close to the mean IGM one and therefore we consider their contribution in the IGM emissivity.

The background intensity in a given band [ν_1,ν_2] is related to the specific emissivity by (Fernandez et al., 2010; Yue et al., 2013a):

$$I^{[\nu_1,\nu_2]} = \frac{c}{4\pi}\int \mathrm{d}z \frac{\int_{\nu_1}^{\nu_2}\mathrm{d}\nu \varepsilon_{\nu'}(z)}{H(z)(1+z)}, \tag{7.20}$$

where $\nu' = (1+z)\nu$ and $H(z)$ is the Hubble parameter as a function of redshift. The angular power spectrum of NIRB fluctuations from PBHs can be decomposed in a two-halo and a shot-noise term:

$$C_l = C_l^{\text{2-halo}} + C_l^{\text{SN}}. \tag{7.21}$$

The clustering component at frequency ν and for the multiple moment l is given by (Cooray et al., 2004; Fernandez et al., 2010)

$$C_l^{\text{2-halo}} = \frac{c}{4\pi}\int \mathrm{d}z \frac{\epsilon^2_{\nu'}(z)}{H(z)r^2(z)(1+z)^2} P\Big(k=\frac{l}{r(z)}, z\Big), \tag{7.22}$$

where $r(z)$ is the comoving distance and $P(k,z)$ is the power spectrum of the underlying matter distribution. PBHs in the IGM correspond to DM in the linear regime and therefore $P_{\text{IGM}}(k,z) = P_{\text{lin}}(k,z)$, where the right hand side is the linear matter power spectrum. Instead, haloes are biased tracers of the linear matter density field and their power spectrum can be written as $P^h(k,z) = b_{\text{eff}}(z)P(k,z)$, where the effective bias b_{eff} is given by:

$$b_{\text{eff}}(z) = \int_{M_{\text{min}}}^{M_{\text{max}}} \mathrm{d}M b_h(M,z)\frac{\mathrm{d}n}{\mathrm{d}M} \Big/ \int_{M_{\text{min}}}^{M_{\text{max}}} \mathrm{d}M \frac{\mathrm{d}n}{\mathrm{d}M}, \tag{7.23}$$

where $b_h(M,z)$ is the halo bias, as derived in Tinker et al. (2010).

The shot noise angular power spectrum is described by the following equation (Cooray et al., 2012a; Yue et al., 2013a):

$$C_l^{\text{SN}} = \frac{c}{(4\pi)^2}\int \frac{\mathrm{d}z}{H(z)r^2(z)(1+z)^2}\int_{M_{\text{min}}}^{M_{\text{max}}} \mathrm{d}M L_\nu^2(M)\frac{\mathrm{d}n}{\mathrm{d}M}. \tag{7.24}$$

We note that in principle one should consider the one-halo term, given by (Cooray et al., 2012a):

$$C_l^{\text{1-halo}} = \frac{c}{(4\pi)^2}\int \frac{\mathrm{d}z}{H(z)r^2(z)(1+z)^2} \tag{7.25}$$

$$\int_{M_{\text{min}}}^{M_{\text{max}}} \mathrm{d}M L_\nu^2(M)\frac{\mathrm{d}n}{\mathrm{d}M}|\tilde{u}(k=l/r(z),M)|^2, \tag{7.26}$$

where $\tilde{u}(k=l/r(z),M)$ is the Fourier transform of the NFW profile. For the redshift and halo mass range of interest, we checked that $\tilde{u}(k=l/r(z),M) \sim 1$ and therefore the one-halo term reduces to the shot noise term in equation (7.24).

7.2.4 Matter Power spectrum modified by PBHs

PBHs may constitute a fraction of DM, thus they would add a Poisson shot noise term to the linear matter power spectrum (Meszaros, 1975; Afshordi et al., 2003):

$$P_{\text{poiss}} = \frac{f_{\text{PBH}}^2}{n_{\text{PBH,0}}}, \tag{7.27}$$

where $n_{\text{PBH,0}}$ is the PBH number density at redshift $z=0$. The total matter power spectrum can be then written as (Villanueva-Domingo & Ichiki, 2023):

$$P_{\text{PBH}-\Lambda\text{CDM}}(z,k) = P_{\Lambda\text{CDM}}(k,z) + D^2(z)T_{\text{iso}}^2(k)P_{\text{poiss}}, \tag{7.28}$$

where $D(z)$ is the linear growth factor and T_{iso} is the isocurvature transfer function. An approximate expression for T_{iso} is given by (Peacock, 1998):

$$T_{\text{iso}} = \begin{cases} \frac{3}{2}(1+z_{\text{eq}}), & k \geq k_{\text{eq}} \\ 0, & k < k_{\text{eq}} \end{cases} \tag{7.29}$$

where z_{eq} is the redshift of radiation-matter equality and $k_{\text{eq}} = c^{-1}H(z_{\text{eq}})/(1+z_{\text{eq}})$. The contribution to the power spectrum from PBHs can be recast in the form (Villanueva-Domingo & Ichiki, 2023):

$$P_{\text{PBH}} = T_{\text{iso}}^2 P_{\text{poiss}} = 2.5\times10^{-2}\, f_{\text{PBH}}\Big(\frac{M_{\text{PBH}}}{30\,\mathrm{M}_\odot}\Big)\ \mathrm{Mpc}^3. \tag{7.30}$$

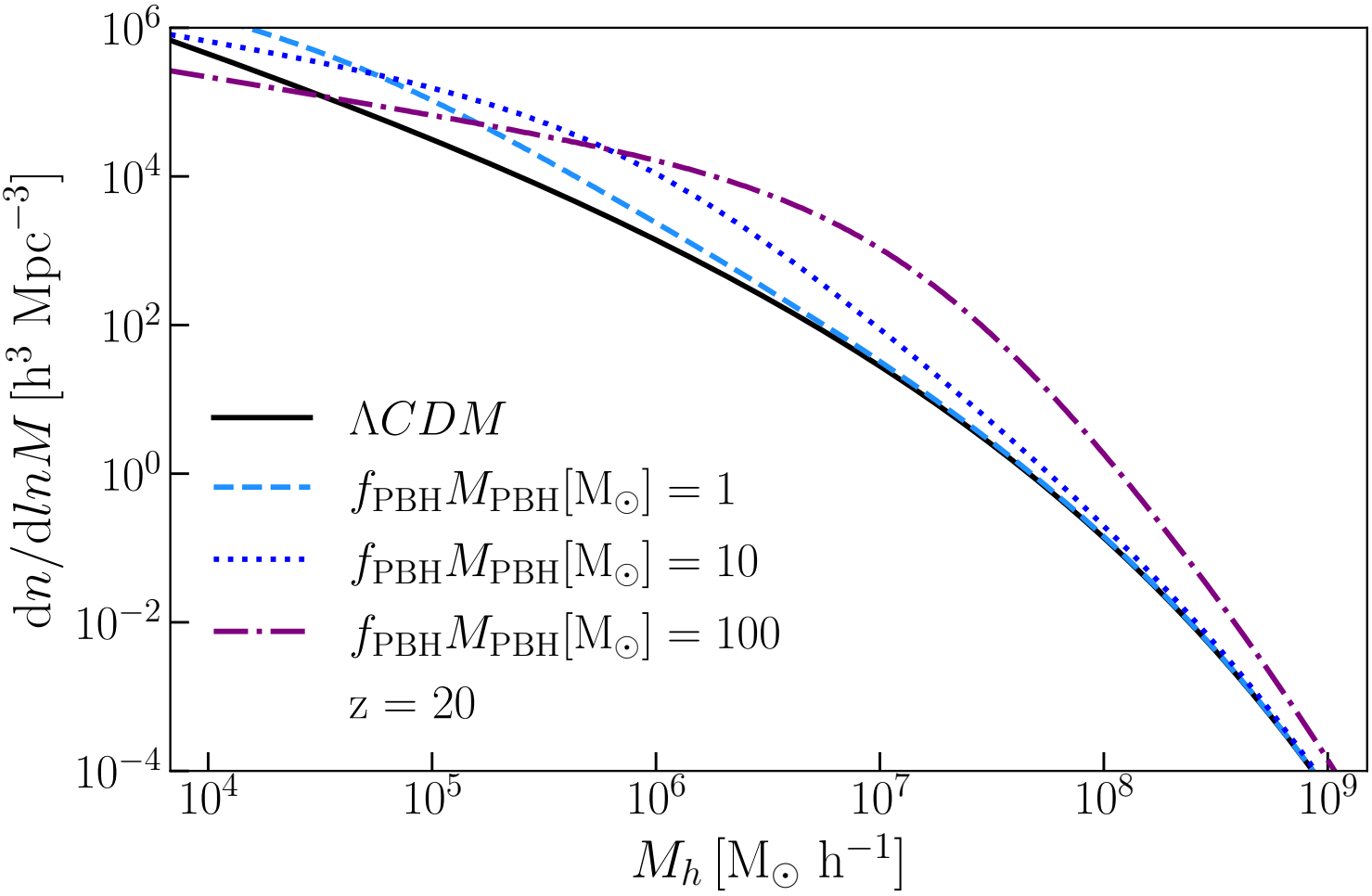

Figure 7.1: Press–Schechter halo mass function at $z = 20$, in the standard ΛCDM scenario (black solid line) and including the modification induced by PBHs, with $f_{\mathrm{PBH}} M_{\mathrm{PBH}} = 1\ \mathrm{M}_\odot$ (light blue dashed), $f_{\mathrm{PBH}} M_{\mathrm{PBH}} = 10\ \mathrm{M}_\odot$ (blue dotted) and $f_{\mathrm{PBH}} M_{PBH} = 100\ \mathrm{M}_\odot$ (purple dot-dashed).

The PBH modification to the power spectrum affects the variance of the matter overdensity field and thus the halo mass function.

Hereafter we will refer to a PBH-ΛCDM cosmology whenever adopting the power spectrum described by equations (7.28)–(7.30). In particular we consider a PBH-ΛCDM cosmology in our models PBH-δ and PBH-lognormal (see Sec. 7.3). In Fig. 7.1 we show the Press–Schechter halo mass function at $z = 20$ in the standard ΛCDM scenario and including the modification induced by PBHs, for different values of the parameter $f_{\mathrm{PBH}} M_{\mathrm{PBH}}$. At $z = 20$, when including the extra power on small scales due to PBHs, the halo mass function is a factor of 3 (40) higher for $M_h = 10^5\ \mathrm{M}_\odot$ ($M_h = 10^7\ \mathrm{M}_\odot$) with respect to the standard ΛCDM case, considering $f_{\mathrm{PBH}} M_{\mathrm{PBH}} = 100$. In Fig. 7.2 we compare the bolometric emissivity, from both haloes and IGM, in the ΛCDM and PBH-ΛCDM cosmologies, as a function of redshift. As a consequence of the increased number of small haloes expected in the PBH-ΛCDM, the contribution to the total emissivity from accreting PBHs in DM haloes is enhanced by a factor of 2 (20) at redshift $z = 30$ (40). Moreover, also the collapsed DM fraction is higher and thus the relative contribution from PBHs accreting in the IGM is further lowered. The emissivity of PBHs accreting in haloes at redshift $z = 20\ (40)$ is roughly 10 (100) times the emissivity from PBHs in the IGM. We point out that, as a consequence of the aforementioned effects, in the PBH-ΛCDM cosmology halo emissivity dominates the IGM one at any redshift, unlike in the standard ΛCDM case.

7.2.5 Extended PBH mass function

The mass function of PBHs at the epoch of their formation is denoted by $\psi(M_{\mathrm{PBH}})$, and defined as:

$$\psi(M_{\mathrm{PBH}}) = \frac{1}{f_{\mathrm{PBH}}} \frac{\mathrm{d}f_{\mathrm{PBH}}}{\mathrm{d}M_{\mathrm{PBH}}}. \tag{7.31}$$

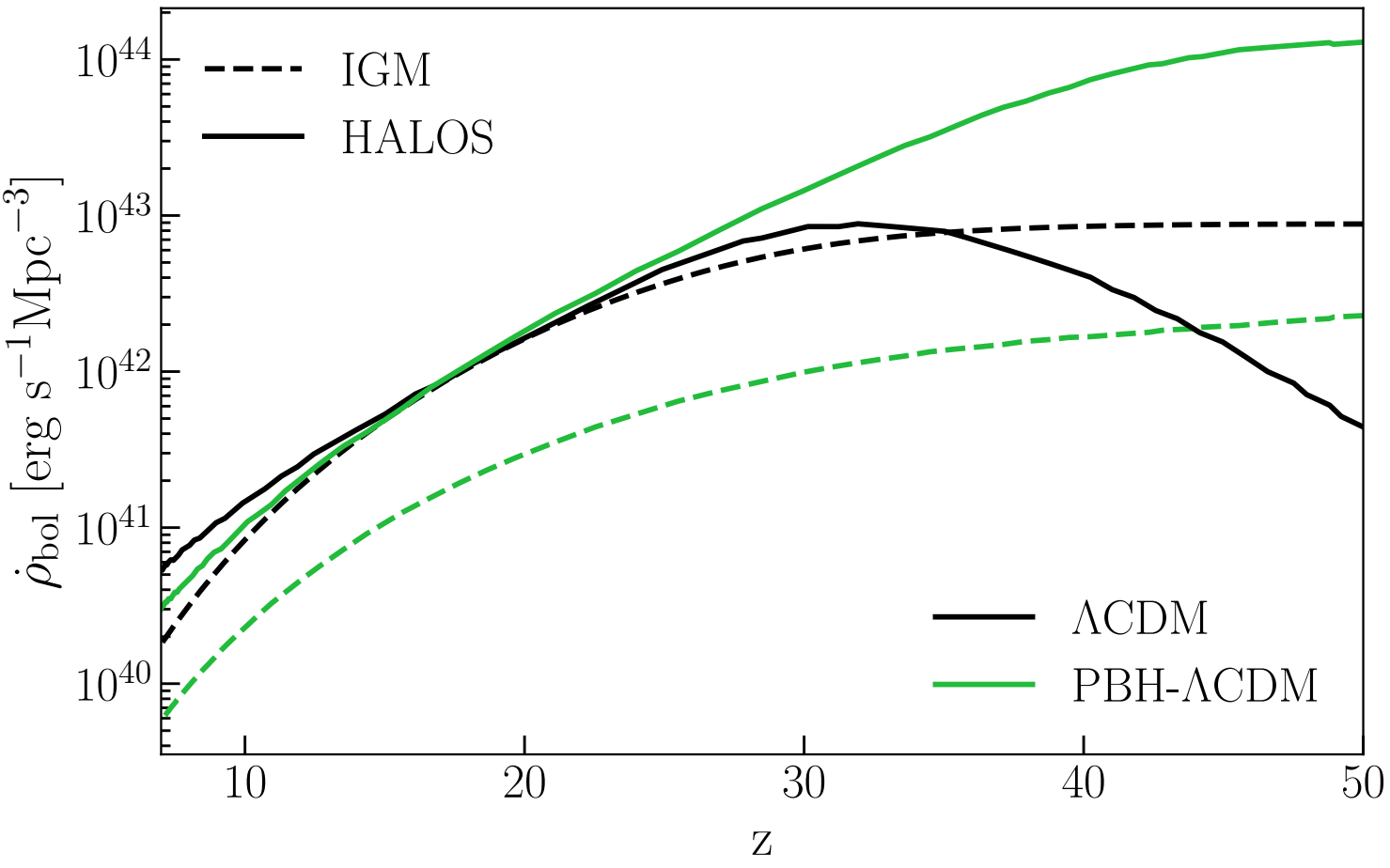

Figure 7.2: Bolometric emissivity from IGM (dashed lines) and haloes (solid lines), in the standard ΛCDM scenario (black) and including the power spectrum modified by PBHs (green). In the case of PBH-ΛCDM cosmology, the halo signal dominates over the IGM one for all the redshift of interest. Here we adopt $M_{\rm PBH} = 30\ {\rm M}_\odot$.

In the following, we generalize our formalism to extended mass functions. In particular, we consider the case of a lognormal mass function[1]:

$$\psi_{\rm log}(M) = \frac{1}{M\sqrt{2\pi}\sigma}\exp\Big(-\frac{\log(M/M_c)^2}{2\sigma^2}\Big). \tag{7.32}$$

Here M_c is the critical mass that sets the position of the peak and σ is the standard deviation of the distribution. Regarding PBHs in the IGM, their emissivity can be generalized to

$$\dot{\rho}_{\rm IGM}(\nu,z) = \int {\rm d}M n^{\rm IGM}_{\rm PBH}(z,M)\psi(M)L_\nu(z,M), \tag{7.33}$$

where the integral is performed over the PBH mass and $n^{\rm IGM}_{\rm PBH}(z,M)$ is taken from equation (7.3). Recalling that $n^{\rm IGM}_{\rm PBH} \propto M^{-1}$ and $L_\nu \propto M^2$, we can write

$$\dot{\rho}_{\rm IGM} \propto \int {\rm d}M\psi(M)M \equiv \bar{M}. \tag{7.34}$$

Therefore, when computing the emissivity of PBHs in the IGM, an extended mass function is equivalent to a δ-function centered at the mean mass $\bar{M}$ of the mass function[2]. For a lognormal mass function, the mean mass is $\bar{M}_{\rm log} = M_c\exp(\sigma^2/2)$. We will assume the benchmark value $\sigma = 1$ throughout the rest of the paper and quote only the mean mass of the lognormal distribution.

Regarding PBHs accreting in haloes, we must specify how PBHs of different masses are distributed inside the halo. We note that the frictional acceleration exerted onto a body of mass M moving through a homogeneous distribution of particles of mass m ($m \ll M$) with isotropic velocity distribution is $\propto M$ (Binney & Tremaine, 2008). Hence, PBHs with higher masses sink towards the centre of the halo before lighter ones. With this in mind and for simplicity, we then assume that more massive PBHs lie at smaller radii.

The mass $M^*(r)$ of PBHs at a given radius r can be derived by imposing that the mass $M(r)$ enclosed in a sphere of radius r is equal to the integrated mass of all PBHs more massive than $M^*(r)$:

$$M(r) = 4\pi\int_0^r {\rm d}r' r'^2\rho_{\rm NFW}(r') = \int_{M^*(r)}^\infty {\rm d}M' M'\psi(M'). \tag{7.35}$$

For a lognormal mass function, the right-hand side of the above equation can be computed analitically, giving

$$\log[M^*(r)/M_c] = \sigma^2 + \sqrt{2}\sigma\,{\rm erf}^{-1}\Big[1-\frac{2M(r)}{M_h}\Big], \tag{7.36}$$

where M_h is the halo mass. We show the resulting $M^*(r)$ for a lognormal mass function with $\bar{M}_{\rm log} = 30\ {\rm M}_\odot$ in Fig. 7.3. Once specified $M^*(r)$, the number of PBHs per unit length at radius r is given by

$$\frac{{\rm d}N_{PBH}}{{\rm d}r} = 4\pi\frac{f_{PBH}}{M^*(r)}\rho_{DM}(r). \tag{7.37}$$

We can then substitute equation (7.37) into equation (7.17) and apply the same formalism described in Sec. 7.2.3. In Fig. 7.4 we compare the bolometric luminosity of haloes in the case of a delta mass function with $M_{\rm PBH} = 30\ {\rm M}_\odot$ and of a lognormal mass function with $\bar{M}_{\rm log} = 30\ M_\odot$. Including the lognormal mass function boosts the halo luminosity by a factor of ~ 10, because more massive PBHs accrete at smaller distances from the center, where the gas density is higher.

7.3 Results

7.3.1 IGM temperature and ionization evolution

In this section we present the IGM temperature evolution, the mean NIRB intensity and the NIRB angular power spectrum obtained from three different models: (*i*) standard ΛCDM cosmology with a PBH delta mass function (ΛCDM-δ); (*ii*) PBH-ΛCDM cosmology with PBH delta mass function (PBH-δ) and (*iii*) PBH-ΛCDM cosmology with a PBH lognormal mass function (PBH-lognormal). We compare our predictions to observational data to test the hypothesis of accreting PBHs as sources of the NIRB.

[1] We choose a lognormal mass function to avoid fruitless complications. The main results of our work are unaffected by the exact shape of the mass function.

[2] This is valid for a constant radiation efficiency. If $\varepsilon \propto \dot{M}^a \propto M^{2a}$, then $L_\nu \propto M^{2+2a}$ and so the corresponding mean mass should be $\bar{M} = \Big(\int {\rm d}M\psi(M)M^{2a+1}\Big)^{1/(2a+1)}$.

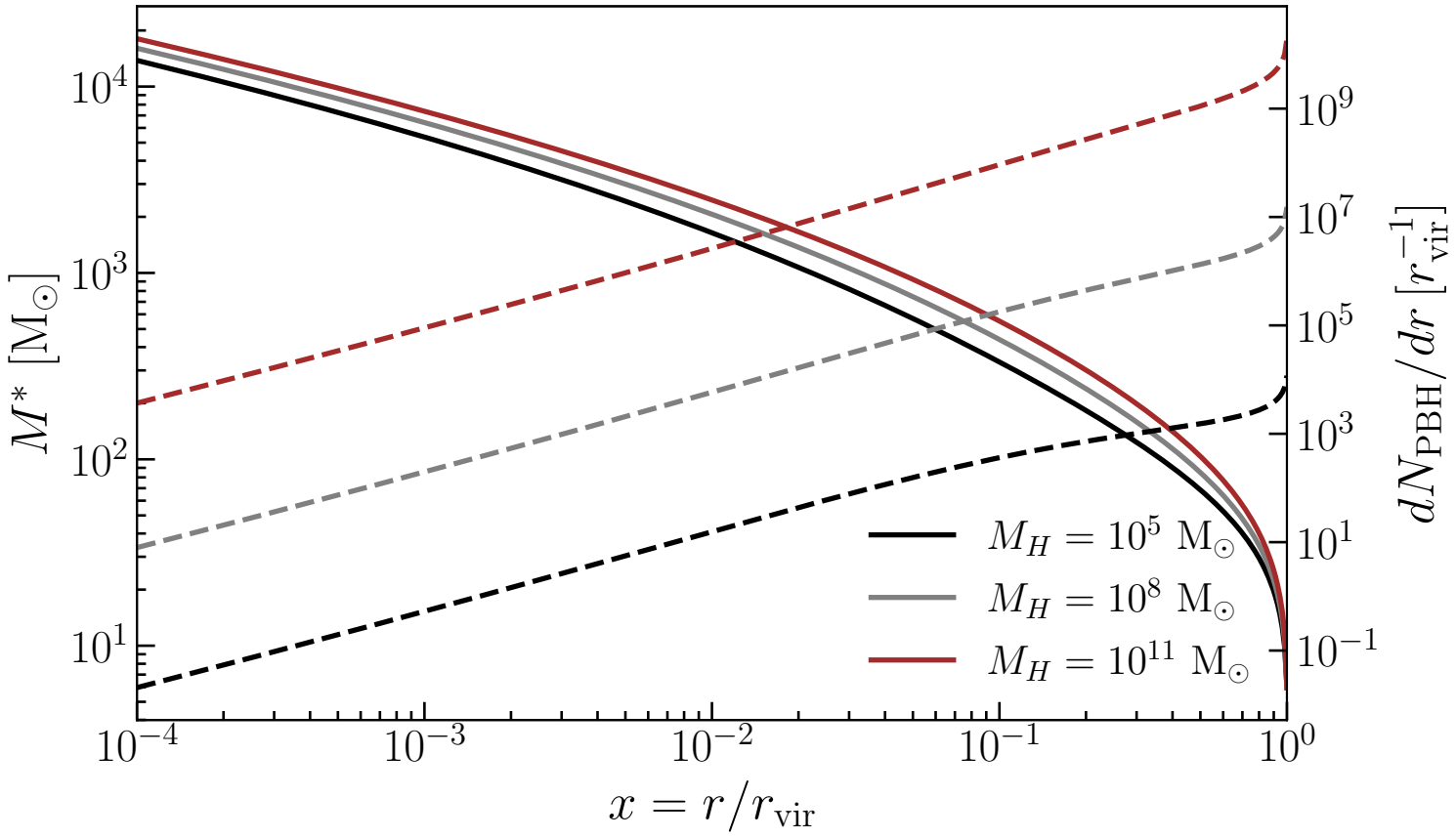

Figure 7.3: Mass of PBHs present at radius r in haloes of masses $10^5\,\mathrm{M}_\odot$ (black), $10^8\,\mathrm{M}_\odot$ (grey), $10^{11}\,\mathrm{M}_\odot$ (brown), when considering a lognormal mass function with $\bar{M}_{\rm log} = 30\,\mathrm{M}_\odot$. The dashed lines show the number of PBHs per unit length, in units of $r_{\rm vir}^{-1}$.

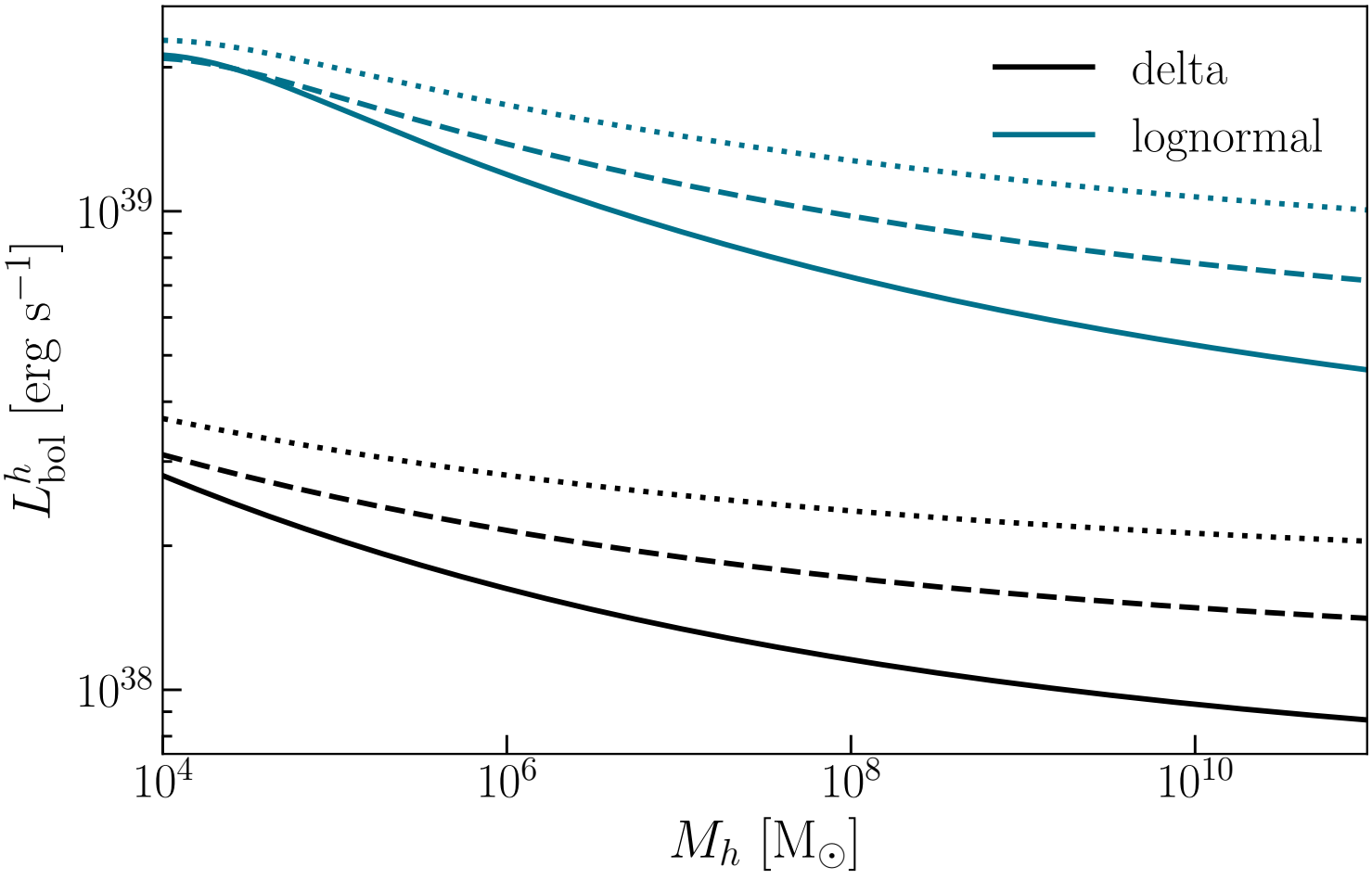

Figure 7.4: Bolometric luminosity of haloes as a function of the halo mass, in the case of a delta (black) and lognormal (blue) mass function, for $z = 20, 30, 40$ (solid, dashed, dotted respectively). The PBH mass for the delta mass function and the mean mass of the lognormal distribution are both set to $M_{\rm PBH} = \bar{M}_{\rm log} = 30\ M_\odot$. With an extended mass function, the luminosity is boosted by a factor ~ 10, because more massive PBH tend to sink towars the center where the gas density is higher.

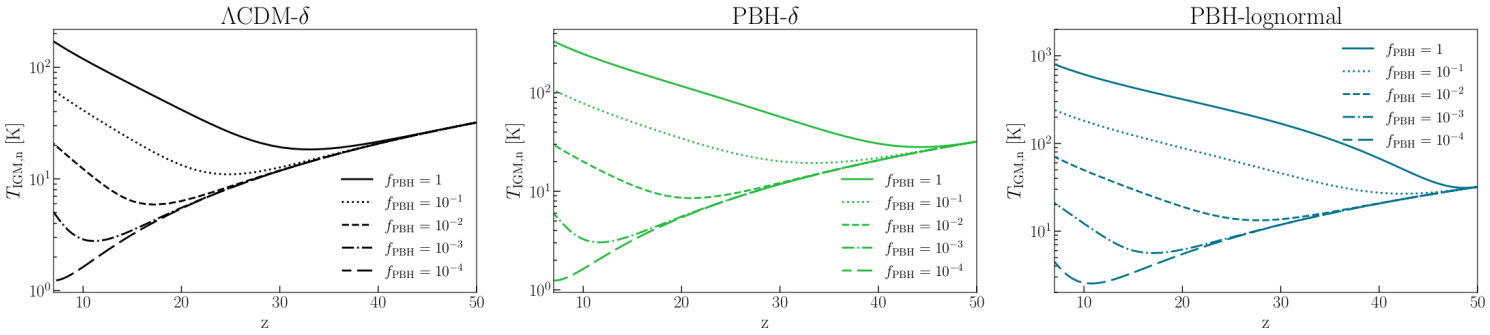

Figure 7.5: Evolution of the neutral IGM temperature as a function of redshift in the three different models ΛCDM-δ, PBH-δ and PBH-lognormal (black, green and blue respectively). Each line corresponds to different values of $f_{\rm PBH}$: 10^{-4}, 10^{-3}, 10^{-2}, 10^{-1}, 1 (long-dashed, dot-dashed, dashed, dotted and solid respectively). The PBHs mass is $M_{\rm PBH} = \bar{M}_{\rm log} = 30\ {\rm M}_\odot$. We maintain the same color-coding for the models throughout the rest of the paper.

7.3.2 IGM temperature and ionization evolution

X-ray emission from PBHs would heat and ionize the IGM well before galaxies start to reionize the Universe. To account for this effect, we self-consistently derive the IGM temperature and ionization evolution following the formalism described in Sec. 3 of Z22.

In the pre-overlap phase of the cosmic reionization process, the Universe can be split in ionized and neutral regions. In the ionized regions, the redshift evolution of the free electron fraction $x_e(z)$ is solved through equation (33a) in Z22, adopting the photoionization rate derived from the UV background in Puchwein et al. (2019). The free electron fraction traces the evolution of the volume filling factor of ionised regions, namely the fraction of volume occupied by ionized regions. In the same regions, we assume an IGM temperature $T_{\rm IGM,ion} = 10^4$ K. Such high temperature suppresses accretion onto PBHs due to high sound speeds (equation (7.9)).

In neutral regions, whose volume filling factor is $1 - x_e(z)$, the free electron fraction $x_{e,n}(z)$ evolves with redshift according to equation (35a) in Z22. Here, the photoionization rate calculation accounts for secondary ionizations due to X-rays emitted by PBHs:

$$\Gamma_{\rm PBH} = \int_{\nu_{\rm min}}^{\infty} {\rm d}\nu \frac{4\pi I_\nu}{h\nu} \left(\frac{h\nu}{E^{\rm th}} - 1 \right) f_{\rm ion} \sigma_H(\nu), \tag{7.38}$$

where $h\nu_{\rm min} = 0.5$ keV [3], $E^{\rm th}$ is the hydrogen ionization threshold, σ_H is the hydrogen ionization cross section and $f_{\rm ion} \sim 0.3$ is the fraction of the primary electron's energy going into secondary ionizations (Furlanetto & Stoever, 2010). In neutral regions we also solve the redshift evolution of temperature $T_{\rm IGM,n}(z)$ through equation (35b) in Z22, which takes into account the IGM heating due to the energy injected by X-rays (Mesinger et al., 2013), here assumed to be emitted by PBHs. The heating rate $\epsilon_{\rm PBH}$ per baryon can then be computed as:

$$\epsilon_{\rm PBH} = \int_{\nu_{\rm min}}^{\infty} {\rm d}\nu \frac{4\pi I_\nu}{h\nu} (h\nu - E^{\rm th}) f_{\rm heat} \sigma_H(\nu), \tag{7.39}$$

where $f_{\rm heat} \sim 0.3$ is the fraction of the primary electron's energy going into heat (Valdés et al., 2010).

Following the evolution of neutral regions $T_{\rm IGM,n}$ is crucial because changes in the IGM temperature affects PBHs emissivity. On the one hand, if the IGM temperature increases, the effective velocity of PBHs accreting in the IGM increases as well (equation (7.11)): this lowers their luminosity and consequently their emissivity. On the other hand, to higher $T_{\rm IGM,n}$ correspond higher $M_{\rm min}$ (equation (7.19)): the integration interval in equation (7.18) is thus shortened, which reduces the emissivity of PBHs accreting in haloes. Therefore, if $T_{\rm IGM,n}$ increases (decreases), the total emissivity of PBHs is lowered (enhanced).

We show the resulting temperature evolution in Fig. 7.5 for the three different models, adopting $M_{\rm PBH} = \bar{M}_{\rm log} = 30\ {\rm M}_\odot$ and $f_{\rm PBH} = 10^{-4}, 10^{-3}, 10^{-2}, 10^{-1}, 1$. For $f_{\rm PBH} = 1$, heating from PBHs increases the IGM temperature in neutral regions at $z \sim 6$ by a factor of $\sim 10, 20, 60$ in model ΛCDM-δ, PBH-δ, PBH-lognormal respectively, with respect to a ΛCDM cosmology which does not include PBHs. While in model ΛCDM-δ $T_{\rm IGM,n}$ starts increasing around $z \sim 30$, in model PBH-δ it rises at higher redshifts ($z \sim 40$), as the PBH emissivity is boosted by the higher number of small mass ($M_h \lesssim 10^6$–$10^7\ {\rm M}_\odot$) haloes. For $f_{\rm PBH} \lesssim 10^{-2}$, the effect of PBHs on the halo mass function is negligible and the evolution of $T_{\rm IGM,n}$ in the two cases is almost identical. In model PBH-lognormal, the luminosity of haloes is further enhanced by the lognormal mass function (Fig. 7.4) and $T_{\rm IGM,n}$ reaches ~ 900K at $z \sim 6$.

Before moving to the core results of this work, we briefly comment on the implications of IGM heating from PBHs. Firstly, our model does not affect the IGM temperature at $z \lesssim 5$, where measurements from Lyman-alpha forest observations are obtained (Walther et al.,

[3] We neglect the contribution of UV photons to IGM heating and ionization since, as discussed in Z22, Appendix B, the Stromgren sphere surrounding accreting PBHs results to be comparable to the Bondi radius, preventing UV photons to contribute to the IGM ionization.

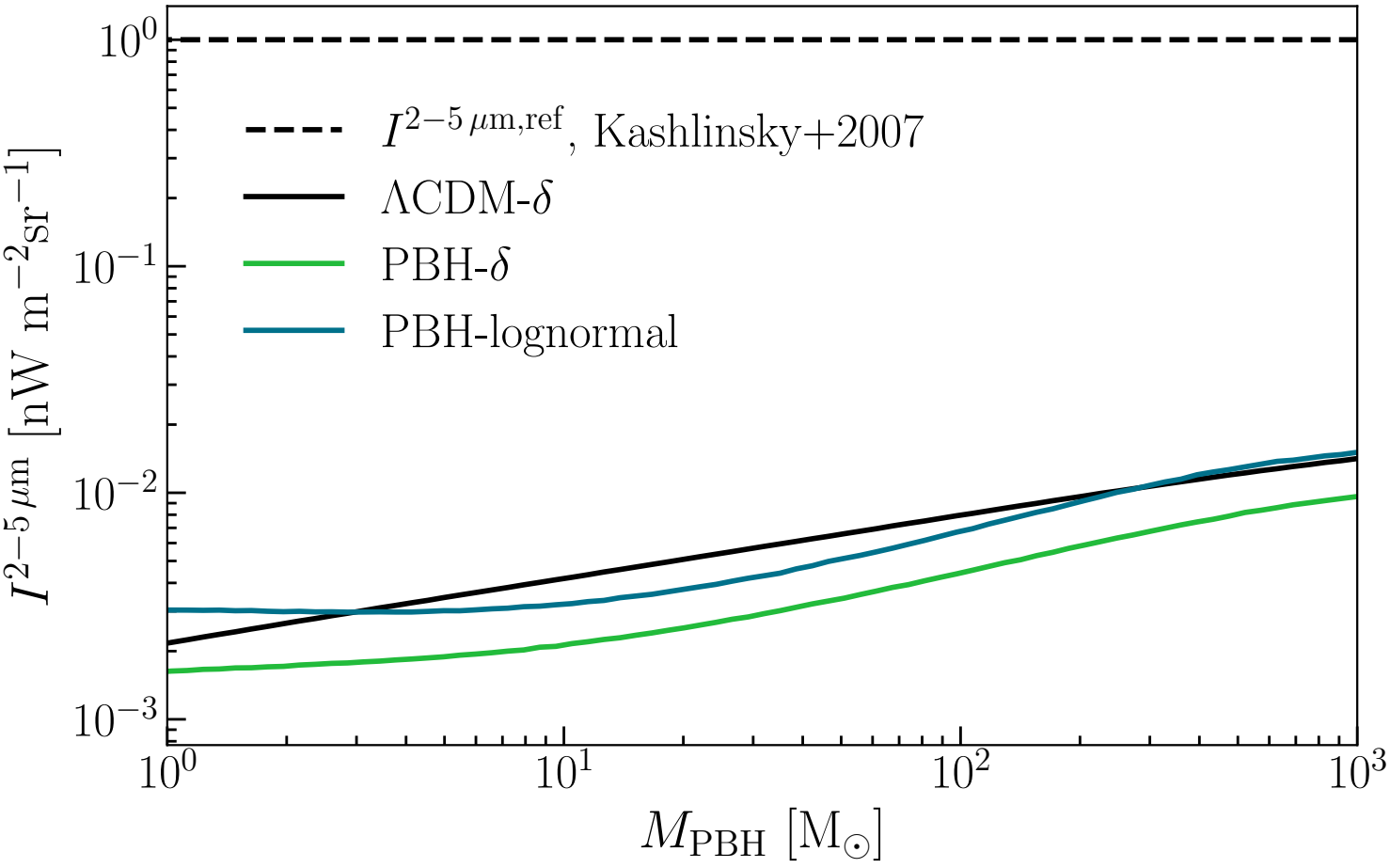

Figure 7.6: Near infrared background intensity in the band 2-5 μ m predicted by the three different models, as a function of PBH mass. The horizontal dashed line corresponds to the minimal near-infrared flux required by NIRB fluctuations (Kashlinsky et al., 2007).

2019; Gaikwad et al., 2020). Below $z \sim 6$, most of the Universe is ionized and IGM temperatures $T_{\mathrm{IGM,ion}} \gtrsim 10^4$ suppress the emission and thus the heating from PBHs in ionized regions. Moreover, the contribution from PBHs in neutral regions is also suppressed because their volume filling factor, i.e $1 - x_e$ in our model, approaches zero as cosmic reionization proceeds. Instead, at $z \gtrsim 10$, the Universe is mostly neutral and the volume filling factor of neutral regions is basically unity. Radiation from PBHs is then effective in heating the IGM above the adiabatic cooling temperature. Therefore, forthcoming 21 cm observations could provide stringent constraints on the heating from PBHs and hence on their abundance (Mena et al., 2019).

7.3.3 NIRB mean intensity and angular power spectrum

As already mentioned in the Introduction, direct measurements of the mean NIRB intensity are uncertain (Kashlinsky et al., 2018). However, constraints on the mean NIRB excess from unknown sources can be derived from the angular power spectrum measurement, as done by Kashlinsky et al. (2007), who found $I^{2-5\,\mu\,\mathrm{m}} \gtrsim 1$ nW m^{-2}sr^{-1} in the 2–5 μ m band.

NIRB mean intensity

We compute the mean NIRB intensity in the 2–5 μ m band, using equation (7.20). To test our predictions, in Fig. 7.6 we compare these results with data from Kashlinsky et al. (2007). We consider the limiting case $f_{\mathrm{PBH}} = 1$, which sets the upper limit for NIR flux produced by PBHs, for a mass range $1\,\mathrm{M}_\odot \leq M_{\mathrm{PBH}} = \bar{M}_{\mathrm{log}} \leq 10^3\,\mathrm{M}_\odot$. Our choice is driven, one the one hand, by the requirement of substantial accretion rates and hence luminosities and, on the other hand, by existing constraints on the abundance of higher mass PBHs. We show the results for the three different models in Fig. 7.6. We find that in the ΛCDM-δ (PBH-δ, PBH-lognormal) model, PBHs contribution to the NIRB mean intensity is at most 1.4 (0.9,1.5) per cent, if $M_{\mathrm{PBH}} = 10^3\,\mathrm{M}_\odot$.

However, current constraints on the abundance of PBHs (Carr & Kühnel, 2020) already exclude $f_{\mathrm{PBH}} = 1$ in the mass range considered here. Lower values of f_{PBH} result in lower NIR flux produced by PBHs. In Fig. 7.7 we show, as a function of PBH mass, the ratio between the intensity of the NIRB produced by PBHs computed considering the maximum value of f_{PBH} allowed by existing

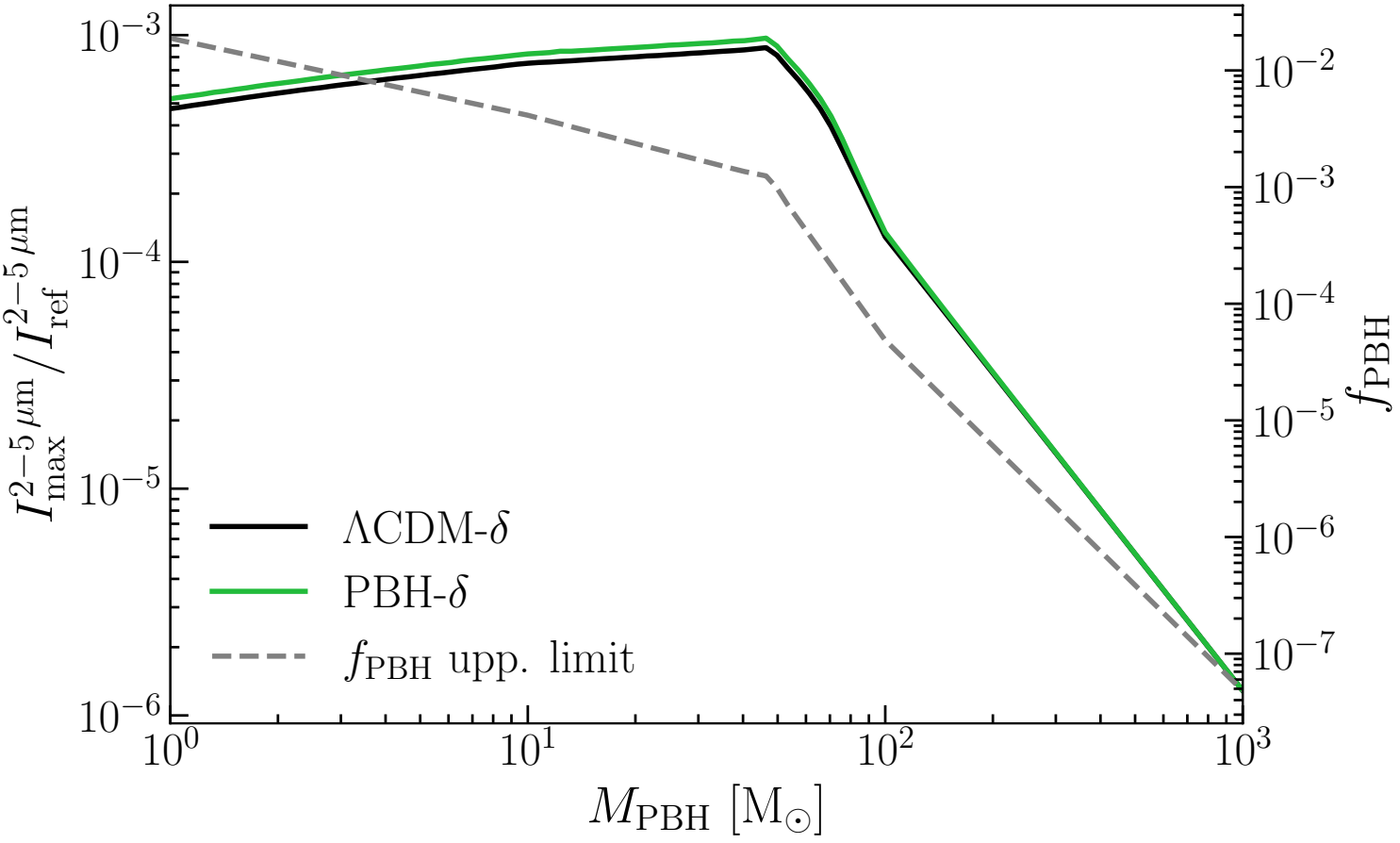

Figure 7.7: Maximum intensity of the NIRB produced by PBHs accounting for present constraints, in units of the reference value (1 nW m^{-2}sr^{-1}), for model ΛCDM-δ (solid black) and PBH-δ (solid green). We do not show the PBH-lognormal model, because available upper limits on f_{PBH} are derived only for a δ-mass function. We also plot the strongest constraint on f_{PBH} (dashed grey) as a function of the PBH mass. We use the LIGO and CMB bounds from PBHBounds (Kavanagh, 2019).

constraints and the NIRB mean intensity reference value. We also show the most stringent upper limit on f_{PBH}, which in the mass range of interest are derived from LIGO observations of black holes mergers (Abbott et al., 2017a; Kavanagh et al., 2018) and from CMB angular power spectrum (Poulin et al., 2017).

We find that, in the most favorable case consistent with constraints, PBHs can produce 0.1 per cent of the NIRB intensity if $M_{\mathrm{PBH}} \sim 50\,\mathrm{M}_\odot$. We show the results only for the ΛCDM-δ and PBH-δ models, as we consider constraints computed adopting a delta mass function. We note that the difference between the two models is very tiny, as for low values of f_{PBH} the modification induced by PBHs to the matter power spectrum is almost negligible.

NIRB angular power spectrum

We also compute the angular power spectrum of NIRB fluctuations produced by PBHs at the reference wavelength 3.6 μ m, using equations. (7.22) and (7.24). We show the results in Fig. 7.8, for the case $f_{\mathrm{PBH}} = 1$ and with PBH masses between $1\,\mathrm{M}_\odot$ (lower lines) and $10^3\,\mathrm{M}_\odot$ (upper lines). We compare our predictions with the latest measurements of NIRB angular power spectrum from Spitzer Deep, Wide-Field Survey (Cooray et al., 2012a).

None of the models considered in this work is able to reproduce the observed angular power spectrum. At multiple moment $l \sim 10^3$, corresponding to angular scales of $\theta = 2\pi/l \sim 20$ arcmin, fluctuations predicted by the ΛCDM-δ (PBH-δ, PBH-lognormal) model are lower than the measured one by a factor of $1000\ (400, 200)$. This holds for $M_{\mathrm{PBH}} = 10^3\,\mathrm{M}_\odot$, which provides the highest value of the angular power spectrum in the mass range considered here.

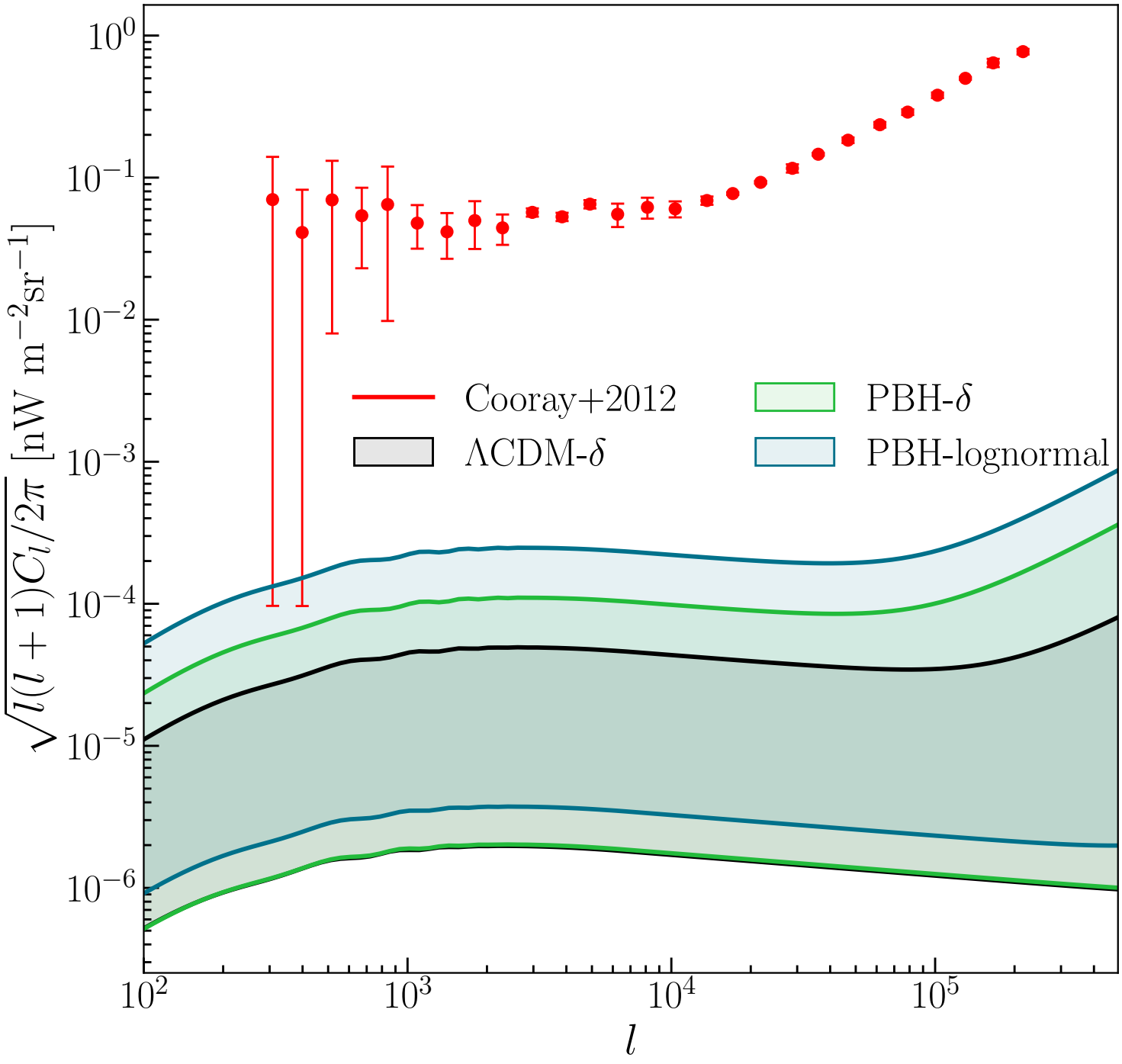

Figure 7.8: Angular power spectrum of the NIRB at 3.6 μm from PBHs for the three models, compared with observational data from Cooray et al. (2012a). Shaded regions correspond to values of PBH mass between $1\ \mathrm{M}_\odot$ (lower lines) and $10^3\ \mathrm{M}_\odot$ (upper lines).

7.4 Discussion and summary

In this work, we have tested the hypothesis that PBHs are sources of the NIRB excess. By assuming that PBHs constitute a fraction $f_{\rm PBH}$ of cold dark matter (DM), we have computed the mean intensity and angular power spectrum of the NIRB arising from their accretion.

Following the formalism by Ziparo et al. (2022), we account for PBH accretion both in the intergalactic medium (IGM) and in DM haloes, and we self-consistently derive the IGM temperature evolution, considering ionization and heating due to X-ray emission from PBHs. The Z22 model is based on the ΛCDM linear matter power spectrum, and considers a δ function for the PBH mass distribution.

Besides this ΛCDM-δ model, we have considered the possibility that PBHs modify the matter power spectrum (PBH-δ model), and follow an extended lognormal mass function (PBH-lognormal model). In both PBH-δ and PBH-lognormal models we adopt a PBH-ΛCDM cosmology, accounting for the matter power spectrum modified by PBHs.

For each model, we have derived the intensity and angular power spectrum of the NIRB finding that PBHs contribute to the observed NIRB fluctuations to < 1 per cent, even in the most optimistic cases considered in this work. This conclusion is supported by these intermediate results:

- The PBH modification to the power spectrum affects the variance of the matter overdensity field and thus the halo mass function, adding an extra power on small scales. In particular, at $z = 20$, in the PBH-ΛCDM model, the halo mass function is a factor of 3 (40) higher for $M_h = 10^5\ {\rm M}_\odot$ ($M_h = 10^7\ {\rm M}_\odot$) with respect to the standard ΛCDM case, considering $f_{\rm PBH} M_{\rm PBH} = 100$.

- As a consequence of the increased number of small haloes expected in the PBH-ΛCDM, the contribution to the total emissivity from accreting PBHs in DM haloes is enhanced by a factor of 2 (20) at redshift $z = 30$ (40). Moreover, also the collapsed DM fraction is higher and thus the relative contribution from PBHs accreting in the IGM is further lowered. The emissivity of PBHs accreting in haloes at redshift $z = 20\ (40)$ is roughly 10 (100) times the emissivity from PBHs in the IGM. We point out that, as a consequence of the aforementioned effects, in the PBH-ΛCDM cosmology the halo emissivity dominates the IGM one at any redshift, unlike in the standard ΛCDM case.

- If the radiative efficiency is indipendent of the accretion rate, given an extended mass function, the emissivity of PBHs accreting in the IGM can be computed adopting a delta mass function with mass equal to the mean mass of the mass function $\bar{M}_{\rm log}$. We compare the bolometric luminosity of haloes in the case of a delta mass function with $M_{\rm PBH} = 30\ {\rm M}_\odot$ and of a lognormal mass function with $\bar{M}_{\rm log} = 30\ M_\odot$. Including the lognormal mass function boosts the halo luminosity by a factor of ~ 10, because more massive PBHs accrete at smaller distances from the center, where the gas density is higher.

- Considering $1 \leq M_{\rm PBH}\ [{\rm M}_\odot] \leq 10^3$ and $f_{\rm PBH} = 1$, PBHs can produce at most ~ 1 per cent of the flux required to explain NIRB fluctuations. The three models differ in their prediction by less than a factor of $\simeq 2$. Although in PBH-ΛCDM cosmology the total emissivity of PBHs at $z \gtrsim 40$ is ~ 10 higher than in the standard ΛCDM scenario (for both delta and lognormal mass functions), the resulting NIRB is similar, because the gas heating from X-rays produced by PBHs damps their emissivity at lower redshifts.

- When accounting for current constraints on PBH abundance, the maximum relative contribution of PBHs to the NIRB is reduced to 0.1 per cent, for PBHs with $M_{\rm PBH} \sim 50\ {\rm M}_\odot$.

- None of our models is able to reproduce the NIRB angular power spectrum. At large angular scales ($\theta \sim 20$ arcmin), fluctuations predicted by model ΛCDM-δ (PBH-δ, PBH-lognormal) are lower than the measured one by a factor of $1000\ (400, 200)$, in the most favorable case with $M_{\rm PBH} = 10^3\ {\rm M}_\odot$.

Before concluding, we compare our findings with the results from Hasinger (2020, hereafter H20), whose model is adopted in Cappelluti et al. (2022). H20 predicted a NIR flux from PBHs of 10^{-13} erg s^{-1}cm^{-2}deg^{-2} $\sim 3\times10^{-4}$ nW m^{-2}sr^{-1}. This corresponds to ~ 0.3 per thousand of the NIRB flux required to explain NIRB fluctuations. Hence, we find a NIRB flux $\sim 10\times$ higher then the one obtained in H20. We point out some substantial differences between the two models to fully grasp the discrepancy in the two results. Firstly, H20 adopt a non-linear relative velocity between gas and DM to capture the collapse of baryons into DM haloes. This approach does not account for the density profile of DM and gas inside haloes, which enhance the contribution of PBHs accreting in haloes, as gas densities are much higher than the mean baryon density. Secondly, H20 estimates as negligible the heating of accreting gas by X-rays produced by PBHs, which instead in our model provides a negative feedback on the PBH emissivity. Moreover, H20 adopts an extended mass function with a peak around $1\ {\rm M}_\odot$, but with broad tails reaching up to $10^9\ {\rm M}_\odot$. They conclude that the dominant contribution arises from PBHs with $M_{\rm PBH} \sim 10^4\ {\rm M}_\odot$, while we focused only on the range $1 \leq M_{\rm PBH}/{\rm M}_\odot \leq 10^3$. A final difference concerns the accretion parameter, which they assume to be $\lambda = 0.05$, i.e. $5\times$ higher than the one adopted here.

To summarize, even if our modelling for the PBH contribution to the NIRB excess differs from the H20 one, we don't end up with a dramatic discrepancy. This is because the extra physical effects that we have included tend to balance each other. In fact, we should have expected a much higher NIRB flux due to the contribution of PBHs accreting in haloes and the boosted matter power spectrum due to the presence of the PBHs. However, these effects are balanced by the inclusion of the IGM heating from PBH X-ray emission that damps their emissivity at lower redshifts.

Part IV

Conclusions and future developments

Conclusions

This Thesis explored how radiation fields shaped the early Universe—by regulating star formation through feedback and by serving as observational probes of the first sources of light. The aim was to refine our understanding of cosmic evolution using the transformative view provided by JWST.

Starting from small scales, we explored how Lyα radiation pressure regulates star formation in the dense, metal-poor environments typical of primordial galaxies. We developed an analytical shell model that incorporates Lyα feedback using the latest formulations of the force multiplier, accounting for photon destruction by dust grains. The model was validated through dedicated one-dimensional hydrodynamical simulations. By considering feedback from a central stellar cluster, we derived upper limits to the star formation efficiency (SFE) achievable before Lyα feedback disrupts the parent cloud. Our results show that, regardless of gas surface density, Lyα feedback disrupts molecular clouds on timescales shorter than a free-fall time—well before the onset of supernova explosions for $\Sigma_g \gtrsim 10^3\,\mathrm{M_\odot\,pc^{-2}}$. At metallicities representative of high-redshift galaxies ($Z/Z_\odot \sim 10^{-2}$), the SFE is severely limited, ranging from $\epsilon_* \sim 0.01$ to ~ 0.6, and decreasing rapidly with lower metallicity. Order-unity efficiencies are attainable only under extreme conditions of surface density and near-solar metallicity.

We then extended our analysis to model early Lyαfeedback provided by Lyα-driven bubbles around massive stars. We developed a formalism to compute the evolution of the volume filling factor under the assumption that bubble growth is powered by Lyα feedback. By linking the filling factor to the star formation rate, we derived the final SFE of star-forming clouds. For typical cloud surface densities in the range $(37 - 1.7 \times 10^5)\,\mathrm{M_\odot\,pc^{-2}}$, we found $\epsilon_* < 0.08$, with higher values achievable only if Lyα-driven shells fragment and trigger secondary star formation. Even under optimistic assumptions, the SFE increases only modestly with surface density, from $\epsilon_* = 0.023$ at $\Sigma_g = 37\,\mathrm{M_\odot\,pc^{-2}}$ to $\epsilon_* = 0.27$ at $\Sigma_g = 1.7 \times 10^5\,\mathrm{M_\odot\,pc^{-2}}$. These values represent upper limits, reinforcing the conclusion that Lyα radiation pressure alone strongly suppresses the SFE, even at solar metallicity. Hence, a genuinely feedback-free phase of star formation leading to near-unity efficiency appears physically untenable in the early Universe.

The environment where Lyα feedback is expected to be most influential is that of Population III (Pop III) star formation. Simulations of Pop III evolution suggest that HII regions around massive primordial stars could remain gravitationally trapped within dense gas. However, accounting for Lyα feedback could drastically alter this picture. The additional radiation pressure may reduce accretion onto the protostar, thereby lowering the final stellar masses and possibly modifying the initial mass function (IMF). We argue that Lyα feedback is a key ingredient that should now be incorporated into theoretical models of Pop III star formation. The framework presented in this Thesis provides a foundation for more advanced studies, such as Lyα radiation–hydrodynamics (RHD) simulations in which Lyα transfer is solved in the diffusion approximation and coupled to hydrodynamics, including detailed microphysics.

On larger, cosmological scales, we tested whether primordial black holes (PBHs) could explain the observed excess in the large-scale fluctuations of the near-infrared background (NIRB). Modeling PBHs as a cold dark matter component, we computed the radiation emitted by gas accreting onto PBHs both in the intergalactic medium and within dark matter halos, self-consistently accounting for the heating and ionization of the gas by X-ray emission. We also considered PBH-induced modifications to the linear matter power spectrum and explored both monochromatic and lognormal mass functions in the range 1–$10^3\,\mathrm{M_\odot}$. Our results show that, even in the extreme case where PBHs constitute the entirety of the dark matter, their contribution to the observed NIRB fluctuations is below 1 per cent, and falls below 0.1 per cent when current constraints on PBH abundance are applied. We therefore conclude that PBHs cannot explain the NIRB excess and are ruled out as major contributors to this background.

In our calculations, the dominant contribution to the PBH-induced background originates from halos below the atomic-cooling threshold, where any treatment of star formation is not necessary. However, if PBHs are present, their X-ray, UV, and Lyman–Werner emission could profoundly influence star formation and the build-up of the first galaxies. A consistent model of PBH–galaxy co-evolution is therefore needed to search for indirect signatures of PBHs in early structure formation. This effort will require both semi-analytical models and high-resolution numerical simulations that fully capture the relevant feedback processes.

In summary, this Thesis provides new predictions for the star formation efficiencies of molecular clouds in the high-redshift Universe and establishes a benchmark framework for modeling Lyα radiation pressure feedback. It also delivers the first quantitative predictions for the NIRB fluctuations produced by PBHs, demonstrating that they cannot reproduce the observed levels. Several promising avenues now open to deepen our understanding of the high-redshift Universe.

Bibliography

Abbott B. P. e. a., 2019, Phys. Rev. X, 9, 031040

Abbott B. P., et al., 2016, Phys. Rev. Lett., 116, 061102

Abbott B. P., et al., 2017a, Phys. Rev. D, 96, 022001

Abbott B. P., et al., 2017b, Phys. Rev. Lett., 118, 221101

Abbott B. P., et al., 2019, The Astrophysical Journal Letters, 882, L24

Abbott R., et al., 2020a, Phys. Rev. Lett., 125, 101102

Abbott B. P., et al., 2020b, ApJL, 892, L3

Abbott R., et al., 2020c, ApJL, 896, L44

Abe M., Yajima H., 2018, MNRAS, 475, L130

Adamo A., et al., 2025, Nature Astronomy, 9, 1134

Adams T. F., 1972, ApJ, 174, 439

Adams T. F., 1975, ApJ, 201, 350

Adams N. J., et al., 2023, MNRAS, 518, 4755

Afshordi N., McDonald P., Spergel D. N., 2003, ApJL, 594, L71

Agazie G., et al., 2023, ApJL, 951, L8

Alcock C., et al., 1997, The Astrophysical Journal, 486, 697

Alcock C., et al., 2000, The Astrophysical Journal, 542, 281

Algera H., et al., 2025, REBELS-IFU: Dust Build-up in Massive Galaxies at Redshift 7 (arXiv:2501.10508), https://arxiv.org/abs/2501.10508

Ali-Haïmoud Y., 2018, Phys. Rev. Lett., 121, 081304

Ali-Haïmoud Y., Kamionkowski M., 2017, Phys. Rev. D, 95, 043534

Ali-Haïmoud Y., Kovetz E. D., Kamionkowski M., 2017, Phys. Rev. D, 96, 123523

Arthur S. J., Henney W. J., Dyson J. E., 1996, A&A, 313, 897

Bañados E., et al., 2018, Nature, 553, 473

Barkana R., Loeb A., 2001, Physics Reports, 349, 125–238

Bertoldi F., McKee C. F., 1992, ApJ, 395, 140

Binney J., Tremaine S., 2008, Galactic Dynamics: Second Edition. Princeton University Press

Bird S., Cholis I., Muñoz J. B., Ali-Haïmoud Y., Kamionkowski M., Kovetz E. D., Raccanelli A., Riess A. G., 2016, Phys. Rev. Lett., 116, 201301

Bisbas T. G., et al., 2015, Monthly Notices of the Royal Astronomical Society, 453, 1324

Bithell M., 1990, MNRAS, 244, 738

Blaineau T., et al., 2022, A&A, 664, A106

Blinnikov S., Dolgov A., Porayko N., Postnov K., 2016, JCAP, 2016, 036

Bombaci I., 1996, Astronomy and Astrophysics, 305, 871

Bondi H., 1952, Monthly Notices of the Royal Astronomical Society, 112, 195

Bonilha J. R. M., Ferch R., Salpeter E. E., Slater G., Noerdlinger P. D., 1979, ApJ, 233, 649

Brandt T. D., 2016, The Astrophysical Journal, 824, L31

Bromm V., Larson R. B., 2004, Annual Review of Astronomy and Astrophysics, 42, 79–118

Bryan G. L., Norman M. L., 1998, ApJ, 495, 80

Bunker A. J., et al., 2023, Astronomy & Astrophysics, 677, A88

Byrohl C., et al., 2021, Monthly Notices of the Royal Astronomical Society, 506, 5129–5152

Cantalupo S., Porciani C., Lilly S. J., 2008, The Astrophysical Journal, 672, 48

Cappelluti N., et al., 2013, ApJ, 769, 68

Cappelluti N., et al., 2017a, The Astrophysical Journal, 837, 19

Cappelluti N., et al., 2017b, ApJL, 847

Cappelluti N., Hasinger G., Natarajan P., 2022, ApJ, 926, 205

Carniani S., et al., 2024, Nature, 633, 318

Carr B. J., Hawking S. W., 1974, MNRAS, 168, 399

Carr B., Kühnel F., 2020, Annual Review of Nuclear and Particle Science, 70, 355

Carr B., Kühnel F., Sandstad M., 2016, Phys. Rev. D, 94, 083504

Carr B., Kohri K., Sendouda Y., Yokoyama J., 2021a, Constraints on Primordial Black Holes (arXiv:2002.12778)

Carr B., Clesse S., García-Bellido J., Kühnel F., 2021b, Physics of the Dark Universe, 31, 100755

Casey C. M., et al., 2023, The Astrophysical Journal, 954, 31

Castellano M., et al., 2023, ApJL, 948, L14

Castor J. I., 2004, Radiation Hydrodynamics. Cambridge University Press

Chapline G. F., 1975, Nature, 253, 251

Cheng Y.-T., Bock J. J., 2022, ApJ, 940, 115

Clesse S., García-Bellido J., 2017, Physics of the Dark Universe, 15, 142

Clesse S., García-Bellido J., 2022, Physics of the Dark Universe, 38, 101111

Coogan A., Morrison L., Profumo S., 2021, Phys. Rev. Lett., 126, 171101

Cooke R., 2024, arXiv e-prints, p. arXiv:2409.06015

Cooray A., Bock J. J., Keatin B., Lange A. E., Matsumoto T., 2004, ApJ, 606, 611

Cooray A., et al., 2012a, Nature, 490, 514

Cooray A., Gong Y., Smidt J., Santos M. G., 2012b, ApJ, 756, 92

Cox D. P., 1985, ApJ, 288, 465

Curti M., et al., 2024, A&A, 684, A75

Cyburt R. H., Fields B. D., Olive K. A., Yeh T.-H., 2016, Rev. Mod. Phys., 88, 015004

Dale J. E., Wünsch R., Whitworth A., Palouš J., 2009, MNRAS, 398, 1537

Dayal P., Ferrara A., 2018, Phys. Rep., 780, 1

Dayal P., maiolino R., 2025, The properties of primordially-seeded black holes and their hosts in the first billion years: implications for JWST (arXiv:2506.08116), https://arxiv.org/abs/2506.08116

Dayal, Pratika 2024, A&A, 690, A182

De Luca V., Franciolini G., Pani P., Riotto A., 2020, JCAP, 2020, 052

De Luca V., Desjacques V., Franciolini G., Pani P., Riotto A., 2021, Phys. Rev. Lett., 126, 051101

Decataldo D., Pallottini A., Ferrara A., Vallini L., Gallerani S., 2019, MNRAS, p. 1456

Dekel A., Sarkar K. C., Birnboim Y., Mandelker N., Li Z., 2023, MNRAS, 523, 3201

Deng Y., Li H., Liu B., Kannan R., Smith A., Bryan G. L., 2024, Astronomy & Astrophysics, 691, A231

Dijkstra M., 2014, Publications of the Astronomical Society of Australia, 31

Dijkstra M., Loeb A., 2008, MNRAS, 391, 457

Dijkstra M., Loeb A., 2009, MNRAS, 396, 377

Djorgovski S., Thompson D. J., 1992, in Barbuy B., Renzini A., eds, IAU Symposium Vol. 149, The Stellar Populations of Galaxies. p. 337

Dolgov A., Silk J., 1993, Phys. Rev. D, 47, 4244

Draine B. T., 2011, ApJ, 732, 100

Driver S. P., et al., 2016, ApJ, 827, 108

Edgar R., 2004, New Astron. Rev., 48, 843

Eisenstein D. J., et al., 2023, arXiv e-prints, p. arXiv:2306.02465

Fall S. M., Krumholz M. R., Matzner C. D., 2010, ApJL, 710, L142

Federrath C., 2015, Monthly Notices of the Royal Astronomical Society, 450, 4035

Fernandez E. R., Komatsu E., Iliev I. T., Shapiro P. R., 2010, ApJ, 710, 1089

Ferrara A., 2012, Nature, 490, 494

Ferrara A., 2024, A&A, 684, A207

Ferrara A., Pallottini A., Dayal P., 2023, MNRAS, 522, 3986

Franciolini G., Musco I., Pani P., Urbano A., 2022, Phys. Rev. D, 106, 123526

Franciolini G., Junior Iovino A., Vaskonen V., Veermae H., 2023, arXiv e-prints, p. arXiv:2306.17149

Furlanetto S. R., Stoever S. J., 2010, MNRAS, 404, 1869

Furtak L. J., et al., 2024, Nature, 628, 57

Gaikwad P., et al., 2020, MNRAS, 494, 5091

Gallerani S., Ferrara A., Fan X., Choudhury T. R., 2008, Monthly Notices of the Royal Astronomical Society, 386, 359

Gardner J. P., et al., 2023, Publications of the Astronomical Society of the Pacific, 135, 068001

Germani C., Musco I., 2019, Phys. Rev. Lett., 122, 141302

Girichidis P., et al., 2020, Space Science Reviews, 216

Grazian A., et al., 2024, What are the Pillars of Reionization? Revising the AGN Luminosity Function at z 5 (arXiv:2407.20861), https://arxiv.org/abs/2407.20861

Green A. M., Liddle A. R., Malik K. A., Sasaki M., 2004, Phys. Rev. D, 70, 041502

Greene J. E., et al., 2024, The Astrophysical Journal, 964, 39

Grisdale K., Agertz O., Renaud F., Romeo A. B., 2018, MNRAS, 479, 3167

Grudić M. Y., Hopkins P. F., Faucher-Giguère C.-A., Quataert E., Murray N., Kereš D., 2018, MNRAS, 475, 3511

HAWKING S. W., 1974, Nature, 248, 30

Haardt F., Madau P., 2012, The Astrophysical Journal, 746, 125

Hansen M., Oh S. P., 2006, Mon. Not. Roy. Astron. Soc., 367, 979

Harada T., Yoo C.-M., Kohri K., 2013, Phys. Rev. D, 88, 084051

Harikane Y., et al., 2023, ApJS, 265, 5

Harrington J. P., 1973, MNRAS, 162, 43

Hasinger G., 2020, Journal of Cosmology and Astroparticle Physics, 2020, 022–022

Helgason K., Ricotti M., Kashlinsky A., 2012, ApJ, 752, 113

Helgason K., Ricotti M., Kashlinsky A., Bromm V., 2016, MNRAS, 455, 282

Herenz E. C., et al., 2019, A&A, 621, A107

Heyer M., Krawczyk C., Duval J., Jackson J. M., 2009, ApJ, 699, 1092

Hill G. J., HETDEX Consortium 2016, in Skillen I., Balcells M., Trager S., eds, Astronomical Society of the Pacific Conference Series Vol. 507, Multi-Object Spectroscopy in the Next Decade: Big Questions, Large Surveys, and Wide Fields. p. 393

Hopkins P. F., Grudić M. Y., Wetzel A., Kereš D., Faucher-Giguère C.-A., Ma X., Murray N., Butcher N., 2020, MNRAS, 491, 3702

Hopkins P. F., et al., 2023, MNRAS, 519, 3154

Hu E. M., Cowie L. L., Barger A. J., Capak P., Kakazu Y., Trouille L., 2010, ApJ, 725, 394

Hubble E., 1929, Proceedings of the National Academy of Science, 15, 168

Jaskot A. E., 2025, ARA&A, 63, 45

Jiang D., Jiang L., Sun S., Liu W., Fu S., 2025, Nature Astronomy

Kannike K., Marzola L., Raidal M., Veermäe H., 2017, JCAP, 2017, 020

Kashikawa N., et al., 2011, ApJ, 734, 119

Kashlinsky A., 2016, The Astrophysical Journal, 823, L25

Kashlinsky A., Odenwald S., 2000, ApJ, 528, 74

Kashlinsky A., Mather J. C., Odenwald S., Hauser M. G., 1996, ApJ, 470, 681

Kashlinsky A., Arendt R. G., Mather J., Moseley S. H., 2005, Nature, 438, 45

Kashlinsky A., Arendt R. G., Mather J., Moseley S. H., 2007, ApJL, 654, L1

Kashlinsky A., Arendt R. G., Ashby M. L. N., Fazio G. G., Mather J., Moseley S. H., 2012, ApJ, 753

Kashlinsky A., Arendt R. G., Atrio-Barandela F., Cappelluti N., Ferrara A., Hasinger G., 2018, RMP, 90

Kashlinsky A., Arendt R. G., Ashby M. L. N., Kruk J., Odegard N., 2025, Looking at infrared background radiation anisotropies with Spitzer: large scale anisotropies and their implications (arXiv:2501.17751), https://arxiv.org/abs/2501.17751

Kavanagh B., 2019, doi:10.5281/zenodo.3538999

Kavanagh B. J., Gaggero D., Bertone G., 2018, Phys. Rev. D, 98, 023536

Kennicutt R. C., Evans N. J., 2012, Annual Review of Astronomy and Astrophysics, 50, 531–608

Kim J.-G., Kim W.-T., Ostriker E. C., 2016, ApJ, 819, 137

Kimm T., Haehnelt M., Blaizot J., Katz H., Michel-Dansac L., Garel T., Rosdahl J., Teyssier R., 2018, MNRAS, 475, 4617

Klessen R. S., Glover S. C. O., 2023, ARA&A, 61, 65

Kohandel M., 2022, PhD thesis, SNS

Kokorev V., et al., 2023, The Astrophysical Journal Letters, 957, L7

Kokorev V., et al., 2024, The Astrophysical Journal, 968, 38

Komarova L., Oey M. S., Krumholz M. R., Silich S., Kumari N., James B. L., 2021, ApJL, 920, L46

Kopp M., Hofmann S., Weller J., 2011, Phys. Rev. D, 83, 124025

Krumholz M. R., Matzner C. D., 2009, ApJ, 703, 1352

Krumholz M. R., Tan J. C., 2007, ApJ, 654, 304

Krumholz M. R., McKee C. F., Bland-Hawthorn J., 2019, ARA&A, 57, 227

Kühnel F., Freese K., 2017, Phys. Rev. D, 95, 083508

Lada C. J., Lombardi M., Alves J. F., 2010, ApJ, 724, 687

Laha R., 2019, Phys. Rev. Lett., 123, 251101

Lao B.-X., Smith A., 2020, MNRAS, 497, 3925

Latif M. A., Ferrara A., 2016, Publ. Astr. Soc. Australia, 33, e051

Lee E. J., Miville-Deschênes M.-A., Murray N. W., 2016, The Astrophysical Journal, 833, 229

Leinert C., et al., 1998, A&A Supp., 127, 1

Li Z., Dekel A., Sarkar K. C., Aung H., Giavalisco M., Mandelker N., Tacchella S., 2023, arXiv e-prints, p. arXiv:2311.14662

Lightman A. P., Schechter P. L., 1990, ApJS, 74, 831

Linde A. D., 1982, Physics Letters B, 108, 389

Liu B., Bromm V., 2022, ApJL, 937, L30

Liu B., Bromm V., 2023, arXiv e-prints, p. arXiv:2312.04085

Lu T.-Y., Mason C., Hutter A., Mesinger A., Qin Y., Stark D. P., Endsley R., 2023, The reionising bubble size distribution around galaxies (arXiv:2304.11192), https://arxiv.org/abs/2304.11192

Lu T.-Y., et al., 2025, Astronomy & Astrophysics, 697, A69

Macciò A. V., Dutton A. A., van den Bosch F. C., Moore B., Potter D., Stadel J., 2007, MNRAS, 378, 55

Madau P., Silk J., 2005, Monthly Notices of the Royal Astronomical Society, 359, L37

Madau P., Haardt F., Rees M. J., 1999, ApJ, 514, 648

Magg M., et al., 2020, Monthly Notices of the Royal Astronomical Society, 498, 3703

Maiolino R., et al., 2024a, Nature, 627, 59

Maiolino R., et al., 2024b, A&A, 687, A67

Makino N., Sasaki S., Suto Y., 1998, ApJ, 497, 555

Mason C. A., Treu T., Dijkstra M., Mesinger A., Trenti M., Pentericci L., de Barros S., Vanzella E., 2018, ApJ, 856, 2

Mason C. A., Trenti M., Treu T., 2023, MNRAS, 521, 497

Matsumoto T., et al., 2011, The Astrophysical Journal, 742, 124

Matsumoto T., Kim M. G., Pyo J., Tsumura K., 2015, ApJ, 807, 57

Matsuura S., et al., 2017, ApJ, 839, 7

Matteri A., Pallottini A., Ferrara A., 2025a, A&A, 697, A65

Matteri A., Ferrara A., Pallottini A., 2025b, Astronomy & Astrophysics, 701, A186

McGreer I. D., Mesinger A., D'Odorico V., 2015, MNRAS, 447, 499

McLeod D. J., et al., 2024, MNRAS, 527, 5004

Mena O., Palomares-Ruiz S., Villanueva-Domingo P., Witte S. J., 2019, Phys. Rev. D, 100, 043540

Menon S. H., Federrath C., Krumholz M. R., 2023, MNRAS, 521, 5160

Menon S. H., Burkhart B., Somerville R. S., Thompson T. A., Sternberg A., 2025, ApJ, 987, 12

Mesinger A., Ferrara A., Spiegel D. S., 2013, MNRAS, 431, 621

Meszaros P., 1975, A&A, 38, 5

Michel-Dansac L., Blaizot J., Garel T., Verhamme A., Kimm T., Trebitsch M., 2020, A&A, 635, A154

Mirocha J., Furlanetto S. R., 2023, MNRAS, 519, 843

Monroy-Rodríguez M. A., Allen C., 2014, ApJ, 790, 159

Mortlock D. J., et al., 2011, Nature, 474, 616

Munirov V. R., Kaurov A. A., 2023, MNRAS, 522, 2747

Murray N., 2011, ApJ, 729, 133

Murray N., Quataert E., Thompson T. A., 2010, ApJ, 709, 191

Murray S. G., Power C., Robotham A. S. G., 2013, Astronomy and Computing, 3, 23

Musco I., Miller J. C., Rezzolla L., 2005, Classical and Quantum Gravity, 22, 1405

Musco I., Miller J. C., Polnarev A. G., 2009, Classical and Quantum Gravity, 26, 235001

Naidu R. P., et al., 2022, ApJL, 940, L14

Naidu R. P., et al., 2025, A Cosmic Miracle: A Remarkably Luminous Galaxy at $z_{\rm spec} = 14.44$ Confirmed with JWST (arXiv:2505.11263), https://arxiv.org/abs/2505.11263

Navarro J. F., Frenk C. S., White S. D. M., 1996, ApJ, 462, 563

Nebrin O., 2025, Licentiate thesis, Department of Astronomy, Stockholm University

Nebrin O., Smith A., Lorinc K., Hörnquist J., Larson Å., Mellema G., Giri S. K., 2025, MNRAS, 537, 1646

Neufeld D. A., 1990, ApJ, 350, 216

Niemeyer J. C., Jedamzik K., 1999, Physical Review D, 59

Niikura H., Takada M., Yokoyama S., Sumi T., Masaki S., 2019, Phys. Rev. D, 99, 083503

Nikolić, Ivan Mesinger, Andrei Mason, Charlotte A. Lu, Ting-Yi Tang, Mengtao Prelogović, David Gagnon-Hartman, Samuel Stark, Daniel P. 2025, A&A, 699, A323

O'Brien B., Szczepańczyk M., Gayathri V., Bartos I., Vedovato G., Prodi G., Mitselmakher G., Klimenko S., 2021, Phys. Rev. D, 104, 082003

Oesch P. A., et al., 2014, ApJ, 786, 108

Oesch P. A., et al., 2016, The Astrophysical Journal, 819, 129

Oh S. P., Haiman Z., 2002, Astrophys. J., 569, 558

Olivier G. M., Lopez L. A., Rosen A. L., Nayak O., Reiter M., Krumholz M. R., Bolatto A. D., 2021, The Astrophysical Journal, 908, 68

Osterbrock D. E., 1962, ApJ, 135, 195

Osterbrock D. E., Ferland G. J., 2006, Astrophysics of gaseous nebulae and active galactic nuclei

Ouchi M., et al., 2009, ApJ, 696, 1164

Ouchi M., et al., 2018, Pub. Astron. Soc. Japan, 70, S13

Padmanabhan H., Loeb A., 2023, ApJL, 953, L4

Page D. N., Hawking S. W., 1976, Astrophysics Journal, 206, 1

Pallottini A., Ferrara A., Gallerani S., Vallini L., Maiolino R., Salvadori S., 2017, MNRAS, 465, 2540

Pallottini A., et al., 2022, MNRAS, 513, 5621

Partridge R. B., Peebles P. J. E., 1967, The Astrophysics Journal, 148, 377

Pathak D., et al., 2025, The Astrophysical Journal, 982, 140

Peacock J. A., 1998, Cosmological Physics. Cambridge University Press, doi:10.1017/CBO9780511804533

Pentericci L., et al., 2011, ApJ, 743, 132

Planck Collaboration et al., 2020, A&A, 641, A6

Poulin V., Serpico P. D., Calore F., Clesse S., Kohri K., 2017, Phys. Rev. D, 96, 083524

Press W. H., Schechter P., 1974, ApJ, 187, 425

Puchwein E., Haardt F., Haehnelt M. G., Madau P., 2019, MNRAS, 485, 47

Qin Y., Wyithe J. S. B., 2024, Reionization morphology and intrinsic velocity offsets allow transmission of Lyman-alpha emission from JADES-GS-z13-1-LA (arXiv:2409.07356), https://arxiv.org/abs/2409.07356

Raidal M., Vaskonen V., Veermäe H., 2017, JCAP, 2017, 037

Raiteri C. M., Villata M., Navarro J. F., 1996, A&A, 315, 105

Rees M. J., Ostriker J. P., 1977, MNRAS, 179, 541

Rémy-Ruyer A., et al., 2014, A&A, 563, A31

Rhoads J. E., Malhotra S., Dey A., Stern D., Spinrad H., Jannuzi B. T., 2000, ApJL, 545, L85

Ricotti M., Ostriker J. P., Mack K. J., 2008, ApJ, 680, 829

Roberts-Borsani G., et al., 2022, ApJL, 938, L13

Robertson B. E., 2022, Annual Review of Astronomy and Astrophysics, 60, 121–158

Robertson B. E., et al., 2023, Nat. Astronom., 7, 611

Robertson B., et al., 2024, ApJ, 970, 31

Rybicki G. B., dell'Antonio I. P., 1994, ApJ, 427, 603

Salvaterra R., Ferrara A., 2003, MNRAS, 339, 973

Salvaterra R., Ferrara A., 2006, MNRAS, 367, L11

Sano K., Kawara K., Matsuura S., Kataza H., Arai T., Matsuoka Y., 2015, ApJ, 811, 77

Santos M. R., Bromm V., Kamionkowski M., 2002, MNRAS, 336, 1082

Sasaki M., Suyama T., Tanaka T., Yokoyama S., 2016, Phys. Rev. Lett., 117, 061101

Schaerer D., 2002, A&A, 382, 28

Schaerer D., 2003, A&A, 397, 527

Schaerer D., Guibert J., Marques-Chaves R., Martins F., 2024, arXiv e-prints, p. arXiv:2407.12122

Schneider R., Ferrara A., Natarajan P., Omukai K., 2002, The Astrophysical Journal, 571, 30

Senchyna P., Plat A., Stark D. P., Rudie G. C., Berg D., Charlot S., James B. L., Mingozzi M., 2024, The Astrophysical Journal, 966, 92

Serpico P. D., Poulin V., Inman D., Kohri K., 2020, Physical Review Research, 2, 023204

Shibata M., Sasaki M., 1999, Phys. Rev. D, 60, 084002

Shibuya T., et al., 2018, Pub. Astron. Soc. Japan, 70, S14

Shibuya T., Ouchi M., Harikane Y., Nakajima K., 2019, ApJ, 871, 164

Smith A., Safranek-Shrader C., Bromm V., Milosavljević M., 2015, Monthly Notices of the Royal Astronomical Society, 449, 4336

Smith A., Bromm V., Loeb A., 2016, MNRAS, 460, 3143

Smith A., Bromm V., Loeb A., 2017, MNRAS, 464, 2963

Smith A., Tsang B. T. H., Bromm V., Milosavljević M., 2018, MNRAS, 479, 2065

Smith A., Ma X., Bromm V., Finkelstein S. L., Hopkins P. F., Faucher-Giguère C.-A., Kereš D., 2019, MNRAS, 484, 39

Smith A., Kannan R., Garaldi E., Vogelsberger M., Pakmor R., Springel V., Hernquist L., 2022, Mon. Not. Roy. Astron. Soc., 512, 3243

Smith A., Lorinc K., Nebrin O., Lao B.-X., 2025, MNRAS, 541, 179

Smoot G. F., et al., 1992, ApJL, 396, L1

Sobacchi E., Mesinger A., 2015, MNRAS, 453, 1843

Solomon P. M., Rivolo A. R., Barrett J., Yahil A., 1987, ApJ, 319, 730

Somerville R. S., Yung L. Y. A., Lancaster L., Menon S., Sommovigo L., Finkelstein S. L., 2025, arXiv e-prints, p. arXiv:2505.05442

Sommovigo L., Ferrara A., Pallottini A., Carniani S., Gallerani S., Decataldo D., 2020, MNRAS, 497, 956

Spitzer L., 1978, Physical processes in the interstellar medium, doi:10.1002/9783527617722.

Tacchella S., et al., 2023, The Astrophysical Journal, 952, 74

Tan J. C., McKee C. F., 2003, in Holt S. H., Reynolds C. S., eds, American Institute of Physics Conference Series Vol. 666, The Emergence of Cosmic Structure. pp 93–96 (arXiv:astro-ph/0212283), doi:10.1063/1.1581776

Taniguchi Y., et al., 2005, Pub. Astron. Soc. Japan, 57, 165

Tinker J. L., Robertson B. E., Kravtsov A. V., Klypin A., Warren M. S., Yepes G., Gottlöber S., 2010, ApJ, 724, 878

Tisserand, P. et al., 2007, A&A, 469, 387

Tomaselli G. M., Ferrara A., 2021, MNRAS, 504, 89

Topping M. W., Stark D. P., Endsley R., Plat A., Whitler L., Chen Z., Charlot S., 2022, ApJ, 941, 153

Topping M. W., et al., 2023, arXiv e-prints, p. arXiv:2307.08835

Topping M. W., et al., 2024, Monthly Notices of the Royal Astronomical Society, 529, 3301

Topping M. W., et al., 2025, The Astrophysical Journal, 980, 225

Trinca A., Schneider R., Valiante R., Graziani L., Ferrotti A., Omukai K., Chon S., 2024, MNRAS, 529, 3563

Tsumura K., Matsumoto T., Matsuura S., Sakon I., Wada T., 2013, Pub. Astron. Soc. Japan, 65

Umeda H., Ouchi M., Nakajima K., Harikane Y., Ono Y., Xu Y., Isobe Y., Zhang Y., 2024, JWST Measurements of Neutral Hydrogen Fractions and Ionized Bubble Sizes at $z = 7 - 12$ Obtained with Lyα Damping Wing Absorptions in 27 Bright Continuum Galaxies (arXiv:2306.00487), https://arxiv.org/abs/2306.00487

Valdés M., Evoli C., Ferrara A., 2010, MNRAS, 404, 1569

Vaskonen V., Veermäe H., 2021, Phys. Rev. Lett., 126, 051303

Verhamme A., Schaerer D., Maselli A., 2006, A&A, 460, 397

Villanueva-Domingo P., Ichiki K., 2023, Pub. Astron. Soc. Japan, 75, S33

Walch S., Whitworth A. P., Bisbas T. G., Wünsch R., Hubber D. A., 2013, MNRAS, 435, 917

Walther M., Oñorbe J., Hennawi J. F., Lukić Z., 2019, ApJ, 872, 13

Weingartner J. C., Draine B. T., 2001, ApJ, 548, 296

Witstok J., et al., 2025, Nature, 639, 897

Wong K. W. K., Franciolini G., De Luca V., Baibhav V., Berti E., Pani P., Riotto A., 2021, Phys. Rev. D, 103, 023026

Yuan F., Narayan R., 2014, ARA&A, 52, 529

Yue B., Ferrara A., Salvaterra R., Chen X., 2013a, Monthly Notices of the Royal Astronomical Society, 431, 383

Yue B., Ferrara A., Salvaterra R., Xu Y., Chen X., 2013b, MNRAS, 433, 1556

Zel'dovich Y. B., Novikov I. D., 1967, Soviet Ast., 10, 602

Zhang S., Liu B., Bromm V., Jeon J., Boylan-Kolchin M., Kuhnel F., 2025, How do Massive Primordial Black Holes Impact the Formation of the First Stars and Galaxies? (arXiv:2503.17585), https://arxiv.org/abs/2503.17585

Ziparo F., Gallerani S., Ferrara A., Vito F., 2022, MNRAS, 517, 1086

Ziparo F., Ferrara A., Sommovigo L., Kohandel M., 2023, MNRAS, 520, 2445

Ziparo F., Gallerani S., Ferrara A., 2024, Primordial black holes as supermassive black holes seeds (arXiv:2411.03448), https://arxiv.org/abs/2411.03448

de Bernardis P., et al., 2000, Nature, 404, 955

et al B. P. A., 2019, The Astrophysical Journal, 882, L24